Summer 8-6-2024

Constraints on Solar Axions Using the Profile Likelihood Ratio Method with the SuperCDMS Experiments

Shilun Liu
Southern Methodist University, shilunl@smu.edu

Recommended Citation

Liu, Shilun, "Constraints on Solar Axions Using the Profile Likelihood Ratio Method with the SuperCDMS Experiments" (2024). *Physics Theses and Dissertations*. 19.
https://scholar.smu.edu/hum_sci_physics_etds/19

CONSTRAINTS ON SOLAR AXIONS USING THE PROFILE LIKELIHOOD RATIO METHOD WITH THE SUPERCDMS EXPERIMENTS

Approved by:

Dr. Jodi Cooley
Professor

Dr. Joel Meyers
Assistant Professor

Dr. Fredrick Olness
Professor

Dr. Robert Calkins
Research Assistant Professor

Dr. Matthew Klein
Assistant Professor

Dr. Belina von Krosigk
Professor

CONSTRAINTS ON SOLAR AXIONS
USING THE PROFILE LIKELIHOOD RATIO METHOD
WITH THE SUPERCDMS EXPERIMENTS

A Dissertation Presented to the Graduate Faculty of the

Dedman College

Southern Methodist University

in

Partial Fulfillment of the Requirements

for the degree of

Doctor of Philosophy

with a

Major in Physics

by

Shilun Liu

B.S., Physics, Applied Mathematics, Southern Methodist University
M.S., Physics, Southern Methodist University

August 6, 2024

Acknowledgments

My graduate school journey was filled with many unexpected challenges and difficulties. Although I continued studying at the same university from my undergraduate, it was a completely different experience. Being apart from my family was the most difficult part, especially since I used to see them every summer and winter break. There was a time when I hadn't been home for almost three years and this separation made me realize how important the support and encouragement from my family was to me.

I am deeply grateful to my parents, especially my mom, for their unwavering emotional and financial support. Their decision to send me abroad for my undergraduate studies and their continued support for my PhD have been instrumental in my academic journey. Their belief in my abilities and their sacrifices have been a constant source of motivation and strength. I also extend my heartfelt thanks to my aunt, my grandma, and my grandma's sister and her family for their warm hospitality and care whenever I returned home. Additionally, I am thankful to my cousin and her family for taking care of me in Dallas, providing a home away from home.

My PhD journey wouldn't have been possible without my advisors—Dr. Jodi Cooley and Dr. Joel Meyers. I am very grateful for Dr. Meyers' brilliant guidance and exceptional mentorship. I am also very grateful to Dr. Cooley for recruiting me to the SuperCDMS collaboration and continuing to provide research grants after she transferred away. Special thanks to Dr. Rob Calkins for his technical insights, which have significantly contributed to my research. I would also like to thank Dr. Robert Kehoe for involving me in his VSX project during my undergraduate years, where I first began my journey into physics research. Additionally, I really appreciate the great lectures and the supportive, caring presence of

SMU professors, especially Dr. David Son and his spouse Heidi, Dr. Randall Scalise, and Dr. Fred Olness. Lastly, I appreciate the hard work and dedication of all the SuperCDMS collaborators, whose efforts have been essential to my thesis.

I am also extremely glad to have all the amazing people who kept me going. Thanks to Tairi, my mom's mentor and now mine, for guiding us with kindness and wisdom. Thanks to Dr. Eric Guzman for being the most supportive peer with his constant encouragement. Thanks to Ju Zhao for all our weekend grinding sessions and feasting on good food together afterward. Thanks to my friends back home for the good times, especially Jing Cai and Yi Xie. And to all the incredible people I met last summer at Voloridge, thanks for the great experiences and friendships. To everyone else who played a part in this journey—there are too many to name, but all my friends' support means the world to me. They made this journey not only less difficult but also much more memorable.

Last but not least, I need to give a huge shoutout to my furry children—Tako (canine) and Karaage (feline). They are seriously the cutest things in the world and have been my ultimate emotional support throughout this wild PhD ride. Also, shoutouts to Teresa and her family, Nicole, and Ran for always taking care of Tako when I needed a hand. I'm excited to start the new chapter of my life, filled with gratitude and anticipation for what's to come.

Liu, Shilun B.S., Physics, Applied Mathematics, Southern Methodist University
M.S., Physics, Southern Methodist University

Constraints on Solar Axions Using the Profile Likelihood Ratio Method with the SuperCDMS Experiments

Advisors: Dr. Jodi Cooley and Dr. Joel Meyers
Doctor of Philosophy degree conferred August 6, 2024
Dissertation completed August 1, 2024

Dark matter plays an essential role in understanding modern physics and particles beyond the Standard Model. Evidence suggests that dark matter accounts for approximately 85% of the universe's matter, and 26.8% of its mass-energy composition. Key candidates for dark matter include unidentified subatomic particles like Weakly Interacting Massive Particles (WIMPs) and axions. The Super Cryogenic Dark Matter Search (SuperCDMS) employs direct detection methods to identify these elusive particles using cryogenic technologies. SuperCDMS Soudan is the latest completed CDMS experiment in Minnesota, in preparation for the next phase experiments of SuperCDMS SNOLAB in Sudbury, Canada. At SNOLAB, the Cryogenic Underground TEst (CUTE) facility is dedicated to analyze background levels prior to the full operation of SuperCDMS SNOLAB experiments. Utilizing collected data from CDMSlite Run 3 at Soudan Underground Laboratory with minimized background interference, sensitivity limits were established for solar axions within the keV energy range using the profile likelihood ratio method. Our results show an axio-electric coupling constant constraints $g_{ae} < 5.91\times10^{-11}$ from the atomic recombination and de-excitation, Bremsstrahlung, and Compton channels at a 90% confidence level.

TABLE OF CONTENTS

CHAPTER

LIST OF FIGURES

LIST OF TABLES

This thesis is dedicated to my determined self, who worked hard and never gave up.

Chapter 1

Introduction of Dark Matter and Axions

In modern physics, abundant observations have suggested that the majority of the matter density in the universe consists of non-luminous "dark matter". The idea that dark matter may consist of subatomic particles that are beyond the Standard Model of particle physics has brought it to the forefront of scientific research. This chapter aims to explore the theoretical and empirical foundations that highlight the particle dark matter hypothesis, emphasizing the evidence that prompts ongoing searches.

The current observational evidence of dark matter, which will be discussed in detail in Section 1.1, indicates that dark matter does not interact electromagnetically and its existence is only implied by gravitational effects. The observational evidence suggests that dark matter could be a new subatomic particle that is beyond the Standard Model of particle physics, which has propelled dark matter to the forefront of modern physics as one of the most appealing enigmas for physicists to solve.

Observational evidence that will be discussed in this chapter include galactic cluster dynamics (Section 1.1.1), galactic rotation curves (Section 1.1.2), gravitational lensing (Section 1.1.3), cosmic microwave background anisotropy (Section 1.1.4), and Big Bang nucleosynthesis (Section 1.1.5). All these observations suggest that dark matter is approximately 85% of the total mass in the universe, making it roughly five times as much as regular matter defined in the standard ΛCDM model of cosmology. In the ΛCDM model, the universe consists of 5% ordinary matter, 26.8% dark matter and 68.2% dark energy [1].

Despite the compelling evidence for dark matter, alternative theories have been proposed to explain the observed gravitational effects without invoking dark matter (Section 1.2). However, the particle dark matter hypothesis remains the most widely accepted explanation. Various dark matter candidates have been proposed, including astrophysical objects (Section 1.3.1), Weakly Interacting Massive Particles (WIMPs) (Section 1.3.2), QCD axions (Section 1.3.3), and axion-like particles (ALPSs) (Section 1.3.4).

Among these candidates, axions and ALPs have gained significant attention due to their potential to solve the strong CP problem in quantum chromodynamics (QCD) and their ability to explain the observed dark matter density. Constraints on the axion-electron coupling constant g_{ae} from the astrophysical measurements (Section 1.4.1) and theoretical considerations (Section 1.4) will be discussed in detail. In particular, solar axions (Section 1.5) have been a focus of experimental searches in this thesis, as they are expected to be produced in the Sun through various mechanisms. The solar axion flux (Section 1.5.1), and the axio-electric effect (Section 1.5.2) are of particular interest in these searches.

1.1. Observational Evidence

Dark matter, a mysterious and unseen substance, has left its mark on a variety of astronomical observations. The unusual movements of galaxies within clusters, the unexpected rotation speeds of individual galaxies, the bending of light by invisible mass, the variations in the cosmic microwave background, and the primordial element abundances all provide compelling evidence for dark matter's existence. This section delves into the observational evidence supporting the dark matter theory, illustrating how each piece of evidence enhances our understanding of the universe.

1.1.1. Galactic cluster dynamics

The very early physical evidence for dark matter traced back to 1933, when Fritz Zwicky measured the visible mass of a cluster of galaxies at the Mount Wilson Observatory. By observing the redshifts of galaxies within the Coma Cluster, Zwicky was able to estimate the apparent velocities of the galaxies. Then he applied the virial theorem to the Coma Cluster, relating the average kinetic energy of the system to its total potential energy, and calculated the mass of the entire cluster. In the virial theorem, if a dynamic ensemble consists of N interacting particles, where the interactions are governed by conservative forces, the mean kinetic energy of the system, denoted by $\langle T\rangle$, can be expressed as follows:

$$\langle T\rangle = \frac{1}{2}\sum_{k=1}^{N}\langle \mathbf{F}_k \cdot \mathbf{r}_k\rangle \tag{1.1}$$

where the k^{th} particle situated at position $\mathbf{r}_k$ within the ensemble, experiencing a net force represented by $\mathbf{F}_k$. In the case where the interparticle forces are derivable from a potential energy function V that exhibits a dependence on the interparticle separation r, the virial theorem can be formulated as:

$$2\langle T\rangle = -\langle V\rangle \tag{1.2}$$

which suggests that for a gravitationally bound system, the time-averaged kinetic energy is proportional to the potential energy, thereby indicating the system's total mass.

Different from expectations, the mass inferred from the luminosity of the galaxies fell significantly short of what was needed to explain the observed velocities to prevent the galaxies from escaping the gravitational pull of the cluster [2]. This discrepancy suggested that a considerable portion of the cluster's mass was invisible or "dark."

Zwicky described the phenomenon as something gluing the clusters of galaxies together [2]. In his works, he also highlighted the potential of using gravitational lensing to estimate the mass of galaxy clusters. This suggested approach was later employed by many lensing surveys, which demonstrate the distribution of dark matter across various scales. These findings are in strong alignment with simulations modeling the large-scale structure of the universe [3].

1.1.2. Galactic rotation curves

Galactic rotation curves are graphical representations that illustrate the orbital speed of various galactic components, such as stars and interstellar gas, as a function of their radial distance from the galactic center. The motion of these galactic components can be described using the virial theorem in Eq. 1.1, which relates the time-averaged kinetic and potential energies of objects within a gravitationally bound system. For a star or an object of mass m orbiting a central mass M, the time-averaged potential energy $\langle V \rangle$ can be expressed as:

$$\langle V \rangle = -\frac{GmM(r)}{r} \tag{1.3}$$

where $M(r)$ is the total mass enclosed within the radius r, and G is the gravitational constant, assuming a spherically symmetric mass distribution. For an object with mass m following a circular orbit with velocity v, the time-averaged kinetic energy $\langle T \rangle$ can be written as:

$$\langle T \rangle = \frac{1}{2}mv^2 \tag{1.4}$$

Then the rotational velocity v of an object orbiting at a distance r from the center of the galaxy can be expressed by the following equation:

$$v = \sqrt{\frac{GM(r)}{r}} \tag{1.5}$$

Observations have revealed that the density of luminous matter decreases significantly at larger galactic radii. Consequently, based on the distribution of visible matter alone, one would expect the velocity profile to exhibit a decline proportional to $r^{-1/2}$ at greater distances from the galactic center.

After Zwicky's discovery, Vera Rubin and Kent Ford conducted significant research on measuring rotation curves of individual galaxies in the 1970s. Their work involved calculating the velocity profile of ionized hydrogen in the Andromeda Galaxy using Doppler-shifted H_α emission lines, revealed a constant velocity at large radii instead of the expected $r^{-1/2}$ trend [4]. They observed that the rotational velocity of galaxies remain constant beyond their centers, implying the galaxy's total mass continues to increase even outside its brightly luminous core. This observation led to the hypothesis of an extensive, invisible dark halo surrounding each galaxy, stretching beyond its visible limits. Over the course of the decade, they compiled rotation curves for numerous galaxies of different sizes, shown in Figure 1.1, where they consistently observed the same flat behavior at high radii [5, 6].

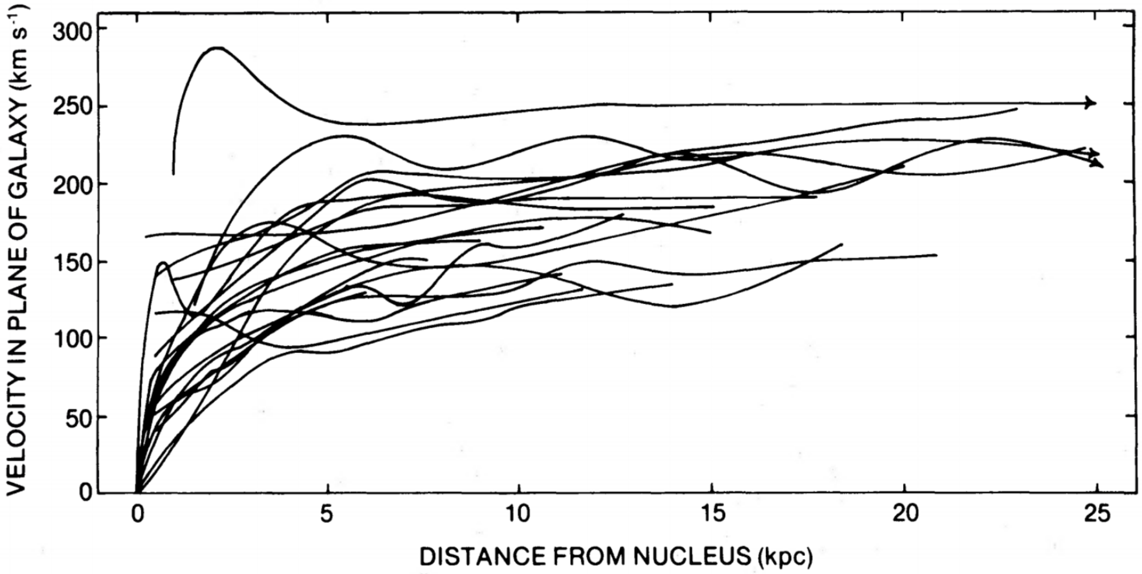

Figure 1.1: Collection of rotation curves for several galaxies. The velocity of objects far from the galactic core is relatively constant at high raddi. Image taken from [6].

One supporting example that further depicted this result is the improved rotation curve of the galaxy NGC 6503 shown in Figure 1.2, which was obtained subsequent to Rubin's work in the 1990s. This result confirmed Rubin's initial observations and provides evidence for the presence of dark matter halos surrounding galaxies.

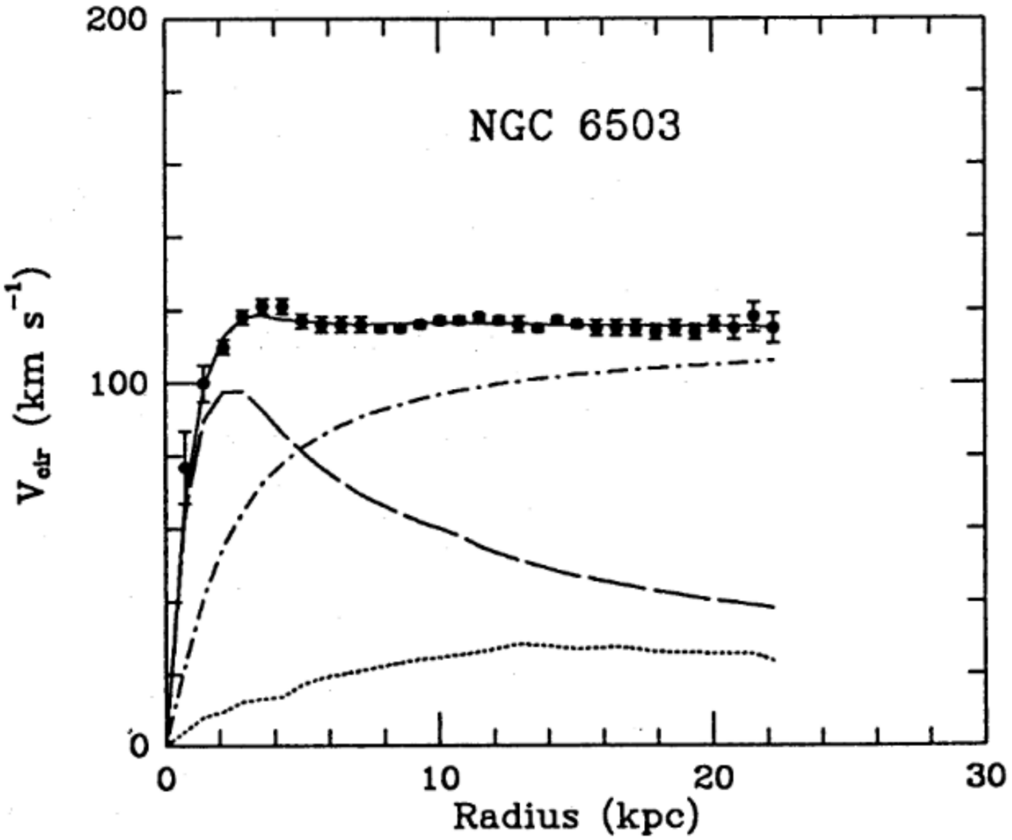

Figure 1.2: The measured rotation curve of the galaxy NGC 6503 is shown with points and uncertainty bars. The best-fit value for the dark halo is represented by the solid black line. Additionally, the rotation curves of individual components are depicted: the visible components by the dashed curve, the gas by the dotted curve, and the dark halo by the dotted-dashed curve. The inclusion of the dark halo component is necessary to explain the flatness of the rotation curve at large distances from the galaxy's center. Image taken from [7].

These rotation curves eventually revealed that some unseen matter was preventing galaxies from drifting apart. This important discovery provided compelling evidence for the existence of dark matter, fundamentally altering the scientific community's understanding of the universe's composition. It challenged existing models and prompted the development of new theories to account for this mysterious, non-luminous matter.

1.1.3. Gravitational lensing

Observational evidence of dark matter is particularly striking in the dynamics of galaxy cluster mergers. Galaxy clusters, rich in hot gas and visible matter like stars, reveal their dark matter content during these mergers. Techniques like X-ray imaging and gravitational lensing are employed to track baryonic matter and the gravitational potential of clusters, respectively. They show that during a merger, the dark matter, interacting mainly through gravity, behaves differently from baryonic matter, which is slowed down by electromagnetic interactions [8].

Gravitational lensing, a phenomenon predicted by Einstein's general theory of relativity, has emerged as a powerful tool for detecting and studying dark matter in the Universe. This effect occurs when the presence of a massive object, such as a galaxy or galaxy cluster, distorts the fabric of spacetime, causing light from distant background sources to bend and follow curved paths [9]. The gravitational lensing effect caused by a point mass M results in an angular deflection α of the light ray, which can be expressed as [9]:

$$\alpha = \frac{4GM}{rc^2} \tag{1.6}$$

where r represents the distance between the light source and the lens in the plane perpendicular to the observer's line of sight, G denotes the gravitational constant, and c is the speed of light.

In extreme cases of strong gravitational lensing, the distortion of the background source can manifest as arc-like structures or even complete ring images, known as Einstein rings, which occur when the observer, lens, and light source are precisely aligned [8]. By carefully modeling these gravitational lensing distortions, astronomers can estimate the total mass and the mass distribution of the lensing object, such as a galaxy cluster or an individual galaxy [10]. This technique provides a direct means of measuring the total mass of the lens, independent of the methods based on the dynamics of rotation curves.

A compelling example of how dark matter appears to behave differently than baryonic matter is provided by the study of the Bullet Cluster. The observation of the Bullet Cluster, shown in Figure 1.3, demonstrates that the gravitational potential is spatially separated from visible matter. The Bullet Cluster, despite its name, is actually a system of two colliding galaxy clusters. These clusters contain three main components: galaxies, intergalactic plasma that emits X-rays, and potentially dark matter. The plasma accounts for most of the visible mass. During the collision, the stellar and plasma components of each cluster exhibit distinct behaviors. The galaxies act as collisionless particles, while the colliding plasma experiences a significant slowdown due to electromagnetic interactions. This difference in behavior results in a spatial separation of the plasma and stellar components, which can be observed through optical and X-ray measurements. This separation could be an indicator that dark matter is not visible through electromagnetic interactions. This separation not only suggests that dark matter does not interact with electromagnetic radiation, but it also implies that the self-interaction of dark matter is relatively weak.

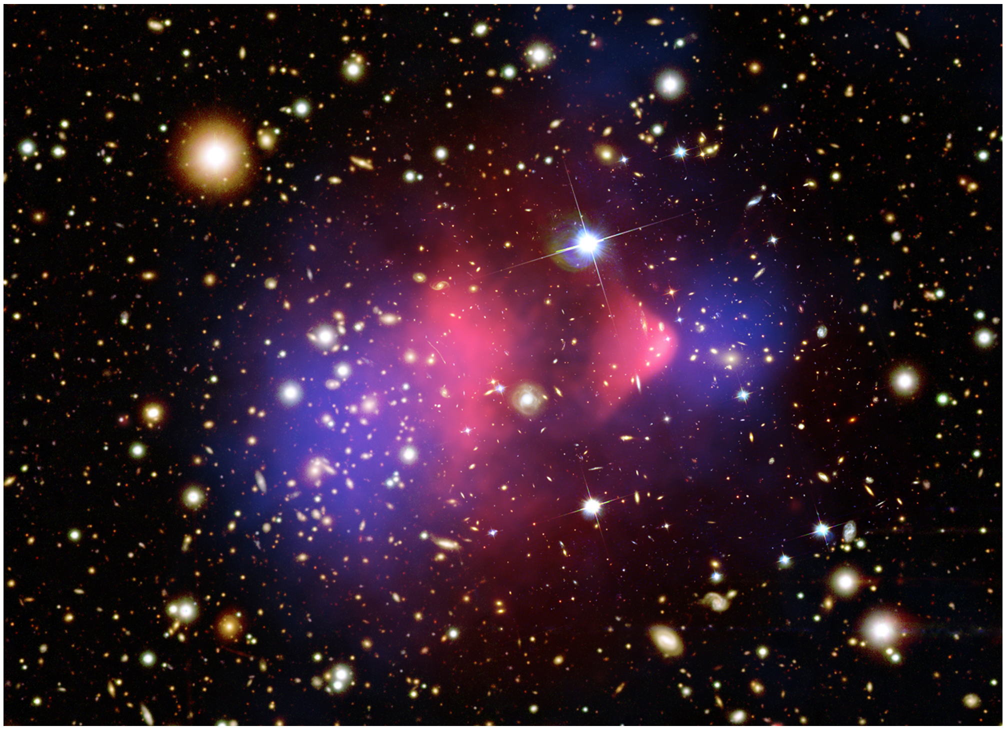

Figure 1.3: A composite image of the Bullet Cluster (1E 0657-558), a system of two colliding galaxy clusters, shows the distribution of galaxies in the clusters through optical observation (background image). The observed shock wave in the gas distribution, resembling a bullet shape, gives the cluster its name. Image taken from NASA [11].

The Hubble Space Telescope captured images of the stellar component [11], while the Chandra X-Ray Observatory mapped the distribution of the plasma [8]. The mass distribution of the Bullet Cluster has been independently measured through gravitational lensing techniques by Clowe et al. (2006) [8]. In the absence of non-standard model matter, one would expect the mass distribution to closely follow the distribution of the interstellar plasma. However, as depicted in Figure 1.4, the true centers of mass do not coincide with the centers of mass of ordinary matter. Instead, there are two large distributions of non-luminous matter that have passed through one another during the collision.

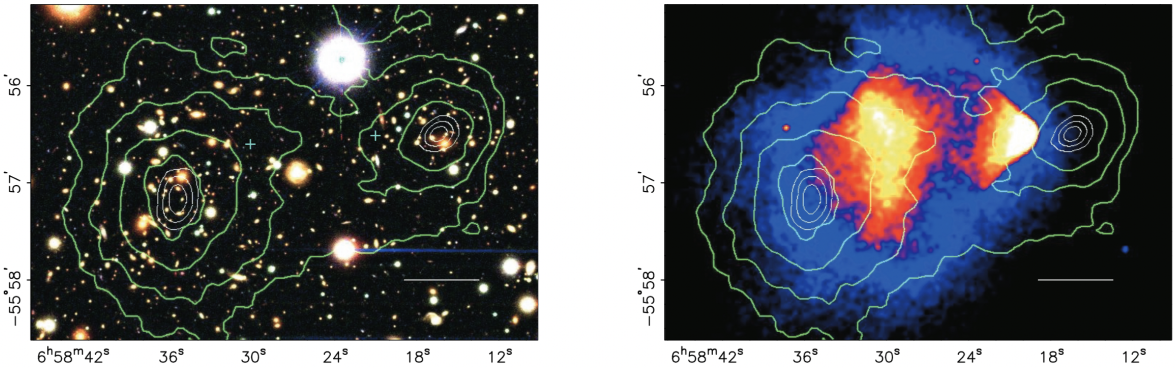

Figure 1.4: Images of the Bullet Cluster showing the stellar (left) and X-ray emitting plasma (right) components. The green contours represent the mass distribution derived from gravitational lensing observations. Notably, the centers of mass indicated by these contours do not coincide with the distributions of the X-ray emitting plasma, which constitutes the dominant component of ordinary matter in the cluster. Image taken from [8].

By comparing the gravitational lensing map with the optical and X-ray observations, researchers have found that the majority of the mass in the Bullet Cluster is not associated with the X-ray emitting plasma, but instead follows the distribution of galaxies [8]. The observed total mass distribution suggests that the majority of the mass in the cluster is composed of an unseen, largely collisionless form of matter, providing convincing evidence for the existence of dark matter.

Furthermore, observations of the Bullet Cluster have allowed researchers to place tighter constraints on the self-interaction cross-section of dark matter per unit mass (σ/m). By running full N-body simulations of the merging galaxy clusters that include the effects of self-interacting dark matter and comparing the results with higher-quality observational datasets, Randall et al. (2008) [12] derived an upper limit (68% confidence) of $\sigma/m < 1.25\,\mathrm{cm}^2/\mathrm{g}$. This constraint is based on the non-observation of an offset between the bullet subcluster mass peak and galaxy centroid. Additionally, assuming equal mass-to-light ratios for the subcluster and main cluster prior to the merger, they obtained an even more stringent constraint of $\sigma/m < 0.7\,\mathrm{cm}^2/\mathrm{g}$, which ruled out the possibility of a large fraction of dark matter particles being scattered away due to collisions. [12]

1.1.4. Cosmic microwave background

Another important piece of supporting evidence of dark matter is the observations of the cosmic microwave background (CMB), which not only supports the dark matter hypothesis but also constraints the properties of dark matter [13].

According to Big Bang cosmological models, during the earliest periods, the universe was filled with hot plasma of subatomic particles. As the universe continued to expand and cool, the plasma reached a temperature at which protons and electrons could combine to form neutral hydrogen atoms, a process known as recombination [14]. Unlike the plasma, these neutral atoms did not interact with thermal radiation through Thomson scattering, resulting in a transparent universe. This decoupling event, referred as the recombination epoch, allowed photons to travel freely through space, creating what is known as relic radiation. These photons are now observable as the Cosmic Microwave Background (CMB), representing the universe's earliest detectable light. The CMB photons observed today originated from the "surface of last scattering". This is a conceptual sphere in space that represents the furthest distance light could travel to reach the earth since the decoupling event. Due to the expansion of the universe, these photons have experienced cosmological redshift $z \simeq 1100$ at the last scattering surface, losing energy over time. Nonetheless, they provide us with a glimpse of the universe's earliest observable light, offering crucial evidence for the Big Bang theory and the evolution of the cosmos.

The expansion of the universe and its contents can be described using the Friedmann equation, which relates the density parameters of various components to the curvature and expansion rate of the universe:

$$\sum_i \Omega_i + \Omega_\Lambda - 1 = \frac{k}{R^2 H^2} \tag{1.7}$$

where $\sum_i \Omega_i$ sums over all the different species of material in the universe, and the right-hand side represents the spatial curvature. Equation 1.7 holds true at any epoch, but the symbols Ω_i and Ω_Λ are often used to refer specifically to the present-epoch values. The density parameter Ω_i is defined as:

$$\Omega_i = \frac{\rho_{i,0}}{\rho_{\text{crit},0}} \tag{1.8}$$

where $\rho_{i,0}$ is the density of the i-th component (matter, radiation, or dark energy) at the present time (denoted by the subscript 0), and $\rho_{\text{crit},0}$ is the critical density of the universe at the present time, given by:

$$\rho_{\text{crit},0} = \frac{3H_0^2}{8\pi G} \tag{1.9}$$

where H_0 is the Hubble constant (the expansion rate of the universe at the present time), and G is the gravitational constant. [15]

The complete present-epoch state of the homogeneous universe can be described by specifying the current-epoch values of all the density parameters and the Hubble parameter H (the present-day Hubble parameter $H_0 = 100h$ km s^{-1} Mpc^{-1}). A typical collection of density parameters would include baryons (Ω_b), photons (Ω_γ), neutrinos (Ω_ν), and cold dark matter (Ω_c), known as the ΛCDM model. The electron density is not considered separately due to charge neutrality and is effectively included with the baryons. The spatial curvature can be determined from the other parameters using the Friedmann equation. The total present matter density Ω_m, which is the sum of Ω_c and Ω_b, may be used in place of the cold dark matter density Ω_c. [16]

The overall shape of the CMB spectrum is well-described by a blackbody curve with a temperature of 2.72548 ± 0.00057 K [17]. The spectral shape in Figure 1.5 is a major prediction of the hot Big Bang model and it is consistent with the presence of dark matter in the early universe. Models without dark matter would predict a different spectral shape that is not observed [1]. However, the CMB is not perfectly uniform but exhibits small temperature fluctuations or anisotropies on the order of $\Delta T/T \approx 10^{-5}$ [18]. CMB anisotropies are typically represented using a spherical harmonic decomposition of the CMB sky map:

$$T(\theta, \phi) = \sum_{lm} a_{lm} Y_{lm}(\theta, \phi) \tag{1.10}$$

where l and m indices denote the spherical harmonics' degree and order, respectively.

The CMB anisotropies, represented by the spherical harmonic decomposition in Equation 1.7, play a crucial role in constraining the properties of dark matter and other cosmological parameters. The angular power spectrum of the CMB anisotropies, which quantifies the amplitude of the fluctuations as a function of angular scale, exhibits several acoustic peaks whose relative heights and locations are sensitive to the densities of baryonic matter, dark matter, and dark energy in the early universe [19]. By comparing the observed power spectrum with theoretical predictions from the ΛCDM model, cosmologists have obtained precise measurements of the baryon density, dark matter density, and other parameters that characterize the composition and evolution of the universe [1]. These measurements have conclusively established the presence of non-baryonic dark matter as a dominant component of the cosmos, complementing the evidence from other cosmological probes such as galaxy surveys and gravitational lensing studies.

The CMB power spectrum, observed by the Planck satellite, is shown in Figure 1.5. The key features of the power spectrum include the peaks and troughs, the spacing between the peaks, and the position of the first peak, which were influenced by the initial conditions and energy content of the Universe at the time of recombination and its subsequent evolution [1]. The location of the first peak is consistent with a flat Universe, implying that the current energy density of the Universe is equal to the critical density ρ_{crit} [15]. The band power peaks correspond to oscillatory modes in the baryon-photon fluid, which were at their maximum or minimum of oscillation when decoupling occurred. The position and spacing of the peaks can be used to estimate the density parameters for dark energy Ω_Λ and matter Ω_M, as well as the spatial curvature of the Universe Ω_k. Notably, the presence of baryons at the time of decoupling suppresses the heights of even-numbered peaks compared to odd-numbered peaks. As a result, the difference in height between the second peak and the first and third peaks provides a measure of the baryon density parameter Ω_b [19].

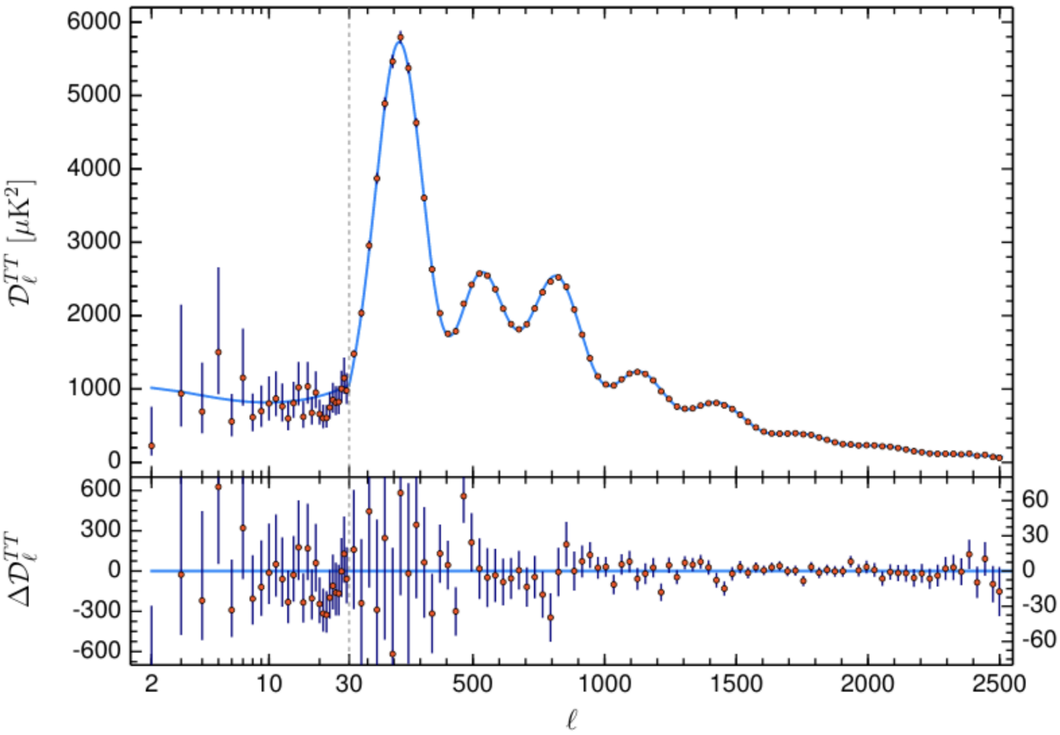

Figure 1.5: Power spectrum of the cosmic microwave background measured by the Planck satellite, along with the best fit to the ΛCDM model and residuals. Image taken from [1].

The observed third peak in the CMB power spectrum provides strong evidence for the existence and dominance of cold dark matter (CDM) at the time of recombination [20]. The relative heights of the acoustic peaks in the CMB temperature spectrum are sensitive to the ratio of baryonic matter to dark matter, with the odd-numbered peaks being enhanced by the presence of CDM [21]. The pronounced third peak is a clear indication that CDM was a significant component of the total energy density at the epoch of recombination. Measurements of the acoustic peaks in the CMB temperature spectrum have also confirmed that the Universe is nearly spatially flat, consistent with the predictions of the simplest inflationary models [1].

The Planck collaboration analyzed the observed power spectrum using the ΛCDM model. The measured spectrum reveals that dark matter must be non-relativistic, or "cold". Table 1.1 presents the most recent results from the Planck collaboration for various cosmological parameters.

Table 1.1: Cosmological Parameters with uncertainties measured by [1].

Parameter	Symbol	Value
Matter Density	Ω_M	0.315 ± 0.007
Baryon Density	Ω_b	0.0493 ± 0.0008
CDM Density	Ω_c	0.264 ± 0.004
Dark Energy Density	Ω_Λ	0.6897 ± 0.0057
Hubble Parameter	h	0.674 ± 0.005

The small observed baryon density, $\Omega_b = 0.0493 \pm 0.0008$, compared to the total matter density, $\Omega_M = 0.315 \pm 0.007$, indicates that the baryon content does not account for all of the matter content. This comparison provides strong evidence for the existence of matter that was not coupled to photons prior to recombination.

1.1.5. Big Bang nucleosynthesis

Big Bang Nucleosynthesis (BBN) offers a reliable probe of the early Universe, based on well-understood Standard Model physics. By predicting the abundances of light elements such as deuterium (D), helium-3 (^{3}He), helium-4 (^{4}He), and lithium-7 (^{7}Li), which were formed in the first three minutes after the Big Bang, BBN provides a means to test the standard hot Big Bang cosmology. The remarkable agreement between the predicted abundances and those inferred from observational data, spanning nine orders of magnitude from ^{4}He/H ~ 0.08 to ^{7}Li/H $\sim 10^{-10}$ (ratios by number), validates the standard cosmological model [22]. This agreement also allows for the use of BBN to place stringent constraints on potential deviations from the standard cosmology and on new physics beyond the Standard Model, such as the existence of dark matter.

According to the standard model of cosmology, BBN occurred within the first few minutes after the Big Bang, when the universe was hot and dense enough for nuclear fusion reactions to take place. These reactions of BBN produced light elements mentioned above in specific abundances that can be predicted by theory and measured through observations. However, the observed abundances of these elements, particularly deuterium and helium-4, cannot be fully accounted for by the known baryonic matter in the universe [22]. This discrepancy suggests the presence of an additional, non-baryonic matter which does not interact through the strong nuclear force and does not participate in BBN. The inferred amount of dark matter from BBN is consistent with other independent observations, such as the cosmic microwave background and large-scale structure formation.

The baryon-to-photon ratio η in BBN can be determined by the deuterium-to-hydrogen (D/H) ratio [23]. The concordant range of η [22] is given by:

$$\eta = (6.143 \pm 0.190) \times 10^{-10} \tag{1.11}$$

This ratio provides constraints on the baryon energy density Ω_b through the following equation:

$$\Omega_b = 3.66 \times 10^7 \eta h^{-2} \tag{1.12}$$

where h is the dimensionless Hubble parameter. Using the concordant range of η from BBN, the corresponding baryon density is:

$$\Omega_b h^2 = 0.02244 \pm 0.00069 \tag{1.13}$$

The Planck satellite measurements of the CMB in Section 1.1.4 provide an independent estimate of the baryon density with $\Omega_b h^2 = 0.02233 \pm 0.00015$ [1]. This translates to a baryon-to-photon ratio of $\eta = 6.09 \pm 0.06$, demonstrating a good agreement between the CMB and BBN measurements. This consistency indicates that approximately 5% of the Universe's energy density is baryonic. However, this value is significantly lower than the total matter energy density $\Omega_m \approx 0.3$ derived from CMB measurements [1]. Additionally, other independent observations, such as Baryon Acoustic Oscillation (BAO) measurements, also find $\Omega_m \simeq 0.3$, which is consistent with the CMB results [24]. The agreement between these independent studies further supports the evidence for the existence of non-baryonic dark matter. The discrepancy between baryon density and the matter energy density suggests that most of the matter in the Universe is non-baryonic, again providing evidence for the existence of dark matter.

The consistency between the CMB and BAO measurements, as well as their agreement with the predictions of BBN provides a remarkable confirmation that baryonic matter accounts for approximately 5% of the critical density of the Universe. The CMB data also suggests that the total matter density is roughly six times higher than the baryonic density, implying the existence of non-baryonic dark matter [1]. Furthermore, the CMB measurements have provided evidence for the presence of dark energy, which is responsible for the accelerated expansion of the Universe [25,26].

1.2. Dark matter alternatives

While it might be natural to suggest the existence of a new type of non-luminous matter that accounts for the discrepancy between the observed stellar velocities in galaxies and those predicted by classical Newtonian mechanics, others have proposed alternative hypotheses on modification of gravitational theories on large scales. One of the hypotheses that modifies Newton's second law, known as Modified Newtonian dynamics (MOND), was first introduced in 1982 by Mordehai Milgrom [27]. The main idea of Milgrom's law is that the law of motion needs to be modified when the acceleration is below a threshold a_0, which is approximately $1.2 \times 10^{-10}\,\mathrm{m/s^2}$.

For accelerations larger than a_0, Newtonian dynamics remains applicable. But when accelerations drop below a_0, the gravitational force transitions into a so-called "deep-MOND" regime where it varies inversely with the distance, which is mathematically given by

$$F_N = m \cdot \mu\left(\frac{a}{a_0}\right) \cdot a \tag{1.14}$$

where:

- F_N is the modified Newtonian force experienced by a mass m,
- a is the acceleration,
- a_0 is the critical acceleration below which Newton's law is modified,
- $\mu(x)$ is an interpolation function that transitions between the Newtonian regime ($\mu(x) = 1$ for $x \gg 1$) and the MOND regime ($\mu(x) = x$ for $x \ll 1$).

The MOND theory leads to flat rotation curves in galaxies without resorting to dark matter, resulting in a slower decrease of gravitation attraction with large distances compared to traditional Newtonian physics. This alternation of gravitational behavior aligns with the mass distribution observed in galaxies without involving additional particles. MOND was initially conceived as a weak-field approximation within a broader theoretical context, and more modified gravity theories emerged after it. For instance, AQUAdratic Lagrangian theory (AQUAL) modifies the gravitational term in the classical Lagrangian. Instead of relying on a quadratic dependency on the gradient of the Newtonian potential, it introduces a more general functional form, resulting in MOND-like behavior. AQUAL does not align with General Relativity principles and was subsequently evolved into a relativistic theorem, known as relativistic AQUAL (RAQUAL) [28].

Although MOND has offered insights into certain galactic phenomena, it falls short in explaining broader cosmic observations, such as galaxy cluster dynamics and CMB anisotropies. These limitations highlight its shortcomings compared to the dark matter framework [29]. The consensus favors dark matter as the more convincing explanation for these phenomena. This has led to extensive research and experimentation in astrophysics, cosmology, and high-energy physics to uncover the universe's nature.

1.3. Dark matter candidates

Throughout the late 20th century, a series of observations reinforced the existence of dark matter. Evidence includes the gravitational lensing of galaxy clusters on distant objects, the thermal distribution of hot gasses within galaxies and clusters, and the distinct variations observed in the cosmic microwave background. The exploration of dark matter is focused on a broad spectrum of candidates, spanning from astrophysical objects to hypothetical particles that extend beyond the Standard Model of particle physics.

On one hand, astrophysical objects such as Massive Compact Halo Objects (MACHOs), which include black holes, neutron stars, and brown dwarfs, as well as Primordial Black Holes (PBHs), offer a more tangible but still elusive explanation for dark matter. While some of these objects, such as neutron stars and brown dwarfs, are composed of baryonic matter, others, like black holes, are vacuum solutions of general relativity and do not consist of dark matter themselves. However, if these objects exist in sufficient numbers, they could potentially account for a significant portion of the missing mass in the Universe. It is important to note that the cosmological evidence discussed above, such as the cosmic microwave background and Big Bang nucleosynthesis, cannot be fully explained by the presence of MACHOs like brown dwarfs or neutron stars. These objects, being composed of baryonic matter, would contribute to the total baryonic density of the Universe, which is already well-constrained by CMB and BBN observations [1]. Therefore, while MACHOs could potentially account for some of the missing mass on galactic scales, they cannot explain the majority of the dark matter in the Universe, which is non-baryonic in nature.

On the other hand, particle physics proposes a wide array of theoretical particles as dark matter candidates, extending beyond the Standard Model. Among the most promising candidates are Weakly Interacting Massive Particles (WIMPs), which have gained significant attention due to their potential to naturally explain the observed dark matter abundance through the freeze-out mechanism. WIMPs are hypothesized to have masses ranging from a few GeV to several TeV and interact with ordinary matter only through weak nuclear force and gravity.

Another intriguing particle dark matter candidate is the axion, a light pseudoscalar particle originally proposed to solve the strong CP problem in quantum chromodynamics. Axions are expected to have extremely small masses and interact very weakly with ordinary matter, making them difficult to detect directly. However, their potential to form a coherent field that permeates the Universe has led to innovative search strategies, such as axion haloscopes and helioscopes.

1.3.1. Astrophysical objects

Massive Compact Halo Objects (MACHOs) are a category of baryonic dark matter candidates that are non-luminous, including black holes, neutron stars, brown dwarfs, and rogue planets. A MACHO can be detected through gravitational microlensing, when it crosses or nearly crosses the line of sight to a star. The gravitational field of the MACHO bends the light from the star, making it momentarily bright. The EROS-2 collaboration undertook microlensing surveys targeting bright stars within the Milky Way to investigate the proportion of the galaxy's halo mass that could be attributed to MACHOs in the mass range of $6 \times 10^{-8} M_{\odot}$ to $15 M_{\odot}$ ($M_{\odot}$ denotes the mass of the Sun). The findings indicated that MACHOs account for less than 8% of the Milky Way's halo mass [30]. Moreover, constraints on MACHOs with masses ranging from $10 M_{\odot}$ to several thousand $M_{\odot}$ were derived from the required growth timescale of star clusters in ultra-faint dwarf galaxies, which should be less than the estimated age of the galaxies [31]. These analyses, along with other independent studies, effectively rule out MACHOs as the sole constituents of dark matter for masses above $10^{-7} M_{\odot}$.

Expanding upon the exploration of MACHOs as potential dark matter components, which accounts for a small fraction of dark matter, Primordial Black Holes (PBHs) arise as another significant non-particle candidate for dark matter, potentially constituting a substantial part of it. PBHs are hypothetical black holes that form in the early universe's high-density conditions before Big Bang nucleosynthesis (BBN). Existing research has significantly limited the parameter space for dark matter, yet a wide range remains open, where PBHs with asteroid-sized masses (ranging from 10^{-15} to $10^{-10} M_{\odot}$) could constitute the entire dark matter content. Additionally, LIGO recently detected that PBHs can be considered as a viable explanation for the cluster of merging black holes, each approximately $30M_{\odot}$. In this specific mass range, it's feasible that PBHs could account for a significat fraction, approximately 10%, of the overall dark matter [32].

1.3.2. Weakly Interacting Massive Particles

In the 1980s, a decade after the recognition of the dark matter problem by Rubin, Ford, and Freeman's work, the concept of Weakly Interacting Massive Particles (WIMPs) emerged as a potential solution. It has been a prime candidate to be searched for through direct dark matter detectors. The theoretical existence of WIMPs could address several astrophysical and cosmological dilemmas associated with the puzzles of dark matter.

WIMPs are theorized to be relic particles from the early universe, a period characterized by thermal equilibrium among particles. During this high-temperature phase of the early universe, dark matter particles and their antiparticles were continuously created from and annihilated into lighter particles. As the universe expanded and its temperature dropped, the thermal energy of these lighter particles decreased, eventually falling below the threshold needed to produce dark matter particle-antiparticle pairs. Despite this, the annihilation of existing dark matter particle-antiparticle pairs continued, leading to an exponential decline in their number density. [33]

As the universe continued expanding over time, the interaction rate between dark matter particles and their antiparticles decreased until it ceased, resulting in a stable number of dark matter particles [34]. This is referred as the 'freeze-out' point, illustrated in Figure 1.6.

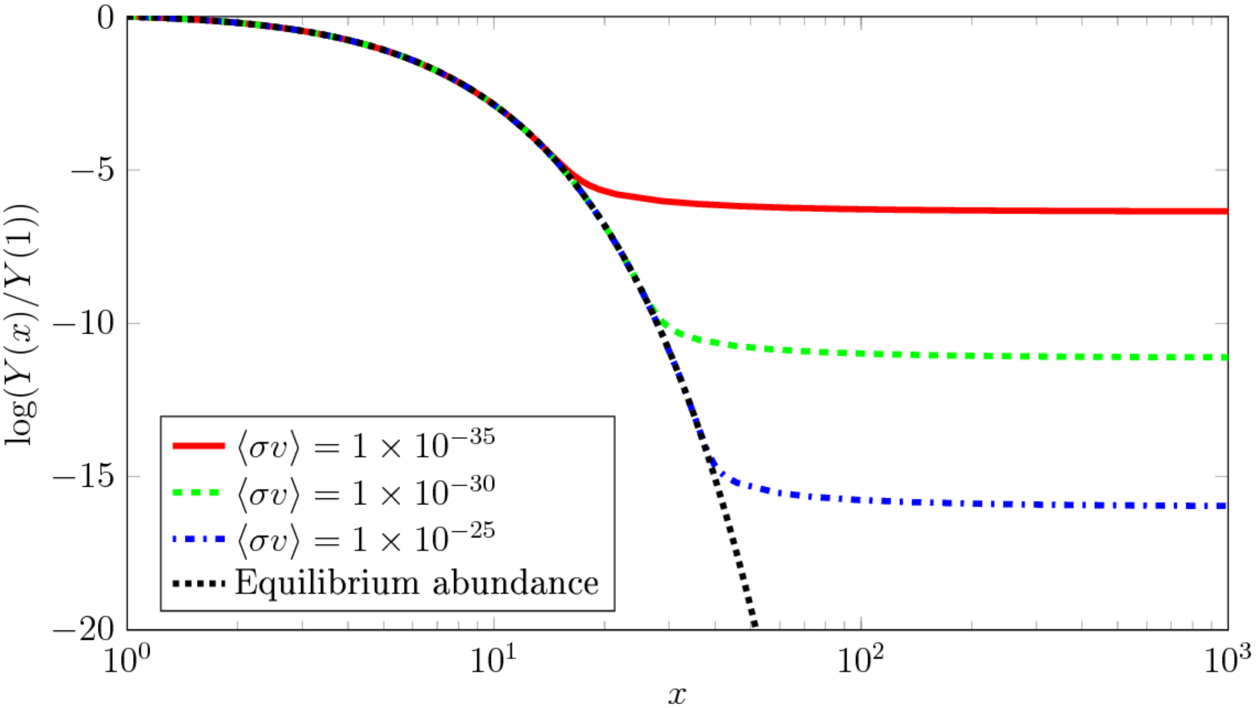

Figure 1.6: Evolution of the WIMP number density Y over time. The black line represents the equilibrium abundance. The colored dashed lines represent the true abundance for various $\langle \sigma v \rangle$, which is the thermal average of the annihilation cross-section multiplied by the relative velocity of the particles. Image taken from [35].

The size of the interaction cross section determines their abundance. The rate at which dark matter particles annihilate in the early stages of the Universe is given by:

$$\Gamma = n_\chi \langle \sigma v \rangle \tag{1.15}$$

where the dark matter annihilation rate Γ is the product of two key factors: the number density of dark matter particles n_χ and the thermal average of the annihilation cross-section σ multiplied by the relative velocity v of the particles. Therefore, particles with a larger thermally-averaged cross section would have undergone annihilation for a more extended period, resulting in a lower residual number density when the annihilation ceased.

Given the current estimated abundance of dark matter in the universe, the interaction cross section for dark matter particle-antiparticle annihilation is inferred to be roughly equal to that of the weak interaction [33]. This similarity in cross-section is a major motivation for the WIMP dark matter hypothesis, as it suggests that dark matter particles could have been produced thermally in the early universe and then frozen out as the universe expanded and cooled. If the annihilation cross-section were significantly lower than the weak scale, the relic abundance of dark matter would be too high compared to observations. Conversely, if the cross-section were much higher, the relic abundance would be too low. The fact that the inferred cross-section is comparable to the weak scale is known as the "WIMP miracle", which has driven much of the interest in WIMP dark matter candidates [36]. This leads to the conclusion that if dark matter consists of such relic particles, they would possess the characteristics of WIMPs, making them a prime target for direct detection experiments.

While the WIMP model provides a promising explanation for the nature of dark matter, it requires physics beyond the Standard Model (SM) to accommodate it, as there are no suitable WIMP candidates within the SM. Despite this limitation, the WIMP model has remained a central focus of research in the effort to unravel the mysteries of the universe's dark matter component. Another primary reason why WIMPs were considered a natural dark matter candidate is that many realizations of supersymmetry (SUSY), a theoretical extension of the SM, contain stable WIMP candidates. Prior to the operation of the Large Hadron Collider (LHC), it was anticipated that supersymmetry would be discovered, potentially including a natural dark matter candidate. Although the LHC has not yet yielded evidence for supersymmetry [37], WIMPs remain a viable and widely studied dark matter candidate.

1.3.3. QCD axions

The axion is a hypothetical particle initially proposed to resolve the strong CP problem in quantum chromodynamics (QCD), which has aslo emerged as a matter candidate. The

Standard Model of elementary particles successfully describes fundamental interactions but leaves a puzzle regarding the strong interactions. Although the strong and electromagnetic interactions are observed to conserve parity (P) and charge-parity (CP), the weak interactions' violation of P, C, and CP is expected to induce P and CP violation in the strong interactions within the SM, which is inconsistent with observations. This inconsistency is known as the Strong CP Problem. The extent of parity and charge-parity violation in the strong interactions is governed by a parameter called θ_{QCD}, which serves as the coefficient of the odd terms in the action density under both P and CP transformations.

Shortly after the identification of the Strong CP Problem, Peccei and Quinn introduced a modification to the Standard Model that provides a potential solution [38]. They proposed a $U_{PQ}(1)$ symmetry with three key properties: it is an exact symmetry of the classical action, it undergoes spontaneous symmetry breaking, and it possesses a color anomaly, meaning that it is explicitly broken by non-perturbative QCD instanton effects that cause physics to depend on the value of θ_{QCD}. By following this approach, the parameter θ_{QCD} is substituted with $a(x)/f_a$, where $a(x)$ is a dynamical pseudo-scalar field and f_a is a quantity with the dimension of energy, known as the axion decay constant. The value of f_a is on the order of the vacuum expectation value responsible for the spontaneous breaking of the $U_{PQ}(1)$ symmetry, and $a(x)$ is the corresponding Nambu-Goldstone boson.

Weinberg and Wilczek highlighted that the non-perturbative instanton effects, which cause physics to depend on θ_{QCD}, generate an effective potential for $a(x)$ [39, 40]. Subsequently, it was demonstrated that the minimum of this effective potential occurs at $a(x) = 0$ [41]. The Strong CP Problem is resolved once the $a(x)$ field reaches this minimum.

The Peccei-Quinn mechanism alters the low-energy effective theory of the SM by introducing a light pseudo-scalar particle called the "axion", which is the quantum of the $a(x)$ field. The characteristics of the axion, including its mass m_a and interaction strengths, are primarily determined by the value of the axion decay constant f_a, with both m_a and the interaction strengths being inversely proportional to f_a given by

$$m_a^2 \approx \frac{f_\pi^2 m_\pi^2}{f_a^2} \frac{m_u m_d}{(m_u + m_d)^2} \tag{1.16}$$

where axion mass m_a can be expressed as a function of several parameters, including the pion decay constant $f_\pi \approx 93$ MeV, the pion mass m_π, and the masses of the up and down quarks (m_u and m_d) [39]. When f_a assumes a large value, the resulting axions will have low masses and are typically generated in low-momentum modes, exhibiting non-relativistic behavior. In this misalignment mechanism, the axion field initially has a non-zero value throughout space, which is determined by the angle θ_i. As the universe expands and cools, the axion field begins to oscillate around the minimum of its potential, behaving like a coherent state of low-momentum axions. The energy density of these oscillations contributes to the cold dark matter density in the universe. The amount of axion dark matter produced through the misalignment mechanism depends on the initial misalignment angle θ_i and the axion decay constant f_a. These properties make axions promising candidates for cold dark matter [42].

As a result of the symmetry breaking, the axion is predicted to be a neutral, pseudoscalar Nambu-Goldstone boson. While the original axion model proposed by Peccei and Quinn has been ruled out by experimental constraints [43], other axion models, such as the invisible axion [44] and axion-like particles, remain viable candidates for dark matter.

1.3.4. Axion-like particles

Axion-like particles (ALPs), while not providing the solution to the strong CP problem, are less constrained in their theoretical properties and are also considered as potential dark matter candidates. They are not constrained by the specific relation between their coupling strength and mass, implying their breaking scale f_a does define their mass m_{ALP}. ALPs are predicted to have a broader mass range compared to QCD axions, with the eV to keV scale being of particular interest. Some of their mass range overlaps with the parameter space explored by experiments searching for WIMPs and light dark matter (LDM) candidates [44].

ALPs can interact with bound electrons in atoms through a process named the axio-electric effect [45], which is analogous to the photoelectric absorption of Standard Model photons. In this interaction, an ALP (denoted by a in Eq. 1.17) is absorbed by a bound electron and then resulted in the liberation of the electron from the atom [45]. The axio-electric cross-section is given by:

$$\sigma_a(E_a) = \sigma_{pe}(E_a)\frac{g_{ae}^2}{\beta}\left(\frac{3E_a^2}{16\pi\alpha m_e^2}\right)\left(1-\frac{\beta^{2/3}}{3}\right) \tag{1.17}$$

where α is the fine structure constant, m_e is the mass of the electron, and β is defined as the ratio of the axion's velocity to the speed of light. The strength of this coupling is characterized by the axio-electric coupling constant, denoted as g_{ae}. The axio-electric effect can also be applied for the detection of solar axions, which will be discussed in more detail in the following section.

For non-relativistic ALPs, the cross-section can be simplified to a form that depends only on the ALP mass, instead of the total energy. The axio-electric cross-section is then simplified to:

$$\sigma_a(m_a) = \sigma_{pe}(m_a c^2)\frac{g_{ae}^2}{\beta}\left(\frac{3m_a^2}{16\pi\alpha m_e^2}\right) \tag{1.18}$$

Assuming that all dark matter is composed of non-relativistic ALPs, the interaction rate of ALP absorption can be calculated using the simplified cross-section, the dark matter density, and the speed of light. The interaction rate is given by:

$$R_a(m_a) = \rho_{\mathrm{DM}} \sigma_{pe}(m_a c^3) \frac{3 g_{ae}^2 m_a}{16 \pi \alpha m_e^2} \tag{1.19}$$

This interaction rate can be used to set limits on the axio-electric coupling constant as a function of the ALP mass, as demonstrated in various experimental studies. The expected signal for a given ALP mass is a Dirac delta function at the mass-equivalent energy, broadened by the energy resolution of the detector. A result [46] from the SuperCDMS Soudan experiment on the axio-electric coupling constraints with ALPs is shown in Figure 1.7. The ALP mass range covered in the figure spans from 40 eV/c^2 to 500 keV/c^2.

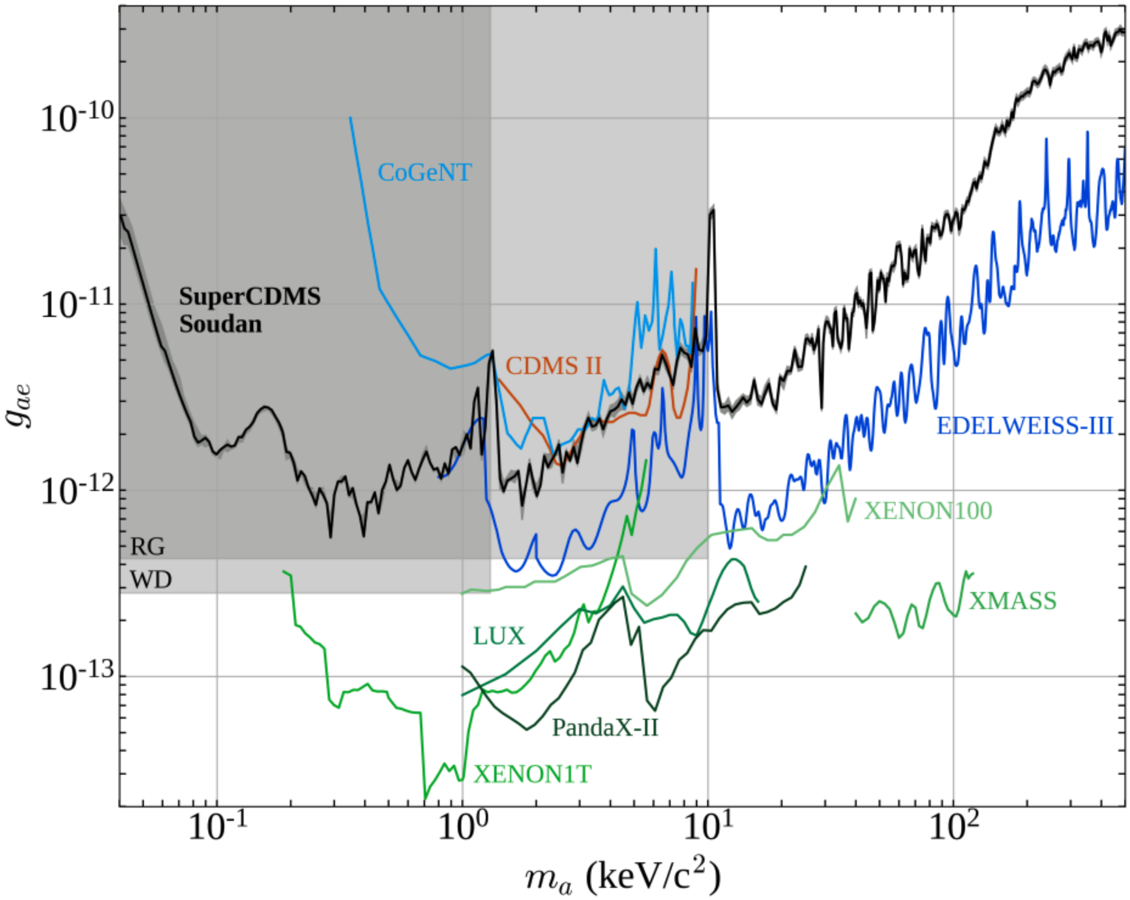

Figure 1.7: SuperCDMS Soudan upper limit (solid black) with uncertainty band (shaded grey) on the axio-electric coupling. Image taken from [46].

Figure 1.7 also includes results with limits set by other direct detection experiments such as CDMS II [47], CoGeNT [48], EDELWEISS-III [49], LUX [50], PandaX-II [51], XENON100 [52], XENON1T [53], and XMASS [54]. The shaded regions in the figure are excluded by the observed cooling of red giant [55, 56] and white dwarf stars [56, 57]. In the next section, constraints by astrophysical observations will be discussed in more detail and additional theoretical limits will be introduced.

1.4. Constraints on g_{ae}

The axio-electric coupling constant g_{ae} characterizes the interaction strength between axions and electrons, and its value can vary significantly based on different assumptions from specific axion models. Various theoretical frameworks propose different mechanisms for axion-electron interactions, resulting in a range of possible coupling strengths. While theoretical models offer a broad parameter space to explore, astrophysical observations provide essential constraints on g_{ae}. Studies of white dwarf cooling rates and the evolution of red giant stars have set upper limits on g_{ae}, which have thereby narrowed the range of feasible coupling constants and provided insights on diverse experimental approaches in the search for axions.

1.4.1. Astrophysical constraints

Axions and ALPs may influence stellar evolution due to their interactions with photons, electrons, and nucleons. These particles can be produced within the stellar core and then readily escape the star due to their weak interactions. As a result, axions and ALPs could potentially influence the rate of energy dissipation in stars, thereby affecting their longevity and other properties.

The astrophysical consequences of axions and ALPs have been utilized to constrain their properties, yielding the most stringent bounds on most axion-electron couplings. Comparing theoretical models that include axions and ALPs with observational data on stellar evolution has established upper limits on the strength of their interactions with standard model particles. The possibility of constraining the axion-electron coupling constant g_{ae} is particularly important within the dense cores of white dwarfs (WDs) and Red Giant Branch (RGB) stars, where bremsstrahlung emission is the dominant process. [58]

White dwarfs are low-mass stars in the late stages of their evolution, after exhausting their nuclear fuel. Their subsequent evolution is governed by a cooling process driven by photon and neutrino emission. However, the presence of an exotic cooling mechanism could manifest itself in two ways. Firstly, the shape of the White dwarf luminosity function (WDLF) could be altered. Comprehensive WDLF measurements have revealed a small discrepancy with theoretical predictions, suggesting an additional cooling mechanism at a 2σ significance level. When interpreted as evidence for a non-zero axion-electron coupling constant g_{ae}, these results [59, 60] indicate a range of

$$g_{ae} = (1.5^{+0.6}_{-0.9}) \times 10^{-13} \qquad (95\% \text{ C.L.}) \tag{1.20}$$

Secondly, direct observations of periodic changes in variable WDs can confirm the existence of an exotic cooling mechanism. These stars exhibit luminosity oscillations, which enables direct measurements of their cooling rates. However, this calculation requires decades-long observations and only a few stars are currently available. In these cases, the measured rate of change is faster than predicted, suggesting an additional cooling channel. When interpreted in terms of axion production mediated by g_{ae}, these observations also suggest values of g_{ae} on the order of a few times 10^{-13}.

The tip of the red giant branch represents the maximum luminosity achieved by RGB stars right before they reach the conditions necessary to ignite helium in their cores, a process known as the helium flash. It serves as another valuable observable for constraining the axion-electron coupling constant g_{ae}. Initially, this observable was studied for two globular clusters, namely M5 [61] and M3 [62]. Recent studies have extended the analysis to a larger number of clusters with improved data quality in distance determinations. These studies [63,64] have yielded an upper limit of

$$g_{ae} < 1.3 \times 10^{-13} \qquad \text{(95\% C.L.)} \tag{1.21}$$

Combining results [65] from the WDLF, the WD pulsation measurements, and RGB star observations led to an axion solution with a statistical significance slightly exceeding 3 standard deviations in the fit range of

$$g_{ae} = (1.6^{+0.29}_{-0.34}) \times 10^{-13} \qquad (1\sigma) \tag{1.22}$$

1.4.2. Theoretical Constraints

The Kim-Shifman-Vainshtein-Zakharov (KSVZ) and Dine-Fischler-Srednicki-Zhitnitsky (DFSZ) models are two well-known theoretical frameworks proposed to explain the existence of axions. The KSVZ model, introduced by Kim and later expanded by Shifman, Vainshtein, and Zakharov, proposed that axions are the result from the introduction of a new heavy quark that couples to the Peccei-Quinn symmetry, which spontaneously breaks at a high energy scale and lead to the axion as a pseudo-Nambu-Goldstone boson [66]. In contrast, the DFSZ model, developed by Dine, Fischler, Srednicki, and Zhitnitsky, suggests a different mechanism involving additional Higgs fields and standard model quarks. It assumes that axions emerge as a result of these fields and the Peccei-Quinn symmetry [67]. Both models aim to provide a natural solution to the strong CP problem by predicting a very light, weakly interacting particle that could also be a candidate for dark matter in the universe.

The KSVZ model introduces a new heavy quark and a singlet complex scalar to the Standard Model, which results in the spontaneous breaking of PQ symmetry with a vacuum expectation value (VEV) – f_A. This f_A can be set much higher than the electroweak scale. In the original KSVZ model, the new fermion is uncharged with an E/N ratio of 0, where E and N are the electromagnetic and color anomaly coefficients respectively. If the new heavy quark has a hypercharge similar to down-type (up-type) quarks, the E/N ratio becomes 8/3 (2/3). The KSVZ model can be extended to include additional colored fermions and scalars, resulting in different E/N values. However, stability constraints limit E/N to the range (5/3, 44/3) and adding the constraints to g_{ae} accordingly. A key feature of these models is the lack of an axion-electron coupling at tree level, granting them the name "hadronic axions", which will be discussed further in the next section.

On the other hand, the DFSZ model assigns PQ charges to Standard Model quarks, allowing them to carry the PQ anomaly without introducing new exotic fermions. The scalar sector is expanded to include two Higgs doublets, giving mass to up-type and down-type fermions. Additionally, a new singlet complex scalar would set an independent PQ symmetry scale. Unlike the KSVZ model, DFSZ features axion-lepton couplings, particularly with electrons. Depending on which Higgs participates in the leptons' Yukawa term, the model has two variants: DFSZ-I and DFSZ-II, with E/N ratios of 8/3 and 2/3, respectively. This E/N ratios result in the theoretical constraints on the axion-lepton couplings. [58]

1.5. Solar axions

QCD axions and axion-like particles can be produced in astrophysical sources. In particular, the Sun is expected to generate substantial amounts of axions and ALPs. These particles arise from a variety of processes occurring within the sun's interior, such as the Primakoff effect, Axio recombinations and deexcitation, bremsstrahlung, and Compton scattering [68]. These solar axions and ALPs can then stream out of the Sun and potentially be detected by Earth-based experiments.

The detection of solar axions and ALPs could provide valuable insights into the fundamental properties of these particles and their interactions with matter, such as their coupling strengths to photons and electrons. In this section, the topic of solar axions will be explored, including their production mechanisms, expected flux, and expected event rate in detectors using the previously mentioned axio-electric effect.

1.5.1. Solar axion flux

Outside the scope of dark matter detection, the experimental discovery of axions is most feasible in the mass range of ~ 10 keV up to 1 MeV. Axions that are primarily produced at the core of the sun are known as solar axions. In the solar interior, which is a well-understood weakly coupled plasma, relatively precise calculations of axion production reactions can be performed. The axion flux is primarily determined by two key parameters: the axion-two-photon coupling and the axion-electron coupling. The former drives the Primakoff production of axions, which occurs when photons collide with charged particles in the solar plasma, as described by:

$$\gamma + Q \rightarrow a + Q \tag{1.23}$$

where Q is any charged particle.

In hadronic models, including the KSVZ model, there is no axion-electron coupling at the tree level. Instead, axions can couple to photons through a $g_{a\gamma\gamma}$ term, which leads to axion-to-photon oscillation or conversion in the presence of an electromagnetic field.

The axion-photon coupling $g_{a\gamma\gamma}$ emerges from the interaction between axions and the electromagnetic field, and the one-loop order is introduced by the corrections from the interaction of axions with virtual particles in the loop. In hadronic axion models, the primary contributions to this coupling come from loops containing charged hadrons, such as pions. The effective coupling can be written as [69]:

$$\mathcal{L}_{a\gamma\gamma} = g_{a\gamma\gamma} a F_{\mu\nu} \tilde{F}^{\mu\nu} \tag{1.24}$$

The resulting effective interaction between axions and photons can be written as [70]:

$$g_{a\gamma\gamma} = \frac{\alpha}{2\pi f_a}\left[\frac{E}{N} - 1.92(4)\right] = \left[0.203(3)\frac{E}{N} - 0.39(1)\right]\frac{m_a}{\mathrm{GeV}^2}. \tag{1.25}$$

where α is the fine-structure constant, f_a is the axion decay constant, E and N are the electromagnetic and color anomaly coefficients, respectively. In grand unified theories, such as the DFSZ model, the ratio E/N = 8/3, and E/N = 0 if the newly introduced heavy quark is electrically neutral [22]. This interaction is mediated by loop diagrams involving charged particles and enables the detection of axions by converting them into photons, providing a viable method for identifying these particles.

On the other hand, in non-hadronic axion models, axions can couple to electrons at tree level, driving several reactions that would significantly overshadow the Primakoff flux. Their corresponding effective Lagrangian density with electrons is given by:

$$\mathcal{L} = -i g_{ae} a \bar{\psi}_e \gamma_5 \psi_e \tag{1.26}$$

where a denotes the axion field, ψ_e represents the electron spinor field, and g_{ae} stands for the Yukawa coupling between axions and electrons. The value of g_{ae} is determined by the following equation:

$$g_{ae} = \frac{C_{ae} m_e}{f_a} \tag{1.27}$$

where f_a is the axion decay constant and $C_{ae} \sim \mathcal{O}(1)$ is a model-dependent coefficient. Lorentz-Heaviside units were adopted here, with $\hbar = c = k_B = 1$ set accordingly [71].

When the axion-electron coupling constant is present, the solar axion flux would be dominated by reactions including Axio recombinations and deexcitation, Bremsstrahlung, and Compton scattering, abbreviated as the "ABC" reactions. Figure 1.8 includes the Feynman diagrams representing these processes. These processes involve interactions between axions and electrons, and their relative contributions to the total solar axion flux. The total flux can be calculated using available libraries of monochromatic photon radiative opacities [71].

The ABC sub-processes can be expressed as follows:

- Axio-recombination (free-bound transition): $e + I \rightarrow I^- + a$
- Axio-deexcitation (bound-bound transition): $I^* \rightarrow I + a$
- Electron-Ion bremsstrahlung (free-free transition): $e + I \rightarrow e + I + a$
- Electron-electron bremsstrahlung: $e + e \rightarrow e + e + a$
- Compton scattering (photo production): $\gamma + e \rightarrow e + a$

where I stands for ions and I^* for their excited states.

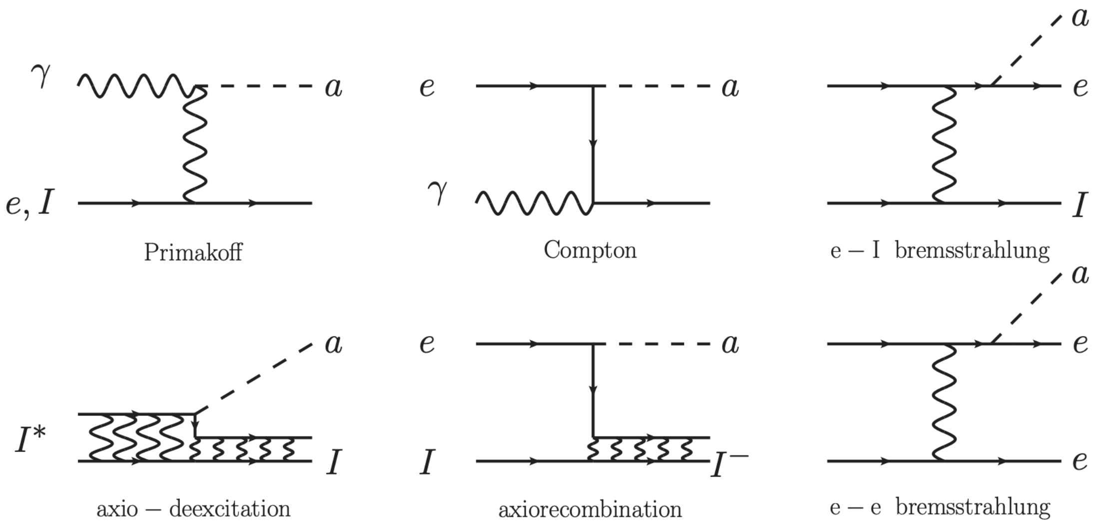

Figure 1.8: ABC reactions responsible for the solar axion flux in non-hadronic axion models. Image taken from [71].

To determine the solar axion flux, it is essential to consider the contributions from each of the ABC sub-processes. The relative importance of these processes depends on the solar environment and the specific properties of the axion, such as its mass and coupling strength to electrons. By taking into account the various interaction channels and utilizing accurate radiative opacity data, the solar axion flux could be obtained in a more precise estimate.

Calculations of solar axion flux were conducted by utilizing available libraries of monochromatic photon radiative opacities, such as OP [72], LEDCOP [73], and OPAS [74]. The results in Figure 1.9 revealed approximately 30% larger flux than previous estimations in [75], primarily due to the addition of atomic recombination (free-bound electron transitions) and deexcitation (bound-bound) processes [71]. The relative importance for the total flux Φ through each process has a ratio of

$$\Phi_B : \Phi_C : \Phi_A = 64.9 : 7.6 : 27.6 \tag{1.28}$$

Figure 1.9 presents the results from Redondo [71], showing the total solar axion flux from ABC reactions in comparison to the flux from the Primakoff effect alone. This comparison enables a more precise search for solar axions.

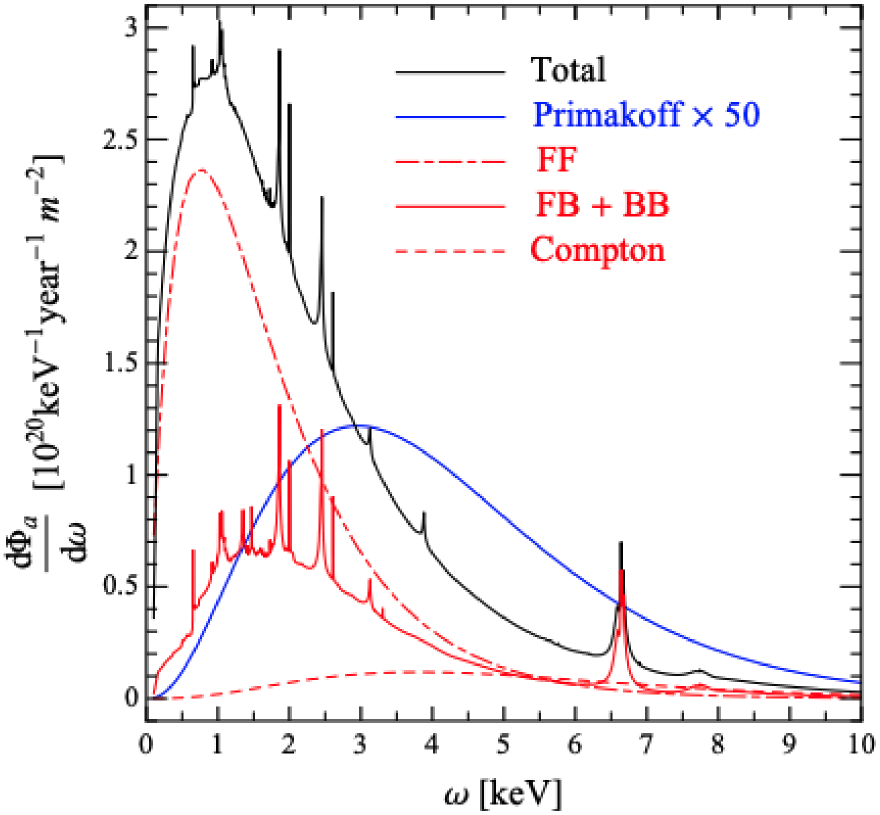

Figure 1.9: Flux of solar axions due to ABC reactions driven by the axion-electron coupling (for $g_{ae} = 10^{-13}$). The different contributions are shown as red lines: Atomic recombination and deexcitation (FB+BB, solid), Bremsstrahlung (FF, dot-dashed) and Compton (dashed). The Primakoff flux from the axion-photon coupling was calculated using a typical value of $g_{a\gamma} = 10^{-12}$, and $g_{ae} = 10^{-13}$ was used for the ABC processes. Note that the Primakoff flux has been scaled up by a factor of 50 in the figure to enhance its visibility. Image taken from [71].

1.5.2. Axio-electric effect

Detection of solar axions also relies on axions' couplings to electrons through the axio-electric effect [45], which is given by:

$$a + e + Z \rightarrow e + Z \tag{1.29}$$

This process is similar to the photoelectric effect, while an axion is absorbed instead of a photon. In the process of the detector absorption, where $\sigma_{pe}(E_a)$ is the photoelectric cross section between the electron of the target material's atom and photon, the cross section of axion and electron is described by:

$$\sigma_{ae}(E_a) = \sigma_{pe}(E_a)\frac{g_{ae}^2}{\beta}\left(\frac{3E_a^2}{16\pi\alpha m_e^2}\right)\left(1 - \frac{\beta^{2/3}}{3}\right) \tag{1.30}$$

where the calculation is identical to relativistic ALPs in Eq. 1.17. When the axion mass m_a is nearly equivalent to the axion energy E_a, β tends to approach zero. Under such circumstances, the cross-sectional interaction between axions and electrons, $\sigma_{ae}(E_a)$, undergoes a significant rise and approaches infinity. Figure 1.10 shows the axio-electric cross section in germanium detectors for several example axion masses, which provides a clear comparison of how different axion masses affect the cross section values. It is important to note that the axion energy is always slightly greater than the axion mass to ensure a finite cross section.

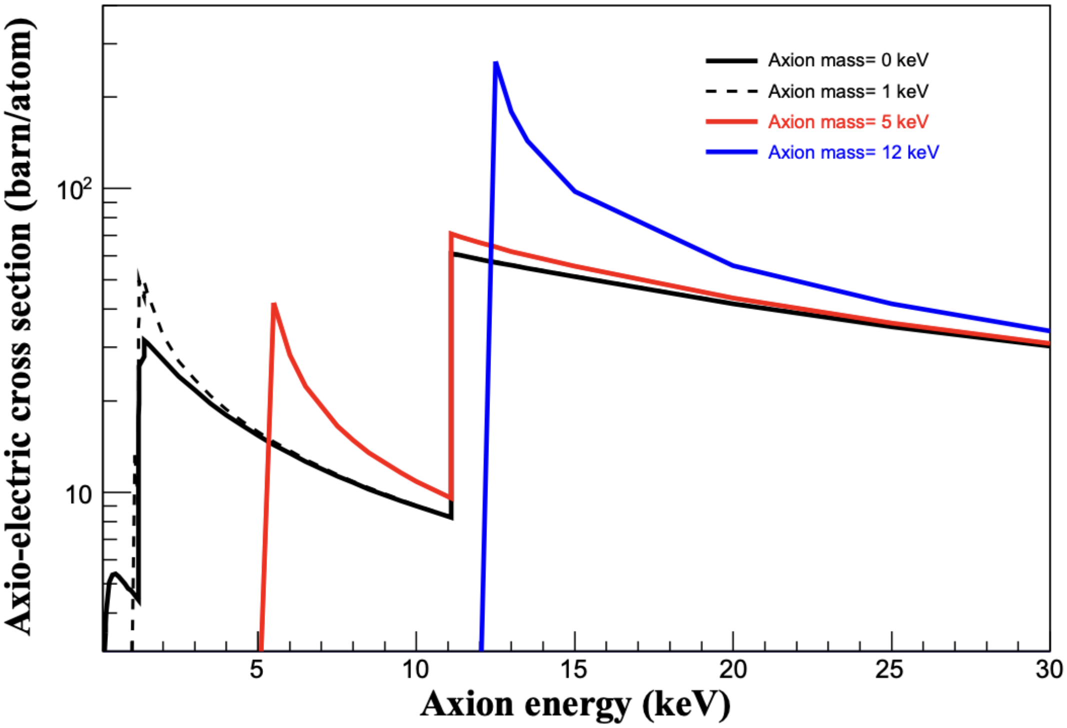

Figure 1.10: Axio-electric cross section for different axion masses, computed for germanium and normalized with $g_{ae} = 1$. Example plots from EDELWEISS [76] show axion energies when they are slightly larger than the axion masses. Image taken from EDELWEISS-II experiment [76].

The axion flux, driven by the axion-electron coupling through ABC reactions, is given by $\Phi_a^{ABC} \propto g_{ae}^2$. The differential event rate, which accounts for the axio-electric process in detection, is given by:

$$\frac{dR}{dE_r} = \frac{N_A}{A} \left(\frac{d\Phi_a^{\mathrm{ABC}}}{dE}(E_r) \right) \sigma_{ae}(E_r) \tag{1.31}$$

where N_A is the Avogadro constant, A is the atomic weight of detector materials, and E_r is the electronic recoil energy. The expected event rate in axion detectors depends on the axion flux, the axio-electric cross-section, and the properties of the detector like energy resolution.

The study of solar axions and their detection through the axio-electric effect is an important aspect of the axion search, and the detection method with more details will be further discussed in the next chapter. As the search for axions continues, improvements in detection technologies, background reduction techniques, and data analysis methods will be essential to enhance the sensitivity of both dark matter and axion experiments. The ongoing efforts to detect solar axions through the axio-electric effect, combined with other complementary searches, will contribute to unraveling the mystery of axions, and potentially provide solutions to the strong CP problem and the dark matter mystery.

Chapter 2

Dark Matter and Axion Detection

One of the major objectives in modern physics is the detection of particles, where physicists utilize advanced technologies and methodologies to explore the fundamental constituents of matter. The search for elusive particles, such as WIMP particles and axions, utilizes a wide range of innovative searching strategies in experimental physics. These searching approaches can be broadly categorized into direct, indirect, and production detection methods.

2.1. Dark Matter Detection

Direct and indirect detection methods are two primary experimental strategies to detect dark matter, each offering unique insights through distinct approaches. Direct detection experiments focus on observing interactions between dark matter particles and ordinary matter within detectors on Earth, including underground detectors shielded from cosmic ray interference. These experiments typically rely on the subtle recoil of nuclei or electrons within a target material as a result of collisions with dark matter particles, such as WIMPs. Indirect detection, on the other hand, aims to identify the byproducts of dark matter interactions or annihilations occurring in space. This approach hinges on observing gamma rays, neutrinos, and other cosmic rays that could result from dark matter particles colliding and annihilating each other in regions of high mass density, such as the centers of galaxies or the Sun. Both methods are complementary, covering different aspects of detection and diverse potential properties of dark matter.

Additionally, accelerator-based experiments provide another aspect to the dark matter search through particle production. These experiments typically accelerate particles like protons or electrons close to the speed of light and collide them with other particles in the hope of generating dark matter directly. Collision outcomes are then analyzed in search of signs such as missing transverse energy or momentum discrepancies, which may indicate elusive dark matter particles. Collectively, these approaches progressively advance the understanding of one of the most profound mysteries of dark matter. The diagram in Figure 2.1 illustrates these key methods employed in the search for dark matter, including direct detection, indirect detection, and particle production at high-energy accelerators.

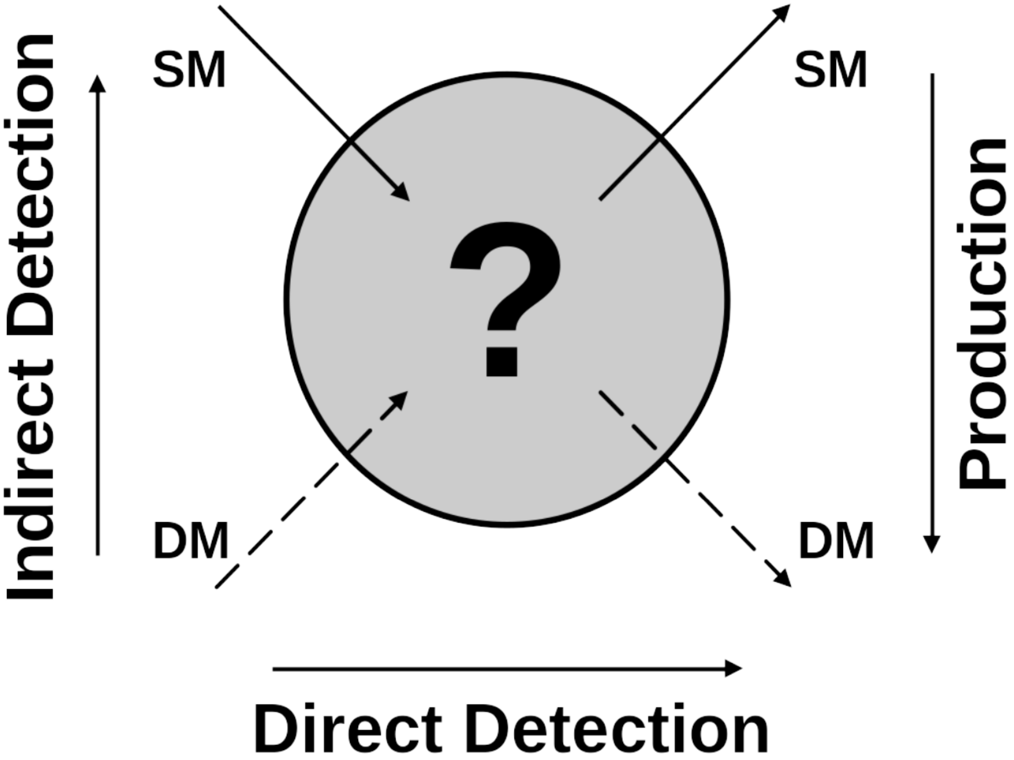

Figure 2.1: Representation of the general search strategies for particle dark matter. Image taken from [77].

Direct detection experiments search for evidence of dark matter interacting with Standard Model particles, illustrated as the left-to-right process in Figure 2.1. Indirect detection aims to identify the byproducts of dark matter annihilation into Standard Model particles, represented by the bottom-to-top process on the left side. The top-to-bottom process on the right demonstrates the method of creating dark matter particles using high-energy particle accelerators through production.

2.1.1. Production at accelerators

Research on dark matter through accelerator-based experiments utilizes various innovative strategies to detect or produce particles beyond the Standard Model (BSM). These strategies include direct production at high-energy accelerators, where particles such as protons or electrons are accelerated to relativistic speeds and collided, potentially generating BSM particles. Facilities including the Large Hadron Collider (LHC) and others engage in such searches, aiming to identify the elusive components of dark matter through the missing transverse momentum in the collision signature. This missing transverse momentum could be an indication of dark matter particles that escape detection. Searches for BSM particles have been conducted at various major accelerators over the past decades, with each new generation of machines achieving higher energy scales. While the LHC currently operates at the TeV scale, earlier accelerators functioned at a lower energy range. This progression in energy has been made possible by constructing larger and more powerful accelerators [36].

At LHC, proton-proton collisions are executed at high energies, where two rings of high-relativistic protons collide at predetermined interaction points within the large detectors, including the Compact Muon Solenoid (CMS) [78] and A Toroidal LHC Apparatus (ATLAS) [79]. The process doubles the center-of-mass energy relative to the beam energy, enabling the potential production of heavy BSM particles. The LHC's unparalleled energy and luminosity have enabled the ATLAS and CMS experiments to conduct extensive searches for WIMPs and dark photons, resulting in numerous publications on dark matter production in the Higgs boson decay channel [78, 79]. These experiments are distinctive in their ability to explore previously inaccessible energy ranges and to explore rare particle interactions with high precision. In particle physics, the dark sector refers to a hypothetical set of undiscovered quantum fields and their associated theoretical particles, which may interact with known matter in a minimal way. Although identifying new particles does not directly confirm their roles as dark matter, the findings of LHC offer essential insights into potential dark sectors and show a path forward for the broader scientific community in the ongoing search for dark matter.

For a smaller target mass ranging from MeV to a few GeV, electron beam-dump experiments can be employed to search for dark matter. These beam-dump experiments deploy high-energy beams directed at target materials to probe for dark sector particles that can penetrate shielding to be detected, thus offering valuable data despite the particles' small interaction cross-section. Results from Izaguirre [80] demonstrate that a meter-scale detector positioned downstream of an electron beam-dump can effectively probe dark matter interactions via sub-GeV mediators. They further indicate that B-factory searches encompass the 1–5 GeV range. Together, these experiments dive into a highly motivated yet previously unreachable region of dark matter parameter space, with the potential to significantly improve sensitivity and surpass existing direct detection constraints by several orders of magnitude. [80]

2.1.2. Indirect detection

Indirect detection aims to identify the by-products of dark matter self-annihilation or decay, which are typically anticipated to include high-energy gamma rays, neutrinos, or pairs of Standard Model particles and antiparticles. Since the annihilation rate of dark matter is proportional to the square of its density, as both a particle and its antiparticle are required for annihilation, indirect detection experiments focus on regions with increased dark matter concentrations, such as galactic centers or the Sun.

Various instruments have been used to detect dark matter annihilation products, such as H.E.S.S. [81], VERITAS [82], and MAGIC (Cherenkov telescopes) [83], Fermi Large Area Telescope (LAT) [84], High Altitude Water Cherenkov Experiment (HAWC) [85], along with neutrino observatories like ANTARES [86], IceCube [87], and SuperKamiokande (Super-K) [88]. These instruments are dedicated to investigate potential signals from WIMPs across various cosmic structures, from the Galactic center and halo to galaxy clusters and dwarf galaxies, with each instrument tailored to its specific energy capabilities [89]. While a definitive dark matter annihilation signal remains elusive, these efforts have succeeded in establishing limits on the properties of dark matter, including constraints on the annihilation cross-section of WIMPs, the longevity of dark matter particles, and the rates of annihilation. Figure 2.2 shows the upper limits and projected sensitivity of the Cherenkov Telescope Array (CTA) on the pair-annihilation rate $\langle \sigma v \rangle$ versus the dark matter mass m_χ from gamma-ray and CMB observations. Various experiments, including H.E.S.S., utilize different models for the Galactic Center, such as the generalized Navarro-Frenk-White (gNFW) and Navarro-Frenk-White (NFW) profiles. These models help describe how dark matter is distributed within galaxies and clusters as distinct theoretical frameworks to interpret observational data.

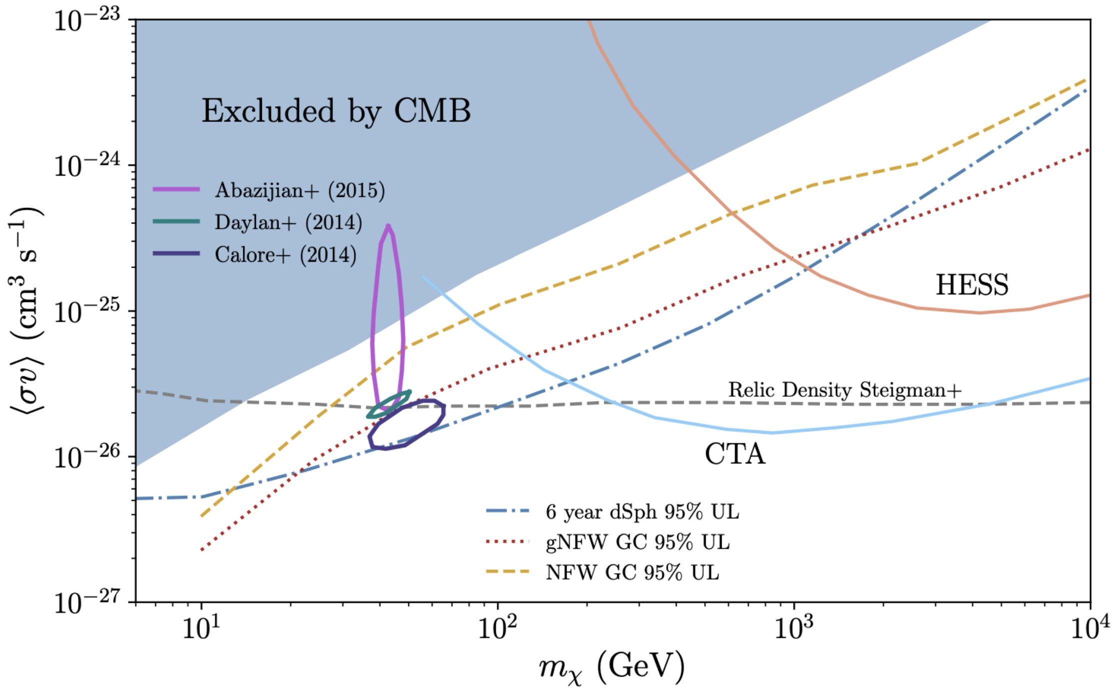

Figure 2.2: Upper limits and projected sensitivity from CTA on the pair-annihilation rate versus the dark matter mass from gamma-ray and CMB observations. The shaded regions were excluded by CMB constraints. The solid and dashed lines represent various upper limits derived from observations from different experiments and projected sensitivity using different theoretical frameworks. Image taken from [69].

2.1.3. Direct detection

In direct detection, experiments aim to identify signals from dark matter particles with a target nucleus, resulting in a nuclear recoil that can be observed. In scenarios of inelastic scattering, the experiments also search for signals that occur simultaneously with the nucleus's de-excitation. The expected scattering rate is given by:

$$\frac{dR}{dE_{nr}} = \frac{\rho_0 M}{m_N m_\chi} \int_{v_{min}}^{\infty} v f(v) \frac{d\sigma}{dE_{nr}} dv \propto \exp\left(-\frac{E_{nr}}{E_0}\frac{4m_\chi m_N}{(m_\chi + m_N)^2}\right) F^2(E_{nr}) \tag{2.1}$$

where m_N, m_χ, and M are the masses of the target nucleus, the WIMP particles, and the detector, respectively, E_{nr} is the nuclear recoil energy, σ is the scattering cross section, and $F(E_{nr})$ is the form factor. The WIMP-nucleus scattering cross section can be expressed as

$$\frac{d\sigma(E_{nr})}{dE_{nr}} = \frac{m_N}{2v^2\mu^2}\left[\sigma_{SI}F_{SI}^2(E_{nr}) + \sigma_{SD}F_{SD}^2(E_{nr})\right], \tag{2.2}$$

where the interaction is characterized by two components: a spin-independent (SI) and a spin-dependent (SD) component. The SI component corresponds to a scalar or vector effective four-fermion Lagrangian, and the SD term is configured as an axial-vector. At lower momentum transfer q, the nucleon partial waves sum coherently, permitting the WIMP to engage coherently with the nucleus entirely. At higher q values, the finite form factors F_{SI} and F_{SD} will account for the absence of coherence. The F_{SI} term is particularly pertinent for WIMP targets with substantial atomic mass numbers approximately $A \geq 100$ and at higher nuclear recoil energies E_{nr}.

In Equation 2.1, the dark matter halo is described by the normalized WIMP velocity distribution $f(v)$ and the local dark matter density ρ_0. E_0 is the WIMP's most likely detected kinetic energy and all velocities are in the detector's reference frame. To induce nuclear recoil of energy E_{nr}, it requires the minimal WIMP velocity $v_{\min}$

$$v_{\min} = \sqrt{\frac{E_{\mathrm{nr}} m_N (m_N + m_\chi)^2}{2(m_N m_\chi)^2}} = \sqrt{\frac{E_{\mathrm{nr}} m_N}{2\mu^2}}. \tag{2.3}$$

WIMPs that travel faster than the Galactic escape velocity $v_{\mathrm{esc}} = 544$ km/s [90] are no longer gravitationally bound to the Milky Way, resulting in their velocity distribution $f(v) = 0$ for $v > v_{\mathrm{esc}}$ when observed from the galactic rest frame. Here μ denotes the reduced mass of the nucleon-WIMP system. The observed differential rate will be a smooth exponential decline (refer to the latter part of Eq. 2.1), which emphasizes the significance of the detector's lower energy threshold E_{low} compared to the higher limit E_{high} during the detection process.

Integrating from Eq. 2.1 with the energy boundaries yields the expected event number in an experiment, given by

$$N = T \int_{E_{\mathrm{low}}}^{E_{\mathrm{high}}} dE_{\mathrm{nr}} \epsilon(E_{\mathrm{nr}}) \frac{dR}{dE_{\mathrm{nr}}}. \tag{2.4}$$

where T is the operation time of the detectors and $\epsilon(E_{\mathrm{nr}})$ is the detection efficiency. The maximum recoil energy $E_{\mathrm{high}} = 2\mu^2 v_{\mathrm{esc}}^2 m_N^{-1}$ is given by its kinematics. Typically, the recoil energies depending on m_N are small and on the order of $\mathcal{O}(10\,\mathrm{keV_{nr}})$. The nuclear recoil energy measurement $\mathrm{keV_{nr}}$ can differ from the electron recoil scale, expressed in $\mathrm{keV_{ee}}$, due to quenching effects caused by the different energy-loss mechanisms.

The search for dark matter particles, particularly those with masses in the $\mathrm{MeV/c^2}$ range, may not always produce a noticeable nuclear recoil due to the minimal momentum transfer to the nucleus. Therefore, experiments also focus on the scattering of WIMPs off electrons, which typically yields a signature that would be considered background noise in other contexts. The interaction strength between WIMPs and electrons is described using cross-section σ_e, and a dark matter form factor $F_{DM}(q)$, which typically varies with the momentum transfer q.

This approach for detecting WIMPs is mirrored in the search for very light axions and axion-like particles (ALPs), which may produce electronic recoils through a mechanism similar to the photoelectric effect, known as the axio-electric effect [45]. In this process, the absorption of an axion by an atom causes ionization, which is then detectable as an electron recoil (ER) signal. The energy of the recoiling electrons combines the rest mass and kinetic energy of the axion, minus the electron's binding energy. These phenomena are explored in greater depth in the context of effective field theories and other theoretical frameworks. [91] [92]

2.2. Axions and ALPs Detection

Axions are expected to be abundantly produced within the Sun's core. One production mechanism is Primakoff solar axions, a prediction based on many axion theories, requiring a non-zero axion-photon interaction constant $g_{a\gamma}$ that established principles of solar physics. Axions coupled to electrons in non-hadronic model provides additional production channels with the axion-electron interaction constant g_{ae} [71]. Upon their creation, axions depart from the Sun and travel to the earth, providing a great opportunity for their direct detection through ground-based experiments. The axion-electron coupling was explored in details through multiple helioscope experiments, which ultimately converged into a single collaborative effort, the International Axion Observatory (IAXO), aimed at detecting axions through such mechanisms [93]. On the other hand, the axion-electron coupling is particularly relevant for the search with dark matter experiments utilizing direct detection. Work with this approach will be described in later chapters, which facilitates a distinct detection approach compared to helioscope experiments.

2.2.1. Low energy axions detection

Axions are anticipated to be particles of very low mass, rendering their detection through traditional accelerator methods less likely [94]. For low energy axions with mass $m_a \lesssim 1$ eV, experimental approaches can be categorized into three different types, according to the source of axions expected: laboratory-based experiments, axion haloscopes, and axion helioscopes.

Laboratory-based experiments, such as light shining through walls (LSW) [95] setups, employ direct detection methods to identify axions generated within the laboratory or from external sources. LSW experiments involve directing a laser beam through a strong magnetic field to convert photons into axions, which pass through a barrier and are then reconverted into detectable photons using another magnetic field [95]. While these experiments are independent of astrophysical or cosmological assumptions, their effectiveness is limited by the low probability of photon-axion-photon conversion in a laboratory setting [96].

Haloscopes and helioscopes benefit significantly from the large axion flux expected from beyond earth's confines, making them capable of detecting axions at the sensitivity levels of QCD axion couplings. Detection from haloscopes is based on the assumption that axions constitute the entirety of dark matter.

If axions represented only a subset of dark matter, the sensitivity of haloscopes would need to be adjusted to reflect this lesser portion. For example, the Axion Dark Matter Experiment (ADMX) [97] exemplifies this approach, demonstrating the specific calibration needed for varying axion contributions to dark matter density. ADMX's haloscope investigated axion dark matter within the mass range of $3.3 - 4.2$ μeV. The result excluded the axion-photon coupling predicted by the Kim-Shifman-Vainshtein-Zakharov (KSVZ) model, a principal theory of "invisible" axion dark matter, for this specific mass range. However, it is important to note that this finding does not completely rule out KSVZ axions as a potential explanation for dark matter composition, as they may still exist at different mass ranges not covered by the ADMX experiment [98].

On the other hand, helioscopes depend on the phenomenon of the Sun producing axions with the Primakoff effect, where solar plasma photons are converted into axions, serving as their most conservative detection channel. This process is supported across a wide range of theoretical models with the existence of the $g_{a\gamma}$ coupling. The CERN Axion Solar Telescope (CAST) experiment has pioneered efforts in this domain, utilizing the Primakoff effect to search for solar axions, thereby testing the theoretical predictions and constraints on the axion-photon coupling strength with high precision. The result shown in Figure 2.3 established an upper limit on the axion-photon coupling at $g_{a\gamma} < 0.66 \times 10^{-10}\,\mathrm{GeV}^{-1} \quad (95\%\ \mathrm{C.L.})$, applicable to axion masses $m_a \lesssim 0.02$ eV. [99]

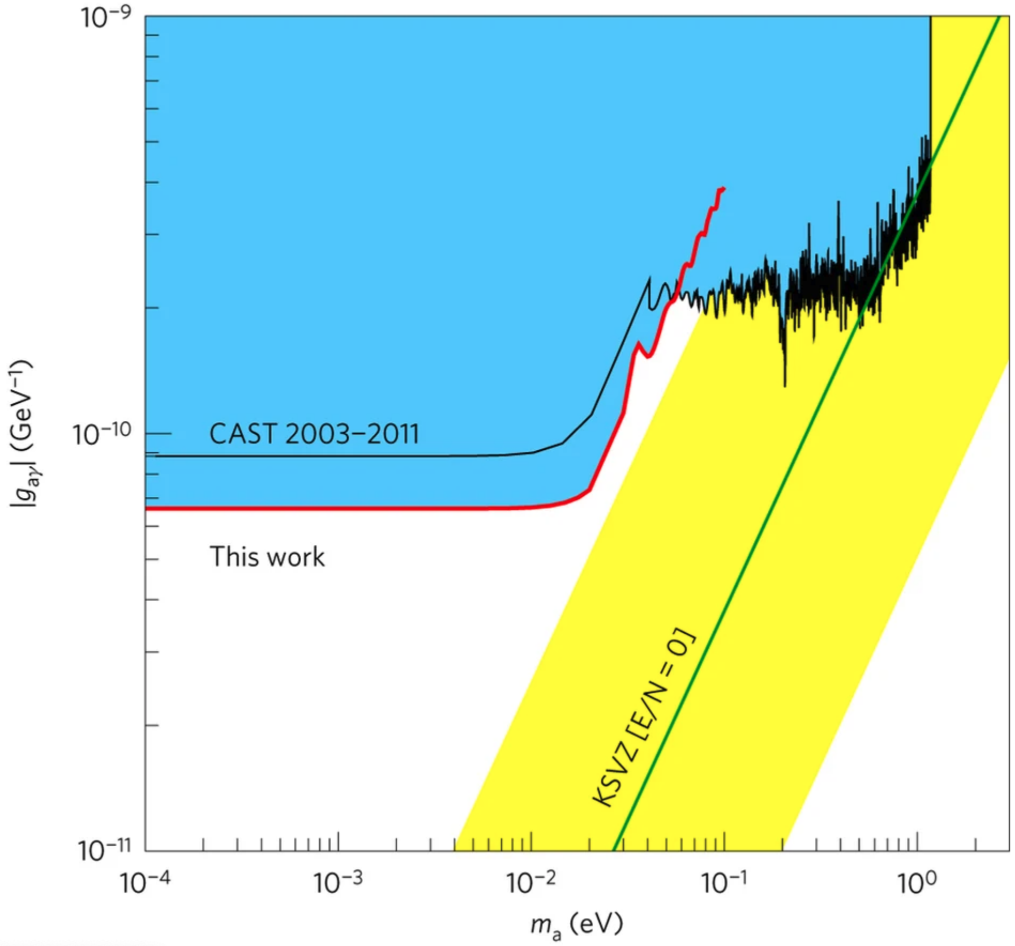

Figure 2.3: The excluded region at 95% confidence level (CL) in the parameter space of axion mass m_a and axion-photon coupling constant $g_{a\gamma}$, as determined by the CAST experiment [99]. Image taken from [99].

Beyond the low-energy range, more generic ALPs have the potential to circumvent the existing constraints on the axion mass, making models with relatively heavier ALPs feasible in the scope of exploration through accelerator-based experiments [100]. For instance, Brdar et al. [101] highlight the possibility of neutrino experiments, like DUNE, to detect signals of ALPs in the future, demonstrating that accelerators could play a pivotal role in the search for these particles across a broader mass range up to few GeV [101].

2.2.2. Low-Background experiments

Experiments aimed at detecting infrequent events such as WIMP interactions with nuclei are designed to minimize background interference and obtain low energy thresholds. The data collected on background noise from these detectors can also be used for detecting signals of axion-like particles (ALPs) or hidden photons, serving as an advantageous secondary outcome of these primary searches. Various detection methods are employed to identify ALPs or hidden photons originating from diverse sources.

The characteristic signal of the axio-electric effect is observed as an energy deposition in the detector, representing the sum of the axion's rest mass and the incoming ALP's kinetic energy, minus the binding energy of the electron [102].

The axio-electric effect [45] can be applied when searching for solar axions with low background detectors, usually for axion masses in keV scale. Detectors need to obtain a sufficiently low threshold to observe the keV electron that absorbed the thermally produced axions. Limits can then be obtained for different couplings corresponding to the different axion production mechanisms within the Sun. Limits on solar axions have been published as by-products of WIMP searches like XENON100 [103], PandaX [104], LUX [105], XENON1T [106] and CDEX [107]. The work in this dissertation builds upon these previous efforts, utilizing the unique capabilities of the SuperCDMS detectors to probe the axion-electron coupling with its own sensitivity. By pushing the detection threshold to even lower energies and leveraging the detector's excellent background rejection capabilities, this analysis aims to set new limits on the axion-electron coupling, furthering our understanding of the axion's role in solar physics and potentially shedding light on the nature of dark matter.

Solar axions and ALPs can also be detected through their coherent Bragg conversion into photons within the electric fields of crystalline detectors. This conversion process depends on the orientation of the crystals relative to the Sun, resulting in distinctive time-dependent modulations that can be analyzed for detection. Experiments such as DAMA [108], CDMS [109], and EDELWEISS [76] have scrutinized their data for these modulations, setting constraints on $g_{\mathrm{ALP}\gamma} < 2 \times 10^{-9}\,\mathrm{GeV}^{-1}$.

Chapter 3

SuperCDMS Experiments

The Super Cryogenic Dark Matter Search (SuperCDMS) experiments deployed direct detection methods with cryogenic semiconductor detectors instrumented with superconducting transition edge sensors (TES) to search for dark matter particle interactions. The first phase of the SuperCDMS experiment was conducted at the Soudan Underground Laboratory (SUL) in northern Minnesota. The following phase of the experiment is currently undergoing extensive preparations and will be hosted at the prestigious SNOLAB facility in Sudbury, Ontario. Before the full operation of the SuperCDMS SNOLAB experiments, the detectors will be tested in the adjacent Cryogenic Underground TEst (CUTE) facility within SNOLAB in low background conditions.

3.1. Detector Principles

The SuperCDMS detectors are designed to detect both the phonon and ionization signals produced by the interaction of dark matter particles with the detector material. This dual-signal approach is a major feature that woubld enable the experiment to effectively distinguish between nuclear recoils (NR) and electron recoils (ER), differentiating dark matter signals from background noise such as neutrons, which produce NR events. The experiment primarily employed semiconductor technologies and other advance signal readout techniques, such as transition-edge sensors (TES) for phonon detection and charge amplifiers for ionization detection.

3.1.1. Semiconductor physics

Semiconductors, with their unique electronic properties, have been utilized in numerous applications across different fields, including use in particle detectors at cryogenic temperatures (usually less than 1K). In a semiconductor material, electrons can reside in two distinct energy regions – the valence band and the conduction band. Within the valence band, electrons are bound to the atoms of the crystal, orbiting the nuclei. However, electrons with sufficient energy can be promoted to the conduction band, and become free to move throughout the crystal structure. The energy required for this transition is referred to as the band gap energy, denoted as E_g.

Therefore, materials with larger band gaps exhibit lower electrical conductivity. The probability of an electron occupying an energy state E in a semiconductor follows the Fermi-Dirac distribution $f(E)$, which is given by:

$$f(E) = \frac{1}{e^{(E-E_F)/k_BT} + 1} \tag{3.1}$$

where k_B is the Boltzmann constant, T is the temperature dependence of the system, and E_F is the Fermi level, which corresponds to the energy state that has a 50% probability of being occupied by an electron when the system reaches a thermal equilibrium. For intrinsic or undoped semiconductors, E_F lies halfway between the valence band and conduction band. At absolute zero temperature (T = 0 K), the exponential term in the denominator approaches infinity for energy states above the Fermi level ($E > E_F$), and it approaches zero for states below the Fermi level ($E < E_F$). Consequently, the distribution function becomes a step function, where all states below the Fermi level are completely filled with electrons ($f(E) = 1$), while all states above the Fermi level are entirely empty ($f(E) = 0$). However, at high temperatures, some electrons can occupy energy states above E_F and may reside in the conduction band illustrated in Figure 3.1.

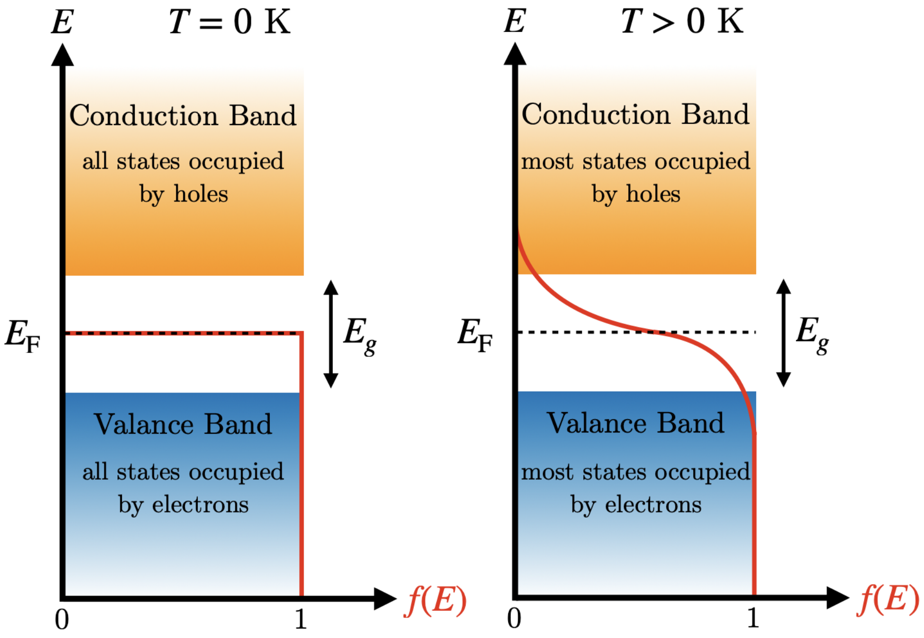

Figure 3.1: Illustration of how electrons and holes occupy energy states according to the Fermi-Dirac distribution in a semiconductor. Image taken from [110].

When detectors with semiconductor are cooled to cryogenic temperatures, the majority of electrons will settle into the the energy states within the valence band, leaving the conduction band nearly empty. As a result, electrons can only transition to the conduction band if they receive an external energy input that exceeds the band gap energy, making it possible for them to overcome the energy barrier between the two bands. The absence of an electron in the valence band would create a positively charged quasiparticle called a hole. Although not considered as physical particles, holes occupy energy states, with each conduction band electron corresponding to a valence band hole. Every electron promoted to the conduction band is mirrored by a hole left in the valence band, forming electron-hole pairs $e^- h^+$.

When particles interact with a solid-state detector, they can transfer energy to the atoms within the cryogenically cooled semiconductor crystal. This energy transfer can occur through two distinct energy depositions – either by directly granting the energy to an atomic nucleus, causing it to recoil as a NR event, or to an electron in the valence band as an ER event. In both cases, the result is the creation of electron-hole pairs e^-h^+ within the semiconductor material. The number of electron-hole pairs generated depend on the interaction type, whether it is an ER or a NR. For the same amount of deposited energy, NR events create a smaller number of ionization pairs compared to ER events.

For a standard electron recoil or nuclear recoil event, the ionization yield $Y(E_R)$ is given by the ratio of the interaction energy E_Q to the recoil energy:

$$Y(E_R) = \frac{E_Q}{E_R} \tag{3.2}$$

The ionization yield quantifies the efficiency of generating charge carriers, differentiating events between electron recoils and nuclear recoils. By definition, ER events have an ionization yield of 1, while NR events exhibit a lower ionization yield. The average number of electron-hole pairs $\langle N \rangle$ produced in an interaction is given by:

$$\langle N \rangle = \frac{E_R}{\epsilon_\gamma} \tag{3.3}$$

where E_R is the recoil energy and ϵ_γ is the mean energy required to generate a single electron-hole pair, which is 3.0 eV for germanium, and 3.8 eV for silicon. The minimum energy required to produce an electron-hole pair is given by the band gap energy E_g, which is 1.12 eV for germanium and 0.66 eV for silicon at cryogenic temperatures. [111]

3.1.2. Phonon signals

While the drifting electron-hole pairs can be directly detected, the primary method for measuring energy in the semiconductor detectors is to capture the heat energy associated with lattice vibrations in the crystal, known as phonons. Phonons measured in the detector can be two distinct types: prompt phonons and Neganov-Trofimov-Luke (NTL) phonons.

Prompt phonons are generated from the lattice vibrations that arise immediately after a particle interacts with an atomic nucleus or electron within the detector, which would transfer a portion of its energy to the lattice. NTL phonons are emitted as a result of this effect, which occurs when charged particles are accelerated by the electric field within the detector. These phonons propagate through the detector and are subsequently absorbed by the phonon sensors on the detectors' surface.

On the other hand, athermal phonons include both prompt and NTL phonons, which are different from the thermal phonons due to the temperature of the semiconductor detector material. When the semiconductor is cooled to cryogenic temperatures, athermal and thermal phonons have distinctly different energy ranges. At an operating temperature of 10 mK, thermal phonons typically have energies around 1 μeV [112], while athermal phonons generated in Si or Ge semiconductors possess energies of at least 0.4 meV [113]. Unlike the low-energy thermal phonons, athermal phonons carry sufficient energy to be captured by sensors distributed on the detector's surface, where they generate a measurable signal.

The detection of phonons is made possible by transition edge sensors positioned on the detector's surface. These sensors exploit the temperature-dependent transition between superconducting and normal states, characterized by the critical temperature T_c, as depicted in Figure 3.2. To detect heat depositions, the TES is maintained at a temperature close to T_c. When a heat deposition occurs, the TES temperature and resistance increase, causing a change in the current flowing through the sensor. R_n is the normal-mode resistance of the TES and ΔT_c is the transition width.This current change is subsequently recorded as the measurement signal.

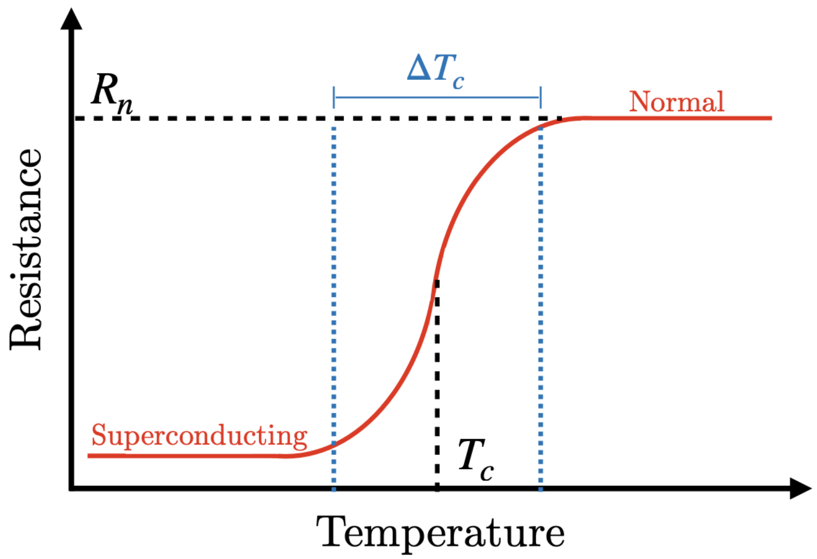

Figure 3.2: Illustration of a resistance-temperature curve for a transition edge sensor. Image taken from [110].

3.1.3. Charge signals

The charge signals are measured by electrodes placed on the surface of detectors. The electrodes are designed to collect the charge carriers, including both electrons and holes, generated by interactions within the detector material. When a bias voltage is applied across the detector, it creates an internal electric field within the detector. Under the influence of this electric field, electrons and holes would drift to the opposite sides, inducing a detectable current or voltage signal given by the Shockley-Ramo theorem [114, 115]:

$$\vec{I} = q\vec{E} \cdot \vec{v} \tag{3.4}$$

This process can be amplified and processed by the detector's charge readout circuitry. Since the strength of the charge signal is proportional to the quantity of electron-hole pairs created during the initial interaction, the readout, in turn, depends on the amount of energy deposited by the incident particle. Figure 3.3 presents a simplified diagram of the electronic circuit employed for measuring and extracting such charge signal generated within the detector.

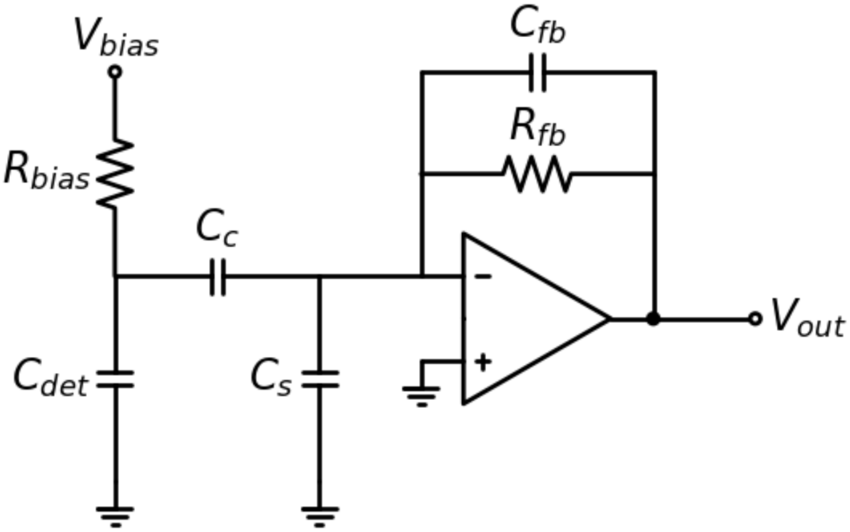

Figure 3.3: A simplified diagram of the circuit from [116]. This circuit was employed for measuring the charge signal generated within the detector.

In Figure 3.3, V_{bias} is the bias voltage input through the bias resistor R_{bias}, and V_{out} is the output voltage through an amplifier. The moving charges induce corresponding mirror charges on the electrodes, which is then coupled to a high-sensitivity charge amplifier through a coupling capacitor C_c. The charge amplifier incorporates a feedback capacitor C_{fb} to stabilize the operation. The presence of stray capacitance in the circuit is accounted for by the term C_s. V_{out} is the output voltage through an amplifier given by:

$$V_{out} = \frac{Q_{ind}}{C_{det}} \tag{3.5}$$

where Q_{ind} is the induced charge, and C_{det} is the detector's inherent capacitance. Following amplification, the signal gradually decays as the capacitor discharges, with a characteristic fall time described by:

$$\tau_Q = \frac{R_{fb}}{C_{fb}} \tag{3.6}$$

Different mechanisms of charge carrier can influence the accuracy of the measurement, resulting in either a shortage or surplus of detected charge. To accurately describe the detector's behavior, the response model must take into account two significant phenomena: charge trapping (CT) and impact ionization (II), demonstrated in Figure. 3.4

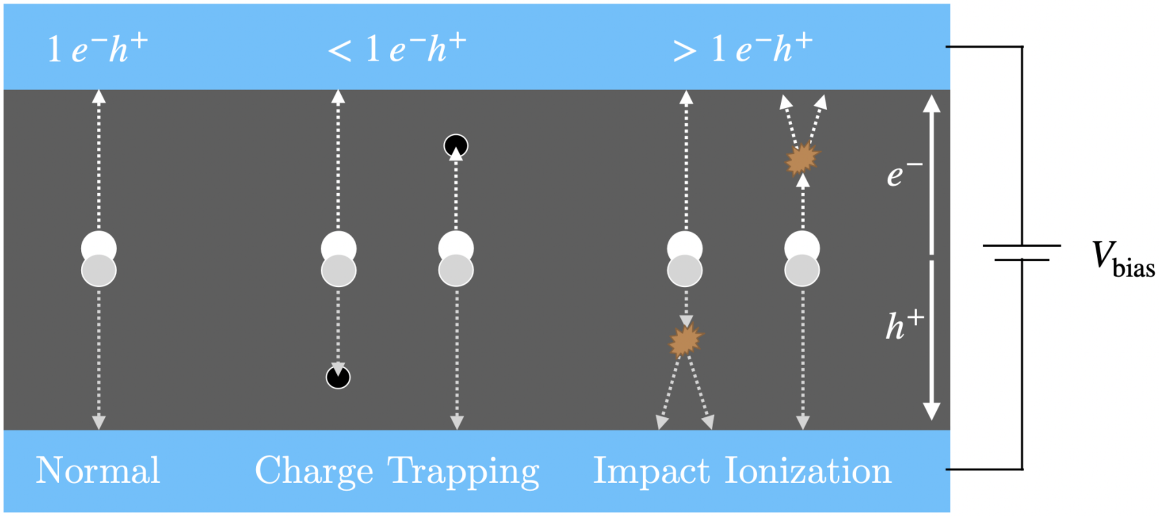

Figure 3.4: Demonstration of two significant phenomena that would impact the accuracy of charge measurement: charge trapping and impact ionization. Image taken from [110].

Charge trapping occurs when propagating charge falls into charge vacancy in the crystal lattice, preventing them from reaching the electrodes and contributing to a shortage of measured signal. On the other hand, impact ionization takes place when charge carriers with sufficient kinetic energy free additional loosely-bound charges along their path, leading to a surplus of the original charge signal. Defects or impurities of the crystal lattice could cause charge trapping or impact ionization effects, which shape the distribution of events observed between the quantized peaks corresponding to discrete numbers of electron-hole pairs.

3.2. SuperCDMS Soudan

The SuperCDMS Soudan experiments operated from 2011 to 2015 in the Soudan Underground Laboratory, located 2341 feet below the surface in northern Minnesota. The experiments used interleaved Z-sensitive Ionization and Phonon-mediated (iZIP) detectors. The experimental apparatus, originally constructed for the Cryogenic Dark Matter Search (CDMS II) experiment [117], features a low-background cryostat enclosed within a passive shielding structure and an outer muon veto system. The underground location affords an overburden equivalent to 2090 meters of water, which provides substantial shielding from cosmic radiation. [109]

3.2.1. Detectors

The SuperCDMS Soudan experiments arranged five vertically stacked arrays of 15 high-purity germanium detectors in total, with three detectors comprising each individual tower in the stacked configuration illustrated in Figure 3.5. Each detector is in cylindrical shape with 76 mm diameter and 25 mm thickness, weighting about 600 grams. [118]

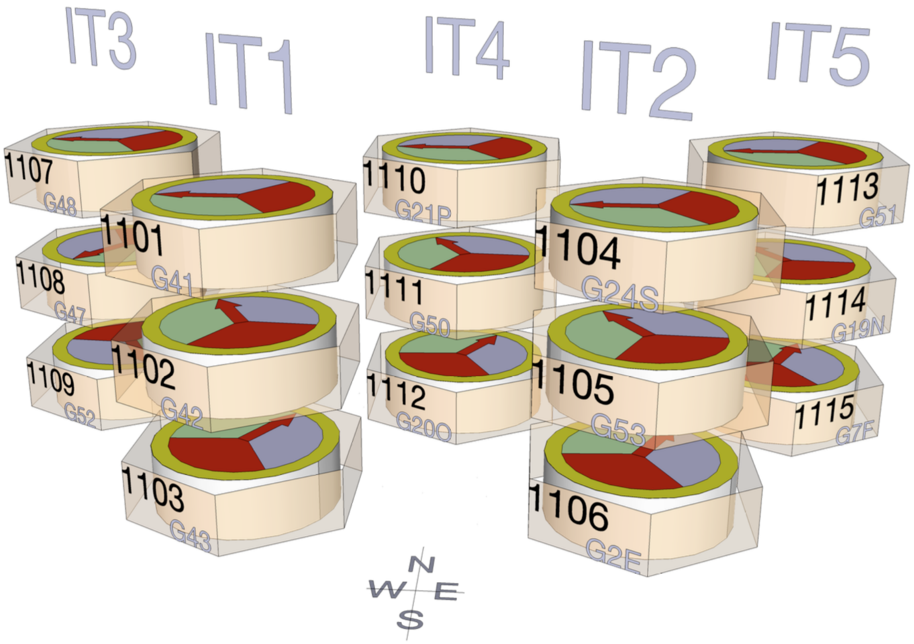

Figure 3.5: Layout of the five towers in SuperCDMS Soudan Experiment with labels on tower numbers and detector numbers. Detector and tower numbers are unique for identification. Image taken from [119].

As mentioned above, when a particle like a nucleus or electron interacted and scattered within the crystal substrate, it produced pairs of free electrons and holes as well as vibrations in the crystal lattice known as phonons. A bias voltage was applied to collect these ionization signals, which were applied parallel to the cylinder's axis throughout the bulk crystal volume and perpendicular to the axis near the flat end faces. This electric field caused the free electrons and holes to drift towards the electrode sensors, with the electrons collected on an inner disk-like electrode and the holes on an outer ring-shaped annular electrode, both patterned on each of the two end faces. Separately, the detectors also incorporated four distinct phonon sensors positioned on each of the end faces as illustrated in Figure 3.6, measuring the vibration signals produced by particle interactions in the crystal [118]. Therefore, the detectors are capable of simultaneously measuring ionization and phonon signals generated by particle interactions within the detector volume [117].

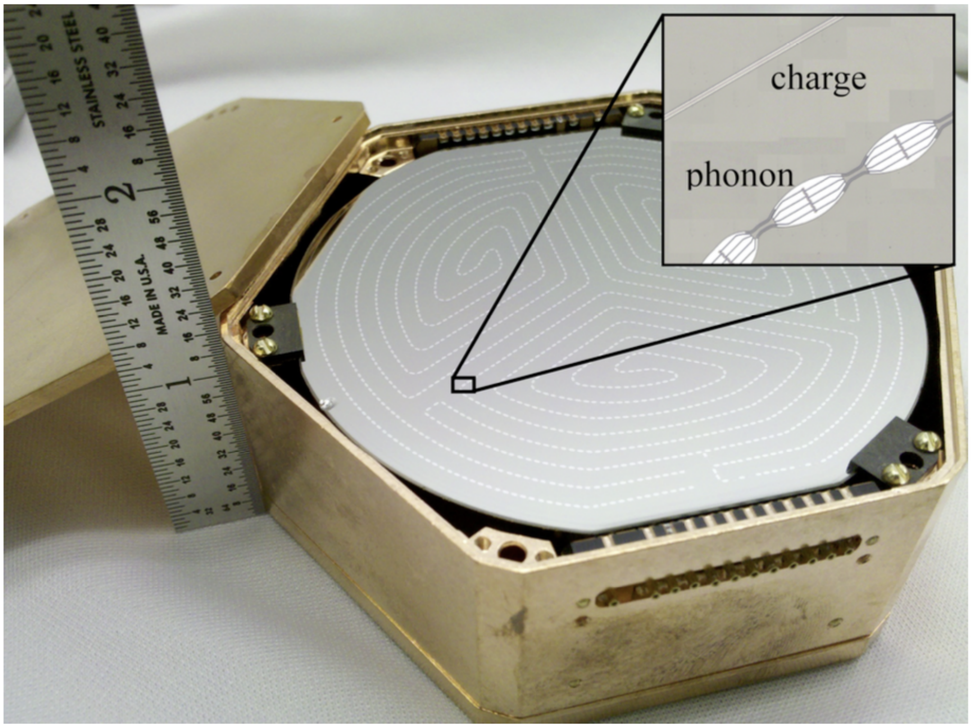

Figure 3.6: An iZIP detector in its housing; image taken from [120]. The phonon channels are visible and interleaved with the charge channels, forming a meandering pattern.

The detector sensors were segmented into multiple distinct readout channels to achieve precise characterization of particle interaction signals. On each of the two flat end faces, the ionization sensors were divided into two channels—an inner circular electrode at the center, and an outer annular ring-shaped electrode surrounding it. Complementing the charge sensors were four phonon channels also patterned on each face. One of these phonon channels covered the same outer region as the outer ionization ring electrode. The remaining three phonon channels were sliced into wedge-like sections, collectively spanning the inner area corresponding to the central circular ionization electrode. The channel layouts on the two opposing detector faces were oriented with a 60-degree relative rotational offset illustrated in Figure 3.7.

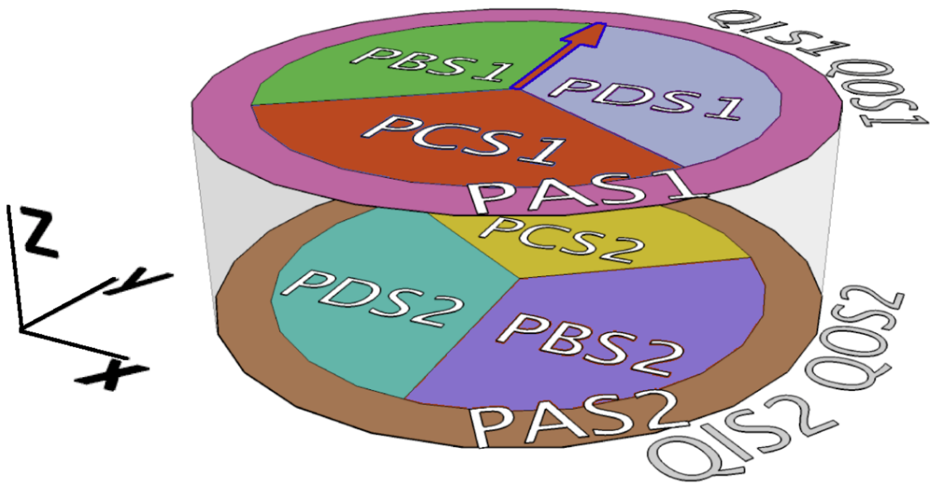

Figure 3.7: Layout of channels on each face of the iZIP detectors. The phonon sensors were segmented into four quadrant regions labeled A-D, with each side's quadrants identified by a number. For instance, PAS1 stands for phonon sensor A on Side 1. The outer ionization channel occupies the same area as the outer phonon quadrant, while the inner circular ionization electrode region corresponds to the three inner wedge-shaped phonon quadrants. Image taken from [121].

The detectors employed a bias voltage across itself to enable effective discrimination of surface interaction events, demonstrated in Figure 3.8. A symmetric ± 2 V potential difference was applied, with the ionization electrode biased while the phonon sensors were grounded. The grounding of the phonon channels created an electric field configuration that caused charge carriers from surface events to preferentially drift towards and be collected on the grounded phonon quadrants rather than the biased ionization electrodes on the opposing face, illustrated in Figure 3.8. [120]

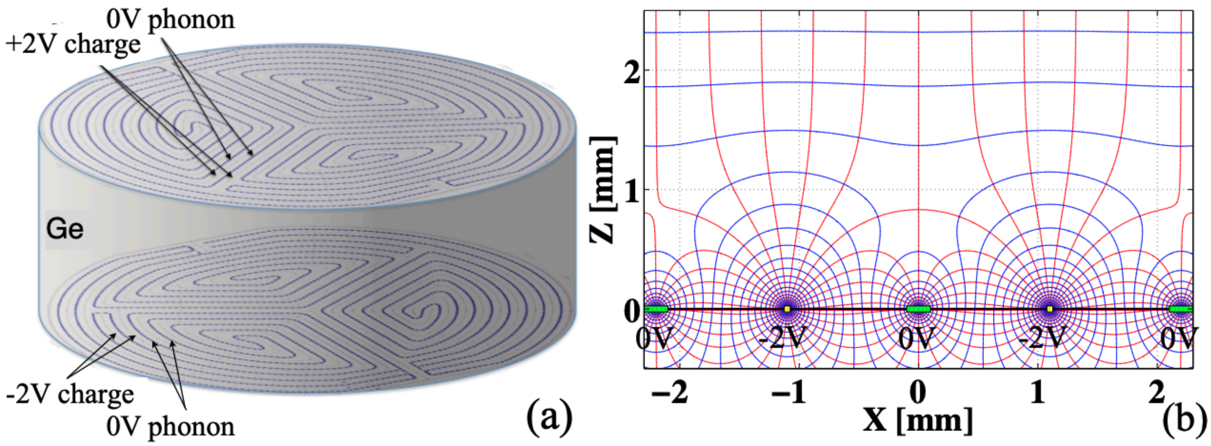

Figure 3.8: (a) Both faces of the detectors are instrumented with ionization lines with ± 2 V that are interleaved with phonon sensors (0 V) on a ∼1 mm pitch. (b) Magnified cross-section view of electric field lines (red) and equipotential contours (blue) near the bottom face of a SuperCDMS iZIP detector. The −2 V ionization electrode lines (yellow) are narrower than the 0 V athermal phonon collection sensors (green). Image taken from [120].

The field geometry caused an asymmetry in the ionization signals measured on each side for surface events, which offers a powerful tool for rejecting these backgrounds. This asymmetry profile effectively distinguishes surface events from bulk events [120]. The bias voltage is constrained to a range where the energy of NTL phonons is close to the recoil energy. This balanced voltage tuning allowed the detectors to leverage a complementary discrimination technique based on comparing the measured phonon signal amplitudes against the ionization signals on an event-by-event basis. Nuclear recoils and electron recoils could then be distinguished by calculating the differences in their respective ionization-to-phonon signal yield ratios from the intrinsic quenching factors for each interaction type. The low-energy reach and precision of this yield-based discrimination depended critically on the combined resolution of the phonon and ionization readout channels, with the ionization resolution typically being the dominant limiting factor.

3.2.2. Shielding

The SuperCDMS Soudan experiment deployed CDMS-II low-background apparatus. The experiment setup consisted of a cryostat at the core, enclosed by multiple layers of shielding materials. The outermost layer was a muon veto detector system designed to identify and reject events caused by cosmic muons. Underneath the muon veto was a passive shielding layer constructed with different high-density materials. The passive shield had an outer 40 cm polyethylene segment, followed by a 22.5 cm lead segment to block gamma radiation, and an inner 10 cm polyethylene section. The cryostat itself, housing the cryogenically cooled detectors, along with the internal hardware, provided an additional 3 cm of copper shielding. [122]

More importantly, the entire apparatus was located at a depth of 714 meters underground at the Soudan Mine, with an overburden of 2090 meters water equivalent to minimize cosmic ray interactions. The overburden reduced the surface muon flux by a factor of 5×10^4. The shielding setup aimed to minimize all potential background radiation sources to create a low-background environment for the rare dark matter interaction search. The cryostat was surrounded by shielding and connected to the dilution refrigerator with the C-stem, all contained in an RF tight room as depicted in Figure 3.9. The outermost layer of the RF room consist of an active muon veto detector system, which was designed to identify and flag any residual muon events that managed to penetrate through the main overburden shielding of the underground laboratory.

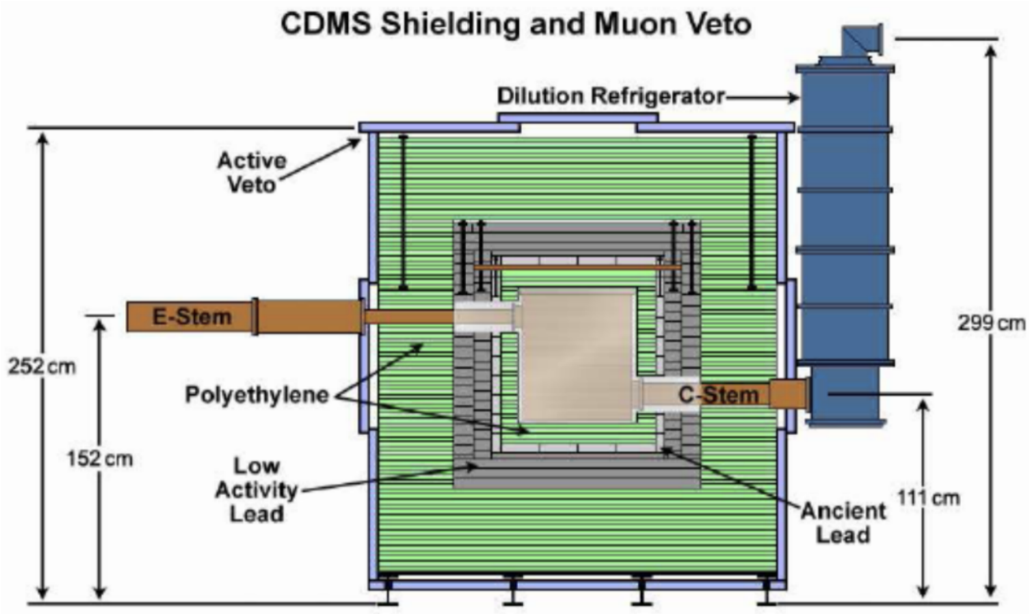

Figure 3.9: The layout of CDMS shielding and its muon veto. Within the shielding, the cryostat is surrounded by multiple passive shielding layers composed of polyethylene and lead. This is further enveloped by a muon veto system characterized by its active scintillator panels. To the right, the dilution refrigerator is linked to the cryostat via the C-stem, while wiring exits the cryostat through the E-stem. Image taken from [123].

3.3. SuperCDMS SNOLAB

The next phase of the SuperCDMS experiment is set to take place at SNOLAB, located in Sudbury, Ontario [118]. SNOLAB stands as a Canadian premier underground research facility, positioned 2 km beneath the surface, and recognized as the world's deepest and cleanest laboratory [124]. The SuperCDMS SNOLAB experiment will benefit from lower background interference due to enhanced shielding and material screening, alongside detectors with increased sensitivity. The experiments will use both high-voltage and iZIP detectors, composed of either silicion or germanium as the target material.

3.3.1. Detectors

The SuperCDMS SNOLAB experiment will employ detectors of cylindrical shape, consisting of both germanium and silicon crystals. These detectors have a thickness of 33 millimeters and a diameter of 100 millimeters. The experiment will encompass four distinct detector types, categorized as iZIP and high-voltage (HV), with each category further divided into silicon and germanium components. The experimental setup consists of four towers, with each stacking six detectors. This configuration results in a combined array of 24 individual detectors in total. Two of these towers will exclusively consist of iZIP detectors, while the remaining two will be dedicated to HV detectors. Notably, one of the iZIP towers will be composed solely of germanium detectors, while the other towers will feature a combination of two silicon detectors and four germanium detectors.

The iZIP detectors feature 12 phonon channels, with six channels on each side, accompanied by two interleaved charge electrodes positioned on the inner and outer surfaces of each detector face, resulting in a total of four charge channels. In contrast, the HV detectors will lack charge electrodes but will incorporate 12 phonon channels arranged in a slightly different layout compared to the iZIP detectors. Both detector layouts are illustrated in Figure 3.10.

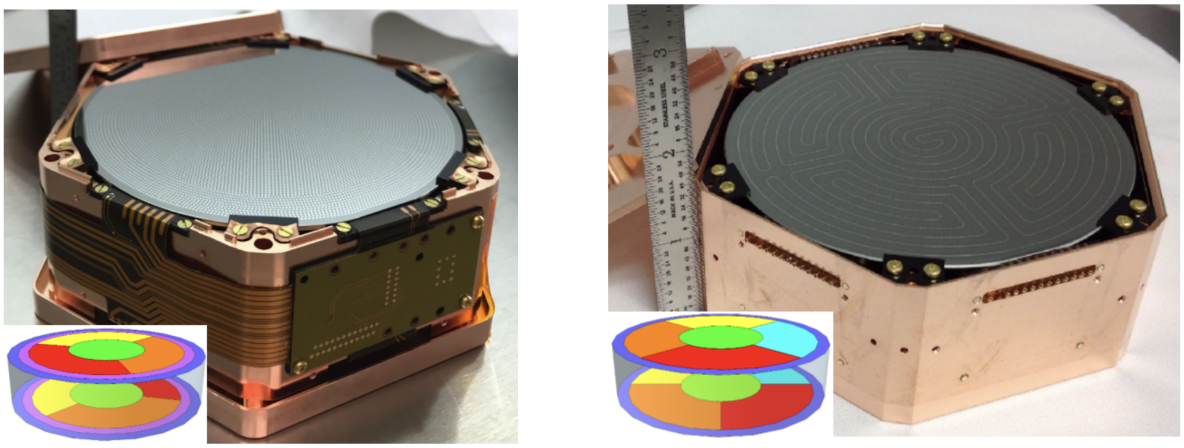

(a) SuperCDMS SNOLAB HV detector, with the layout of the phonon sensors shown in the bottom left.

(b) A SuperCDMS SNOLAB iZIP detector in a prototype copper housing, the layout of the phonon sensors is shown in the bottom left.

Figure 3.10: The HV and iZIP detectors of the SuperCDMS SNOLAB experiment. Layouts of the phonon sensors shown in the bottom left. Image taken from [121].

The channels of each detector will be connected through wirebonding to a horizontal flexible cable (HFC) that wraps around the detector housing. The HFC will then be linked to a vertical flexible cable (VFC) that supports the cold electronics and runs along the length of the tower. These flexible cables will incorporate superconducting traces backed by Kapton, with electronic components and connectors mounted on Cirlex stiffener boards. At the base of the VFC, a short superconducting cable will facilitate connectivity to a long readout cable at the 4 K stage, enabling the signals to be transmitted to room temperature. A vacuum interface board (VIB), hermetically connected to a vacuum port on the cryostat, will serve as the gateway for passing the signals outside the cryostat. This VIB will be connected to the room temperature readout electronics, known as the detector control and readout cards (DCRCs). Notably, the grounds of the DCRCs will float with respect to the chassis of the experiment, enabling the phonon channels of the HV detectors to be read out while biased – a capability that was not available with the SuperCDMS Soudan electronics. Although the electronics used by SuperCDMS SNOLAB differ from those employed in SuperCDMS Soudan, the general operating principle remains consistent.

3.3.2. Shielding

Located 2 km underground, SNOLAB benefits from a formidable 6010 water equivalent overburden, which has a factor of 3 improvement than Soudan. Figure 3.11 illustrates the relative overburden depths of various underground laboratories and their corresponding muon fluxes. Notably, the muon flux at SNOLAB is suppressed by over two orders of magnitude in comparison to Soudan, highlighting the exceptional shielding capabilities of this underground location. Furthermore, the entire laboratory operates as a class 2000 clean room and it is able to control dust contamination exceptionally well.

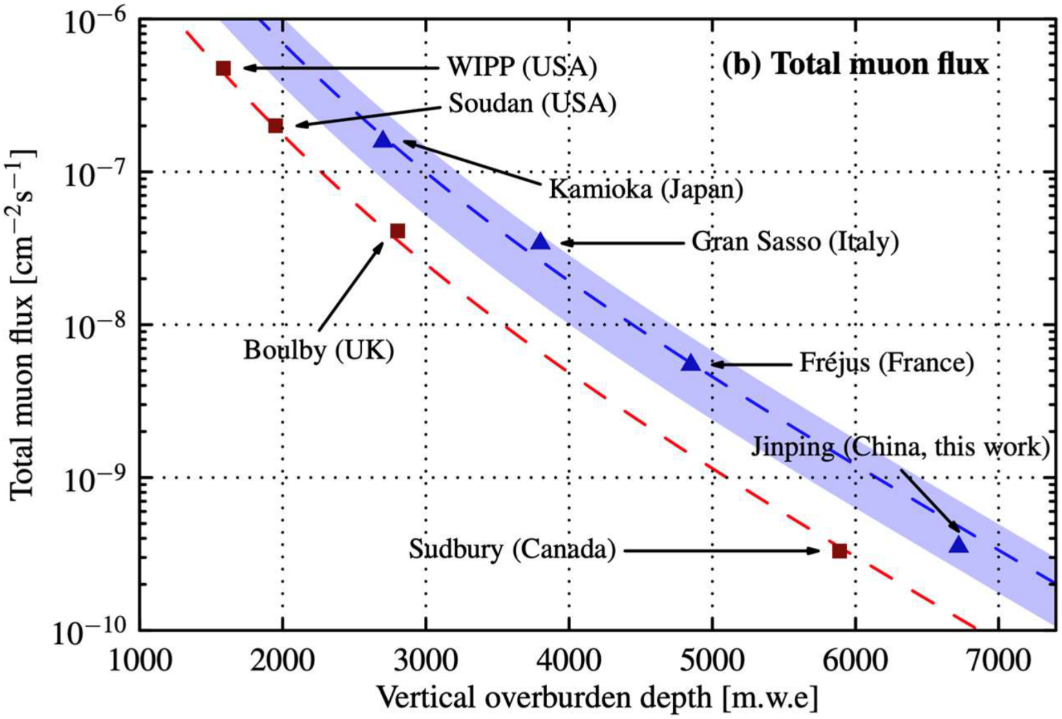

Figure 3.11: SNOLAB's depth and muon flux compared to other underground laboratories, including Soudan Underground Laboratory. Image taken from [125].

The SuperCDMS SNOLAB experiment will have a noval infrastructure with a new cryostat and shielding system, which is expected to reduce the background levels more than SuperCDMS Soudan. A schematic of the experiment is shwon in Figure 3.12. With an improved dilution refrigerator, the operational temperatures will be achieved with an expected range of 15 – 30 mK, which is lower than experiments at Soudan. The cold region housing the detectors within the experiment is referred as the SNOBOX. Within this area, six cylindrical copper cans will be suspended by robust Kevlar ropes, which is a similar configuration to the Soudan setup but larger dimensions for the SNOLAB cans.

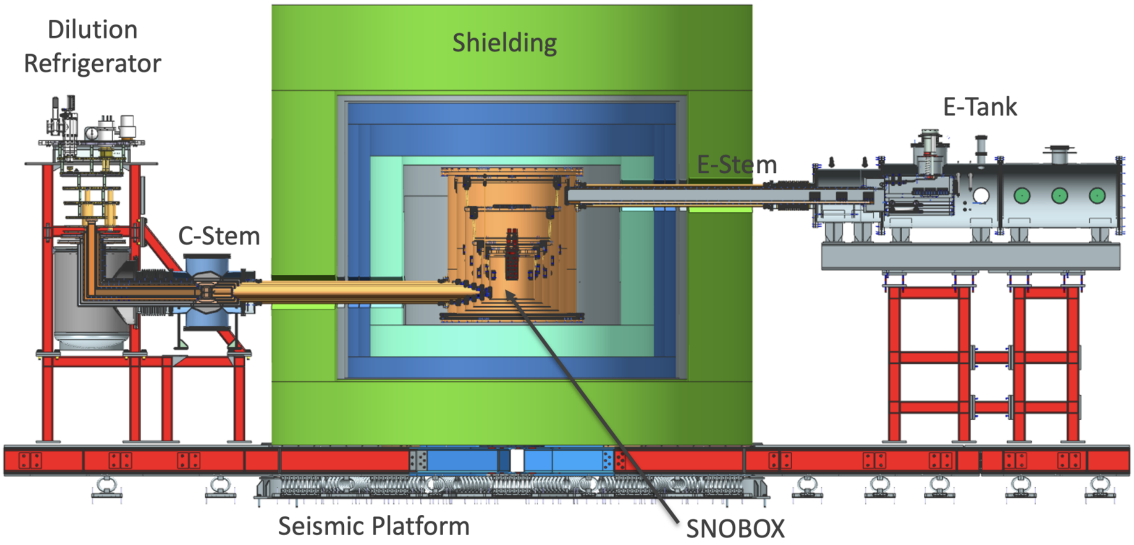

Figure 3.12: The schematic of the SuperCDMS SNOLAB experiment. The detector payload is housed in a cryostat called SNOBOX, surrounded by dense shielding to block background radiation. External connections are made through stem assemblies to reduce penetrations in the shielding. The setup is mounted on a platform to isolate it from the lab floor, ensuring protection during major seismic events. Image taken from [126].

The SNOBOX is mounted within layers of shielding for neutrons and gammas. Similar to the layout of Soudan experiment, the cryostat or SNOBOX is connected to the dilution refrigeator through the C-stem, transferring electrical signals to the E-Tank through E-Stem. The SNOBOX, dilution refrigerator, shielding, and room-temperature electronics are all mounted on a seismic isolation platform, providing a stable and isolated environment for the experiment. This is crucial to mitigate the impacts of seismic activity, such as rock bursts from mining operations or earthquakes.

The SNOBOX itself also comprises several layers of copper cans, with the innermost layer serving as the mounting point for the detector towers. The innermost layer is thermally linked to the dilution refrigerator for temperature control. Enclosing the SNOBOX is a multi-layered shielding system, with the only openings being the connections through the C-stem and the E-stem. The foundation of this shielding system is a 60 cm thick layer of high-density polyethylene (HDPE) plates, positioned at the bottom of the experiment to block neutrons. On top of these HDPE plates lies the rest of the shielding layers. The outermost layer consists of several 60 cm thick water tanks, which was designed to moderate the flux of neutrons. The area within these water tanks is continuously purged with low-radon air to maintain optimal conditions. Within the water tanks, there is a layer of 23 cm thick low-activity lead, which would provide nearly complete 4π coverage from gamma rays. Further enhancing the shielding capabilities, an additional 30 cm of HDPE is incorporated to further moderate the neutron flux.

3.4. The Cryogenic Underground Test Facility

The Cryogenic Underground TEst (CUTE) Facility, located at SNOLAB, was initially built to evaluate potential background interference for the new SuperCDMS dark matter detectors. The primary objective of CUTE is to provide an environment for testing cryogenic devices that might be exposed to radiation and vibrations, which is necessary for rare event search experiments like direct detection of dark matter particles. [127]

The CUTE facility, as illustrated in Figure 3.13, features a cylindrical water tank as its primary structure for shielding. It is approximately 3.6 m in both height and diameter. Inside the water tank's well-protected drywell, there is a cryostat containing the detectors positioned on an active suspension system. The drywell is firmly mounted to the stainless steel deck. This setup allows researchers to access the cryostat when it is in the drywell, making it possible for them to establish connections with the cryogenic systems and verify the detector's continuity.

The detectors are installed in the cryostat within the neighboring clean room, which receives low-radon air from either the SNOLAB compressed air system or the SuperCDMS radon filtration system. After the detectors are in place and the cryostat is sealed, an overhead mono-rail crane will transport the cryostat from the clean room to the drywell. The gas handling system (GHS), situated on the ground adjacent to the water tank, comprises pumps, pneumatic valves, and a helium tank, all of which are essential for operating the dilution refrigerator that cools the CUTE cryostat. Additionally, several computers are used to manage the dilution refrigerator and the detector's readout, which are located on the ground beside the water tank.

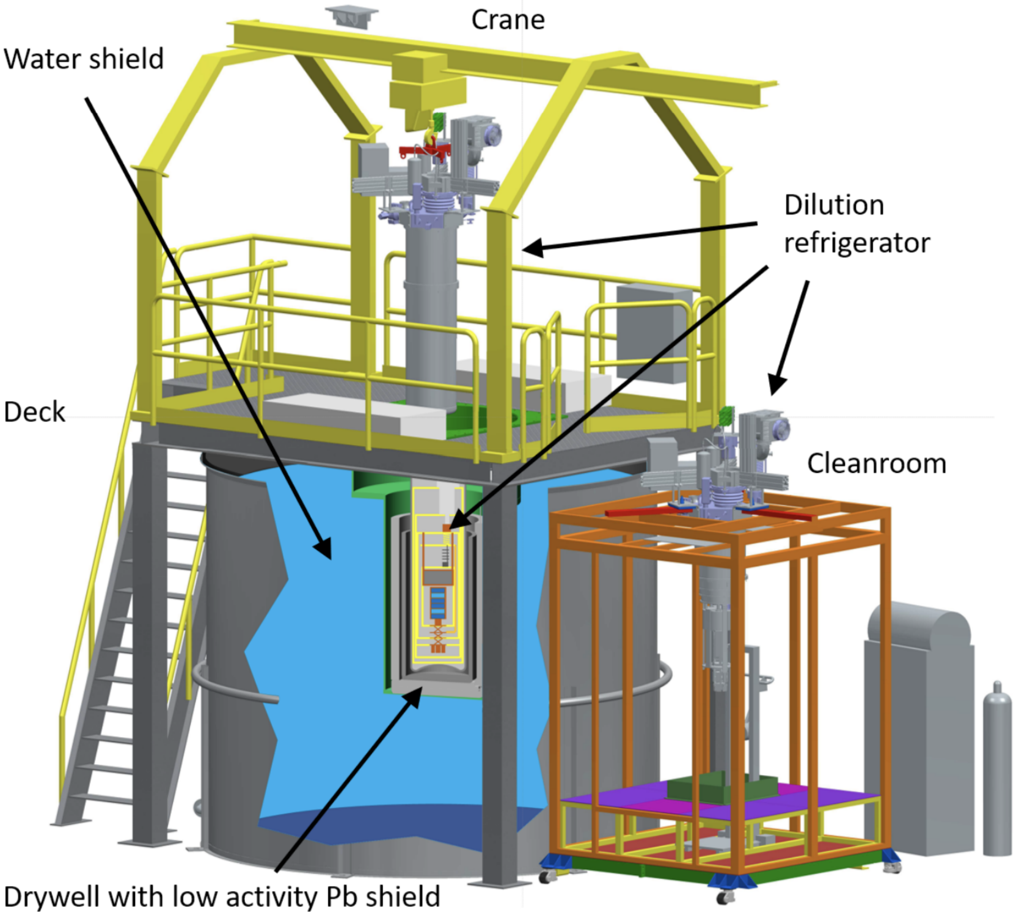

Figure 3.13: The schematic of the CUTE facility. The layout includes a dilution refrigerator inside a drywell at the center of a 3.5-meter diameter water tank, surrounded by 11 cm of lead for radiation shielding. A deck structure with a 20 cm-thick polyethylene shield moderates neutrons from above, which can be moved aside on rails for access to the cryostat. A monorail crane transfers the cryostat between the drywell and the low-radon cleanroom for payload changes. Image taken from [127].

Chapter 4

CUTE Analysis

The CUTE facility at SNOLAB, located adjacent to the SuperCDMS experiments, serves as a necessary testbed for relevant characterization studies on SuperCDMS SNOLAB detectors. The facility also accommodates other small-scale cryogenic experiments that require minimal background radiation. By testing the detectors at CUTE, proper functions of the detectors can be ensured after being transported underground. This is particularly important given the extensive time required for the SuperCDMS SNOLAB cryostat to reach its base temperature, making it impractical to cool down only to discover potential setup issues.

During this doctoral research, different contributions were made to the CUTE project through the execution of remote shifts, which ensured optimal experimental operation. Responsibilities included detector performance monitoring, anomaly detection, and the acquisition of high-quality data for subsequent analysis. Involvement extended beyond operational aspects, including active engagement in collected data analysis in collaboration with the CUTE sub-working group. Advanced statistical methods and machine learning techniques were also employed for data processing and interpretation. The hands-on experience facilitated the development of a comprehensive understanding of the intricate data analysis pipeline utilized in the search for dark matter signals.

The data collected from the CUTE facility was essential for validating the performance of the detectors prior to their installation underground. By thoroughly characterizing the detectors' response, energy resolution, and noise levels, the CUTE team was able to ensure that the detectors were functioning as expected and met the necessary requirements for the main SuperCDMS SNOLAB experiment. This pre-screening process was crucial for minimizing the risk of potential issues during the final deployment and data-taking phase at the SNOLAB underground facility.

Since the CUTE facility has been operational, several different SuperCDMS detectors have been tested including: a SuperCDMS Soudan iZIP detector (T5Z2), a SuperCDMS SNOLAB HV Ge prototype (G124), a SuperCDMS SNOLAB HV Si prototype (S101), two wide area athermal silicon detectors (PD2 and CPD). This section will discuss some of the analysis results obtained with these devices.

4.1. LED Stability Test

Crystal impurities can retain a net charge when cooled to the extremely low temperatures employed by SuperCDMS detectors. As charge carriers move through the detector, they may be drawn to these impurities rather than the electrodes, leading to an underestimation of the scatter energy due to reduced charge signal collection at the electrodes. To mitigate this issue, the detectors are equipped with light emitting diodes (LEDs) that periodically illuminate the crystals, a process referred to as "flashing" or "baking". The photons generated by the LEDs create an abundance of electron-hole pairs, which effectively neutralize the impurity sites' net charge, ensuring optimal signal collection.

Maintaining the detectors in a neutralized state was essential for achieving complete charge signal collection. However, this neutralized condition is temporary and can be disrupted when a sufficient number of charge carriers become trapped by crystal impurities or defects, distorting the electric field configuration and diminishing subsequent charge signals. The duration of each experimental series was limited by the detectors' ability to sustain their neutralized state. During the CUTE runs, these durations typically last around several hours and were referred to as individual "series". At the conclusion of each series, the detectors underwent a flashing process using infrared (IR) photons emitted by LEDs installed within the detector housings. This procedure released the trapped charges, necessitating a 10-minute cooldown period before the commencement of the next series.

Ensuring the stability and proper functioning of the LED system is a necessary precursor to conducting meaningful measurements and analyses within the CUTE experiment. One analysis example is CUTE Run 19, which included a LED housing for maintaining the detectors in a neutralized state. To better understand the LED's impact on the overall stability of the experiment, analysis of the its performance before and after the baking process was conducted. During CUTE Run 19, the detector payload included the LED housing, iZIP detector T5Z2, PD2, CPD and a TES sample. A 1.4 kg prototype SuperCDMS high-voltage germanium detector (designated as G124) was in stack but not connected. A LED stability test was performed using CUTE Run 19 data on T5Z2, PD2 and CPD detectors.

Run 19 involved a total of four LED bake times:

- 21st December, 2020, 00:55–12:14 (˜11 hours, 20 minutes long)
- 6th January, 2021, 01:48–12:02 (˜10 hours long)
- 11th January, 2021, ˜15:00 (1 hour, 7 minutes long)
- 11th January, 2021, 18:08–19:08 (1 hour long)

The factors influencing the LED baking process were investigated, and the effects of the bake on the overall performance of the detector were analyzed by examining the events that occur before and after the baking procedure in this study. Coincidence events between T5Z2, PD2, and CPD were leveraged to apply coincidence cuts. This allowed a clearer presentation by removing most of the background events through coincidence cuts. Figure 4.1 and Figure 4.2 show an example of comparison in one of the channels of the T5Z2 detector, with the data before the coincidence cut presented in Figure 4.1, and the data after the cut shown in Figure 4.2.

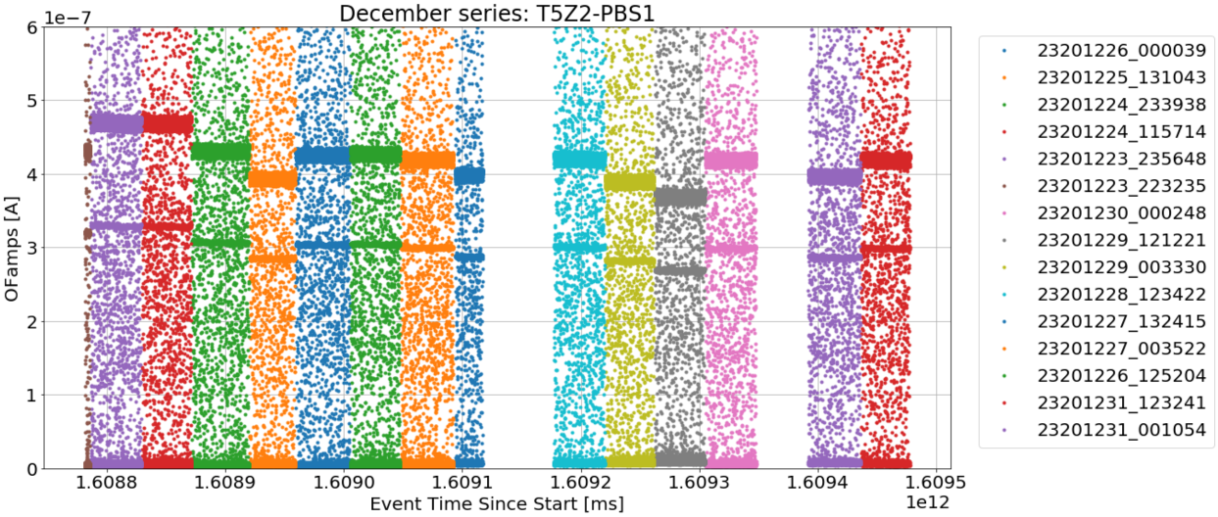

Figure 4.1: Events of T5Z2 detector during December operation before the coincidence cut. Colors denote the operation date and time for individual series.

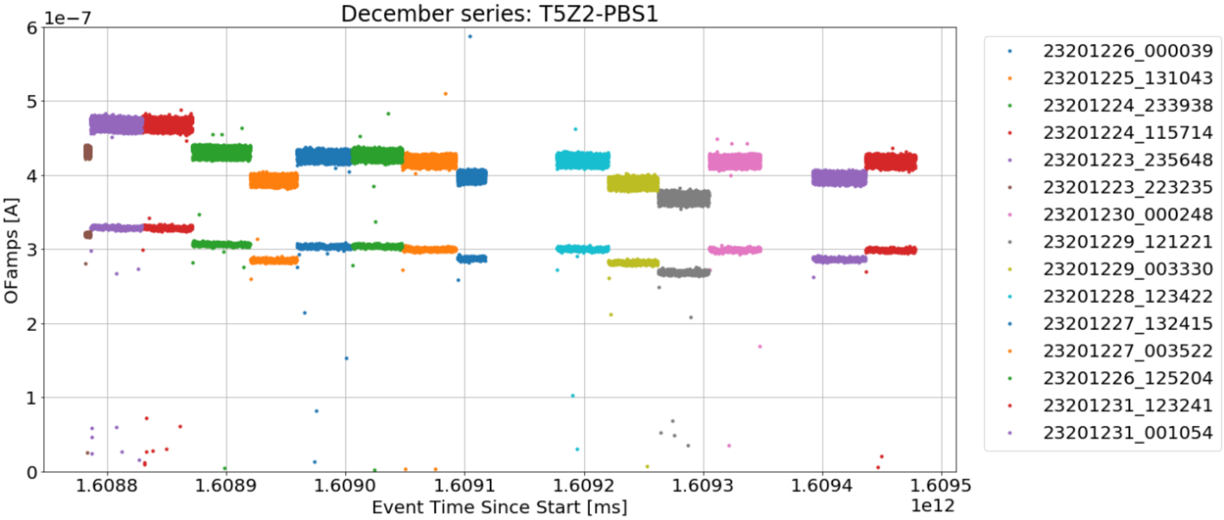

Figure 4.2: Events of T5Z2 detector during December operation after the coincidence cut. Colors denote the operation date and time for individual series.

Although no large fluctuation in stability was observed following the LED bake on December 21st, as the first high-quality series was recorded on December 23rd, the January series revealed a more pronounced pattern. In each instance, a significant decrease in stability was noted immediately after an LED bake was performed in January shown in Figure 4.4 for the PBS1 channel of T5Z2 and Figure 4.3 for the CPD detector.

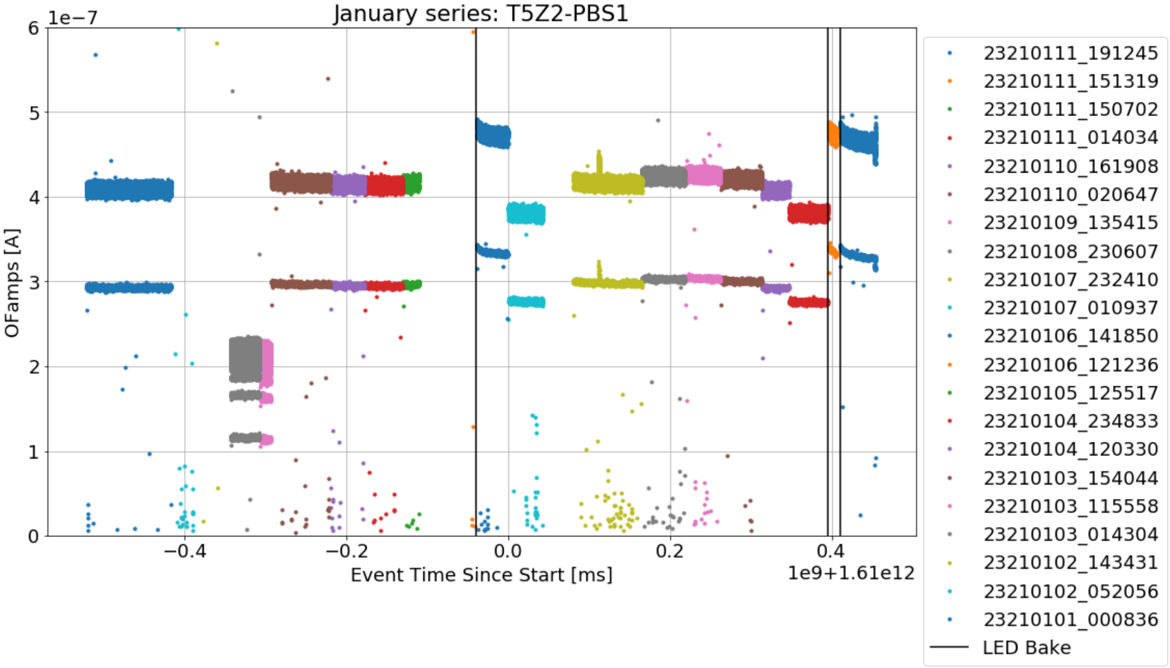

Figure 4.3: Events of T5Z2 detector on January after the coincidence cut. Vertical lines in black indicate the end of each LED baking.

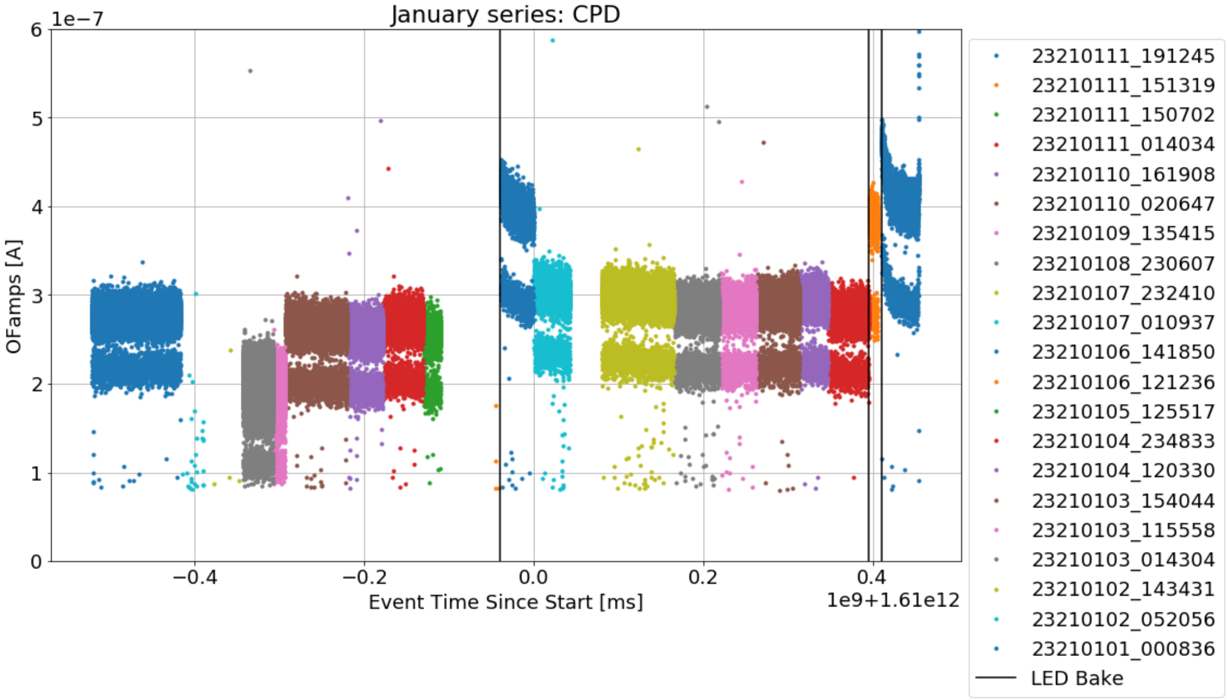

Figure 4.4: Events of PD2 detector on January after the coincidence cut. Vertical lines in black indicate the end of LED baking.

Black vertical lines in Figure 4.4 and Figure 4.3 mark the end of each LED baking session. Immediately following the conclusion of each bake, a noticeable decrease in event amplitude was observed from both detectors. While the post-bake amplitude decreased in a consistent pattern throughout the January series of Run 19, a unique anomaly was discovered during the in-depth analysis of LED stability over time. This anomaly, which deviates from the typical post-bake behavior, warrants further investigation.

During the analysis of the LED stability over time in Run 19, an anomaly was observed in the time series 23210107_232410. As illustrated in Figure 4.5, the Optimum Filter amplitudes (OFamps) of the LED events exhibit an initial increase followed by a decay back to the stable amplitude. This behavior is consistent across all channels, although it is less obvious to discern on the PD2 detector. Additionally, a distinct change was noticed in the events with the lowest amplitude. The onset of the anomaly, the conclusion of the low amplitude event excursion, and the termination of the anomaly, when the LED amplitude returns to its nominal value, are all clearly marked in Figure 4.5.

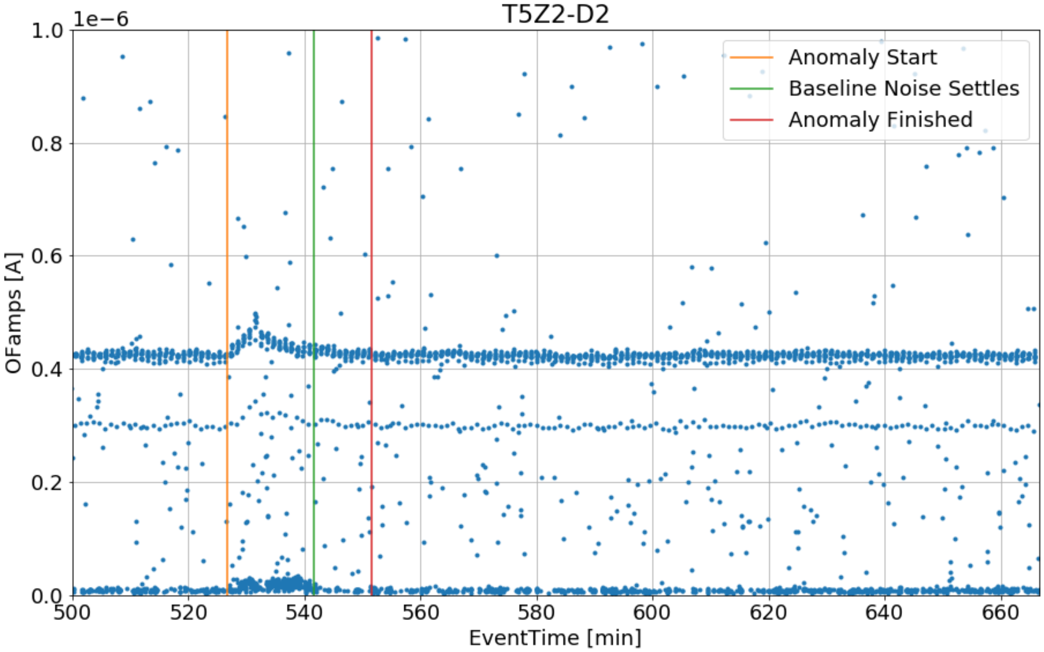

Figure 4.5: Events of PD2 detector on January after the coincidence cut. Vertical lines in black indicate the end of LED baking.

For the purpose of clarity and convenience, the event time has been redefined to start from the first triggered event. In order to characterize the average noise presented in the detector during this anomaly, the power spectral density (PSD) in the frequency domain was computed for each channel at three distinct intervals: prior to the anomaly, during the anomaly, and following the anomaly. These PSDs are depicted in Figure 4.6.

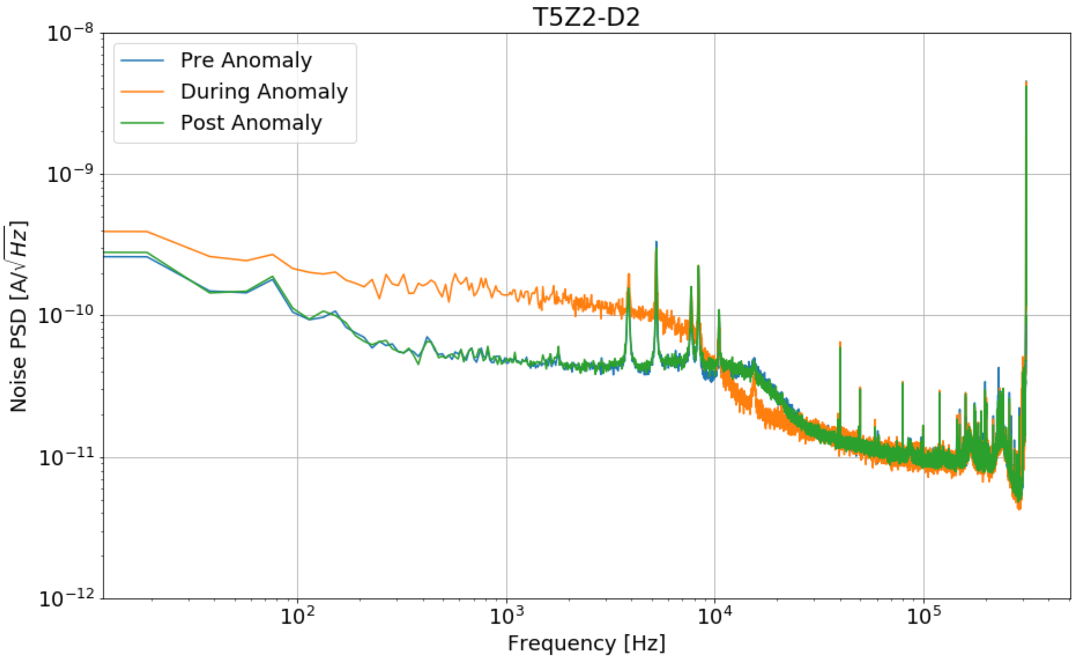

Figure 4.6: Events of PD2 detector on January after the coincidence cut. Vertical lines in black indicate the end of LED baking.

The PSD reveals an elevated noise level in the lower frequency range during the anomalous period compared to the pre-anomaly and post-anomaly intervals. Further analysis performed on the thermometry readout and damper positions throughout the affected series lays the groundwork for understanding and mitigating such anomalies in future experiments, enhancing the reliability and accuracy of the data collection in CUTE.

4.2. Barium Calibration

The CUTE facility is equipped with two calibration systems to perform detector characterization: a gamma calibration system and a neutron calibration system. The gamma calibration system utilizes a ^{133}Ba source, while the neutron calibration system makes use of a ^{252}Cf source. Detailed analyses have been performed using the data acquired through operations with the barium source, enabling detector characterization with calibration.

Both radioactive sources are stored in appropriately shielded housings, and the systems are designed to allow for remote deployment of the sources without requiring on-site personnel. The ^{133}Ba source is housed in a lead enclosure mounted on the drywell, and can be remotely positioned within the shielding using a stepper motor system. A schematic of this ^{133}Ba source deployment mechanism is shown in Figure 4.7.

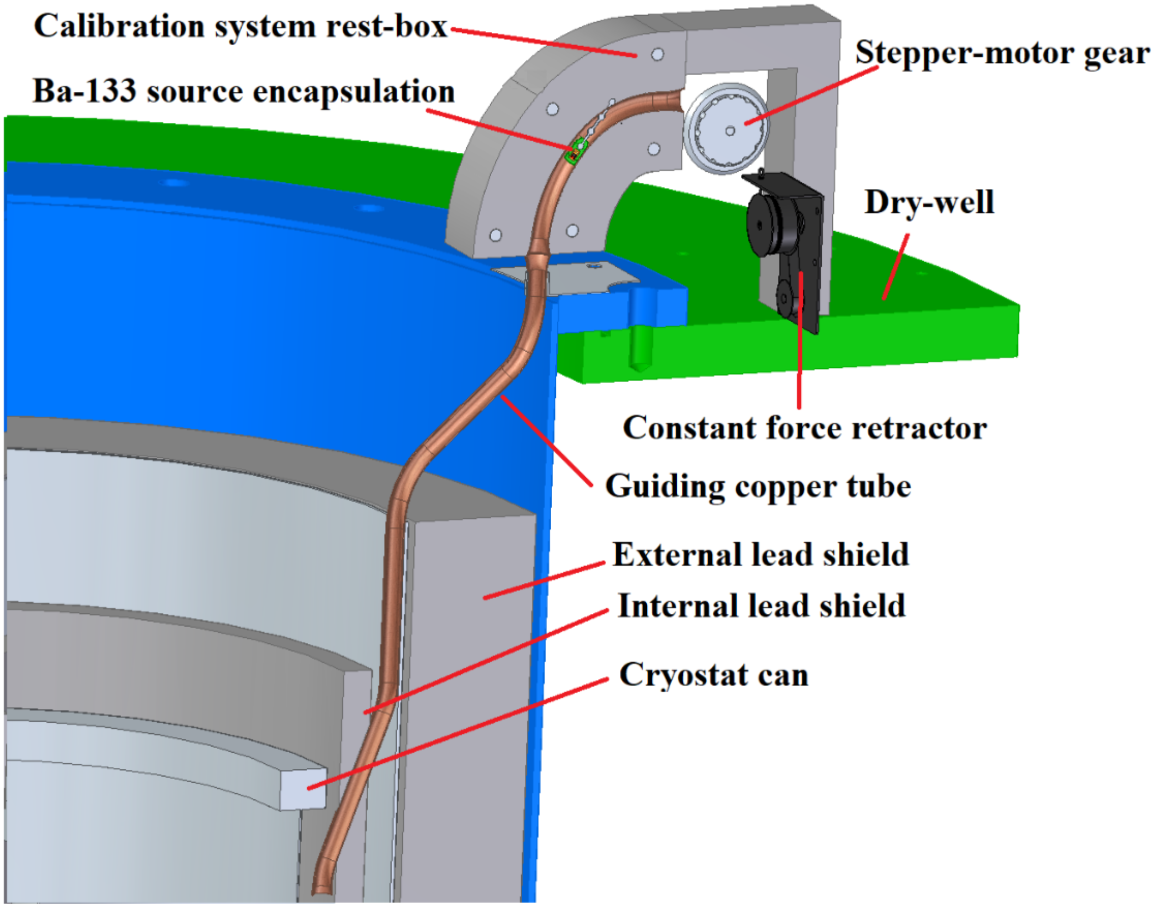

Figure 4.7: Schematic of the gamma calibration system, which lowers an encapsulated ^{133}Ba source into the shielding by a stepper motor system. Image taken from [77]

.

During CUTE Run 18, the barium source was deployed in different series to calibrate the T5Z2 detector and determine the optimal source position for subsequent calibrations. In several of the deployment series, a prominent peak is featured in the spectra, corresponding to the 356 keV gamma ray from the barium source [128]. This characteristic peak was used to calibrate the optimal filter amplitude of the T5Z2 detector. Figure 4.8 highlights an example series demonstrating the Gaussian fit (red line) to the 356 keV peak from the barium source, with the fit parameters including amplitude, mean, and standard deviation. The series number indicates the date and time when the data was collected. The “115 cm HR” label signifies that this series was taken with the source positioned at 115 cm, resulting in a high event rate observed in the detector.

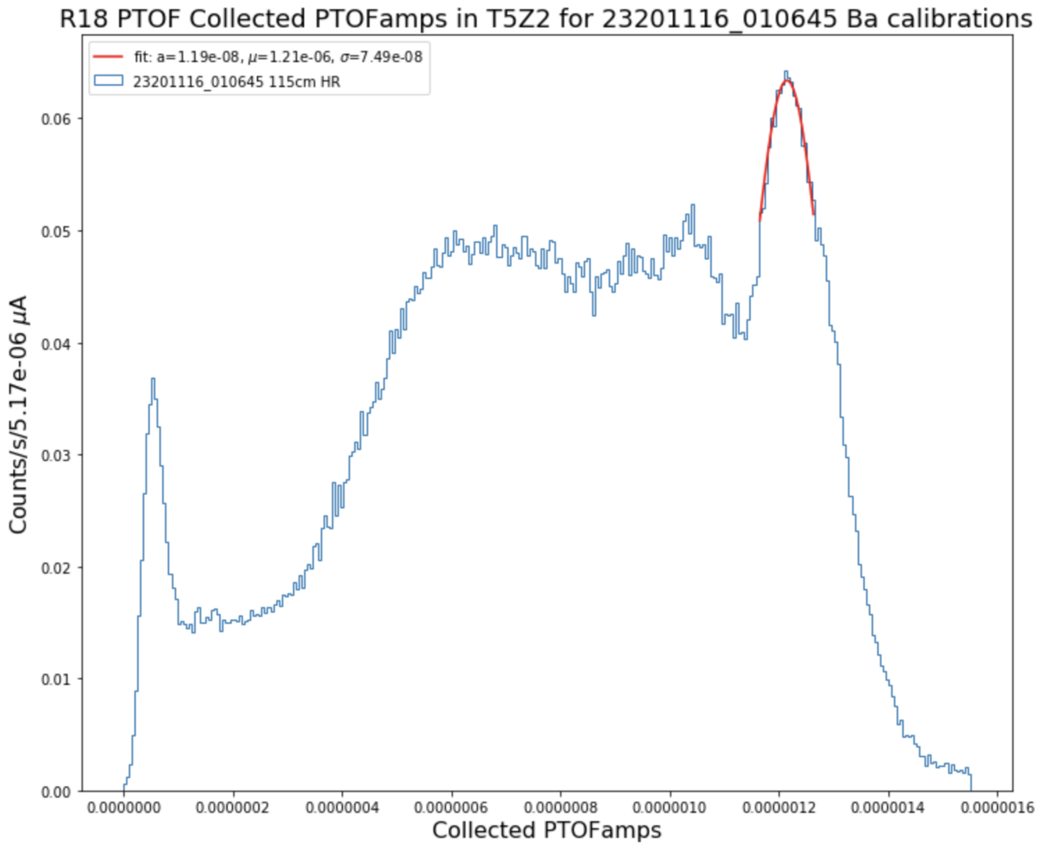

Figure 4.8: Gaussian fit (line in red) to the 356 keV peak from the barium source. The barium source was positioned at 95 cm with a high event rate (HR) observed in the detector.

The calibration was performed by fitting a Gaussian function to the position of the optimal filter amplitude peak and aligning it to the known 356 keV energy peak. The resulting spectra can be found in Figure 4.9. Comparing the spectra of the series where the source was deployed to the low-background series without the source, a clear difference in the measured event rate is observed, indicating the successful deployment of the source.

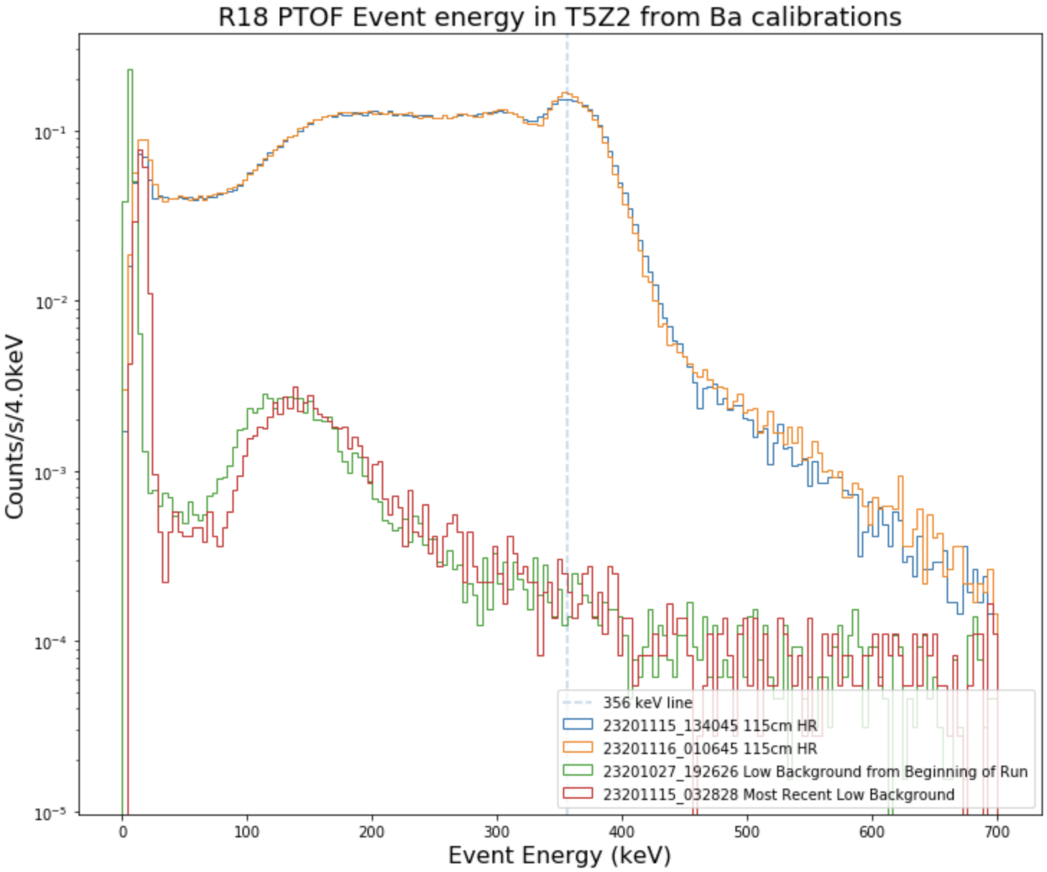

Figure 4.9: Measurements of spectra with and without a barium source for the T5Z2 detector. The 356 keV peak from the series with the source at 115 cm was used to calibrate high-rate events. A difference between the measured event rate is observed, indicating the successful deployment of the barium source.

4.3. Noise Clustering

Emerging experimental techniques often introduce new noise sources that present classification and modeling challenges. In response to this, it is important to explore the application of machine learning (ML) techniques to conduct an unsupervised analysis of the noise characteristics. The goal is to leverage ML clustering methods to identify and reject noise signals that resemble low-amplitude pulses, thereby improving the overall signal-to-noise ratio of the experiment.

The k-means algorithm is a widely utilized unsupervised machine learning technique that can be highly effective in identifying and separating distinct components within complex time-series data [129]. This approach can be employed to disentangle various sources of background noise from the signals of interest, identifying low-amplitude pulses from noise.

In the pre-processing stage, the raw data was extracted as digitized pulse traces from the sensor readout. However, most of these pulses in the dataset are quite noisy. K-means, an unsupervised approach, was utilized to characterize these noises. Prior to applying the k-means clustering, data from multiple channels of the same detector was consolidated by aligning the segments with overlapped operation time.

The silhouette score was used for evaluating the quality of k-means clustering results [130]. It provides a measure of how well each data point fits within its assigned cluster, compared to how well it would fit in neighboring clusters. In our analysis, each multivariate time series from the raw traces was regarded as one "data point". The silhouette score ranges from -1 to 1, with higher values indicating better-defined clusters. It was calculated by first determining the average distance between each data point and all other points in its assigned cluster, and then computing the average distance to the nearest neighboring cluster. The silhouette score was then calculated as the difference between these two average distances, divided by the maximum of the two given by

$$s_i = \frac{b_i - a_i}{\max(b_i, a_i)} \tag{4.1}$$

where b_i is the inter cluster distance defined as the average distance to closest cluster of datapoint i, and a_i is the intra cluster distance defined as the average distance between data point i and all other points within the same cluster.

Table 4.1 shows an example of the clustering silhouette scores measured using the k-means method, comparing the results for single-channel and multi-channel data. A slight improvement in the silhouette score is observed by combining the raw time-series traces from multiple channels and flattening the data into a unified feature set.

Table 4.1: Silhouette scores from k-means clustering for noise in different channels.

Channels	Silhouette score
PAS2	0.806723526444267
PBS2	0.802746091725295
PDS2	0.801753793857405
All channels (Flattened)	0.809138555874168

Examining the silhouette scores for different choices of the number of clusters k, we observe that the rate of change in the scores starts to diminish around 4-5 clusters. This suggests that 5 may be a reasonable number of clusters to select, as increasing the number of clusters further does not lead to a dramatic improvement in the clustering quality. The stability of the silhouette score around 5 clusters indicates this may be an appropriate configuration to capture the natural groupings present in the data without over-partitioning. An example of the clustering result is shown in Figure 4.10.

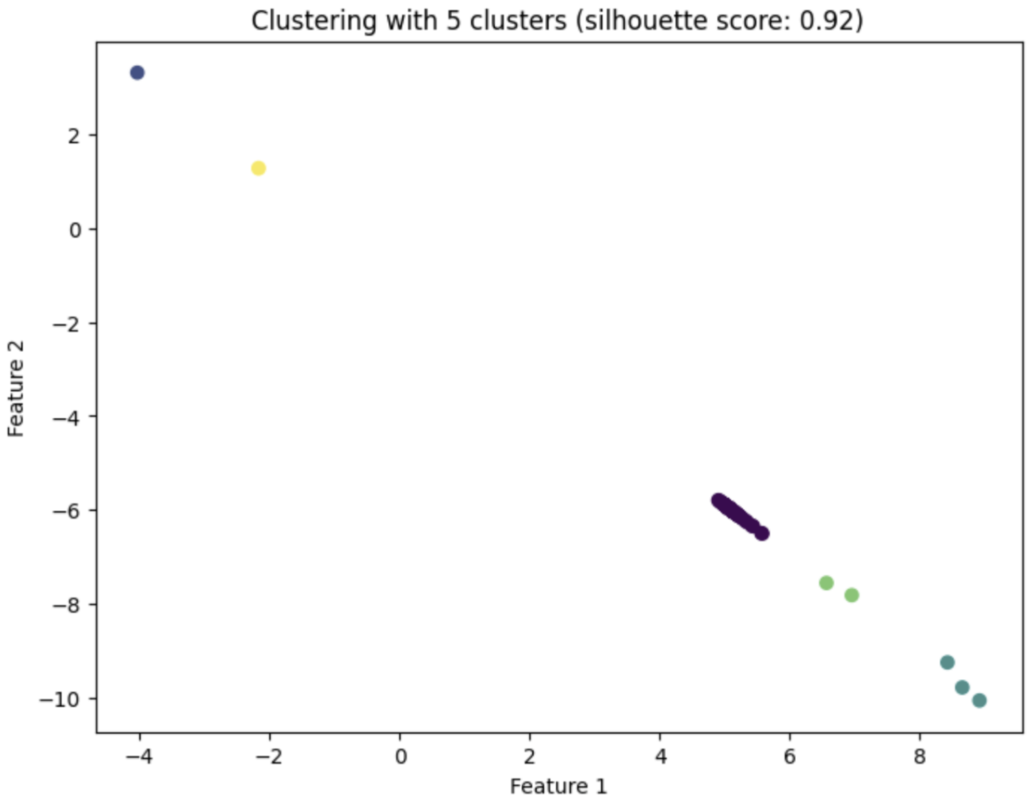

Figure 4.10: Visualization of K-means clustering for datasets with k = 5. Sihouette score is 0.92 in this example.

This unsupervised k-means clustering approach was employed to address the challenge of unknown noise sources in the detector. This method allowed similar noise patterns to be grouped without prior knowledge of their origins. By analyzing time-series data from multiple channels, distinct clusters were identified that potentially represent different types of noise or signal characteristics. While this initial clustering provided valuable insights, there is room for further refinement of the technique. Future work could explore the implementation of recursive k-means clustering, where the process is applied iteratively to subsets of the data. This approach might reveal more complex noise structures and improve the ability to distinguish between genuine signals and various noise sources. Such enhancements could lead to more effective noise reduction strategies and ultimately improve the detector's sensitivity in the search for rare events.

CHAPTER 5

CDMSlite Run Data

The CDMSlite experiment's Run 3 data was previously utilized in the search for dark photons and axion-like particles [46]. However, the work presented in this dissertation represents the first time that this data set was used to search specifically for solar axions produced by the ABC reactions. The Run 3 data was collected in two distinct sub-runs during 2015. The first sub-run, referred to as Run 3-1, occurred during February and March, while the second sub-run, known as Run 3-2, took place from April to May.

5.1. Data Quality

Due to fluctuations from the phonon noise performance during the operation of detectors, the Run 3 dataset was further categorized into two periods, each characterized by unique cut efficiencies and resolutions [131]. Although the analysis treated these two periods independently, the signal and background models were standardized for the combined dataset. After applying all necessary cuts, the effective livetime for Run 3-1 and Run 3-2 was determined to be 31.50 days and 29.39 days, respectively. The total livetime for CDMSlite Run 3 operation is 60.9 days [131]. A summary of the exposure of four iZIP detectors in kg·days for each run can be found in Table 5.1.

Table 5.1: The exposure of CDMSlite Run2, Run 3-1, and Run 3-2.

	Run 2	Run 3-1	Run 3-2
Exposure (kg·days)	70.1	31.5	29.39

Beginning in 2012, the SuperCDMS Soudan experiment conducted three distinct data collection campaigns, each featuring detectors operating in the specialized CDMSlite mode configuration. Run 3 selected the uppermost detector in the second tower, which was based on two critical factors that significantly contributed to achieving lower analysis thresholds. Firstly, this particular detector demonstrated reliable performance across a wide range of applied bias voltages, reaching nearly 75 V. Secondly, due to its inherent resilience against vibrational noise, the chosen detector exhibited exceptional phonon energy resolution, ranking among the finest within the entire detector array. [131]

The CDMSlite data quality cuts were implemented to identify and remove events likely triggered by noise, events with suboptimal energy reconstruction, and time periods where the detector's performance deviated from the expected behavior. These livetime cuts involve the exclusion of specific time intervals based on certain criteria, such as the removal of periods with improper high voltage power supply settings or coinciding with the NuMI neutrino beam directed towards the MINOS experiment at the Soudan Underground Laboratory [132]. These cuts help eliminate events that are coincident with the neutrino beam. Furthermore, triggers in the CDMSlite detector that coincided with triggers on other detectors were also removed, as the anticipated rate of dark matter interactions is sufficiently low that multiple simultaneous triggers are not expected.

Data quality cuts are designed to remove events with anomalous features as well. Such cuts eliminate events where the pre-trigger baseline current exceeds its time-averaged value by more than four standard deviations, while another removes events likely triggered by excessive electronic noise. Several classes of events with unusual pulse shapes were identified in the triggered data. To remove these events, glitch templates were created, and events were fitted to both the regular pulse template and the glitch templates. The difference in fit quality χ^2 was then used to determine whether an event resembled a genuine pulse or was more likely caused by noise. Lastly, events occurring near the detector's outer edges were removed using a fiducial volume cut. The removal of these events is important because they experience reduced NTL amplification due to the inhomogeneous electric field in the detector and are reconstructed at a lower energy. Moreover, the expected background near the detector's edge could be higher due to the radioactive impurities from the detector housing or the crystal surface.

5.2. Signal Efficiency

The event selection criteria, as well as the signal efficiency with associated uncertainties, are consistent with those deployed in the WIMP searches conducted during CDMSlite Run2 and Run3 [131,133]. Figure 5.1 illustrates the signal efficiency as a function of the measured energy, showing the proportion of all detected events that met the data selection criteria at each specific energy level.

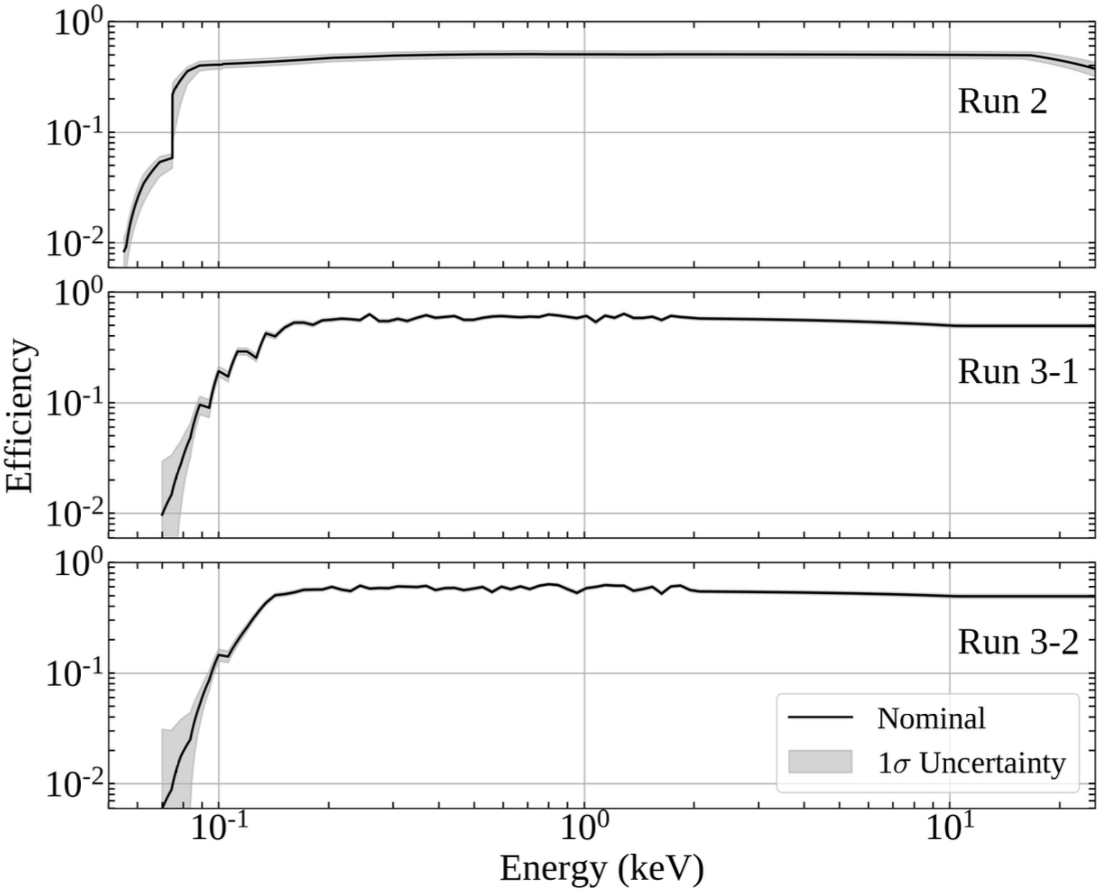

Figure 5.1: Signal efficiency for CDMSlite Run 2, Run 3 Period 1, and Run 3 Period 2 in the top, middle, and bottom subplots respectively. The nominal efficiencies are in solid lines, and 1σ uncertainty bands are the shaded regions. Image taken from [46].

At lower energy ranges, the efficiency is primarily determined by the trigger rate [134]. During Run 2, a trigger threshold as low as 56 eV was achieved. However, in Run 3, the trigger rate at low energies was predominantly influenced by noise-induced events. These events were identified and excluded from the analysis based on their distinctive pulse shape characteristics. Consequently, this process led to a reduction in efficiency and an increase in the effective threshold to 70 eV. For events exceeding approximately 100 eV in Run 2 and 200 eV in Run 3, the efficiency reduction exhibits minimal energy dependence and is primarily attributed to the radial fiducialization procedure. This procedure involves the removal of events occurring near the detector's edge, where irregularities in the electric field result in diminished NTL amplification [46].

5.3. Energy Resolution

The energy resolution, σ_T, of the SuperCDMS detectors was determined in the original CDMSlite analyses [131, 135] and is given by:

$$\sigma_T = \sqrt{\sigma_E^2 + \sigma_F^2(E) + \sigma_{PD}^2(E)} \tag{5.1}$$

where E is the measured energy, $\sigma_E(E)$ is the resolution of the baseline noise, and $\sigma_F(E)$ quantifies the uncertainty caused by the number fluctuations of the electron-hole pairs, taking into consideration the Fano factor. This component is proportional to the square root of the energy and is parameterized as $\sigma_F(E) = \sqrt{BE}$, where B is a constant. The third component, $\sigma_{PD}(E)$, introduces a term that scales linearly with energy E and encompasses factors such as position dependence within the detector. This component is parameterized as $\sigma_{PD}(E) = AE$, where A is another constant. [46]

The linear relationship between the term σ_F^2 and energy E came from the variation in the number of electron-hole pairs N and the Fano factor F, which is expressed as

$$\sigma_F^2 = FN\epsilon_\gamma^2 = F\epsilon_\gamma E \tag{5.2}$$

where ϵ is the average energy required to create an electron-hole pair, and γ is the average charge collection efficiency. On the other hand, the σ_{PD} term accounts for variations from detector-specific effects, such as position dependence, which are expected to scale proportionally with energy. This term also encompasses any other energy-dependent effects that may influence the energy resolution of the detector.

The values of the three free parameters in the resolution model (A, B, and σ_E) are determined by fitting Eq. 5.1 to the observed widths of the Gaussian fits applied to the electron capture peaks of Germanium, as well as the baseline width arising from electronic noise. In the CDMSlite detectors, the established peaks in the energy spectrum correspond to the electron capture events involving the K-, L-, and M-shells of ^{71}Ge, which occur at energies of 10.37 keV, 1.30 keV, and 0.16 keV, respectively [46]. Table 5.2 presents the peak position μ and resolution σ for each of the ^{71}Ge peaks.

Table 5.2: Reconstructed energies and resolutions of the ^{71}Ge decay peaks and the baseline noise in CDMSlite Run3 period 1 and period 2. Table taken from [131].

Peak	Energy μ [keV$_{\text{ee}}$]	Resolution σ [eV$_{\text{ee}}$]
K shell	10.354 ± 0.002	108 ± 2.0
L shell	1.328 ± 0.003	36.3 ± 2.0
M shell	0.162 ± 0.002	13.9 ± 2.0
Baseline Period 1	0.0	9.87 ± 0.04
Baseline Period 2	0.0	12.67 ± 0.04

Figure 5.2 illustrates the fits to the K-, L-, and M-shell peaks, as well as an example of the zero-energy noise distribution of the baseline.

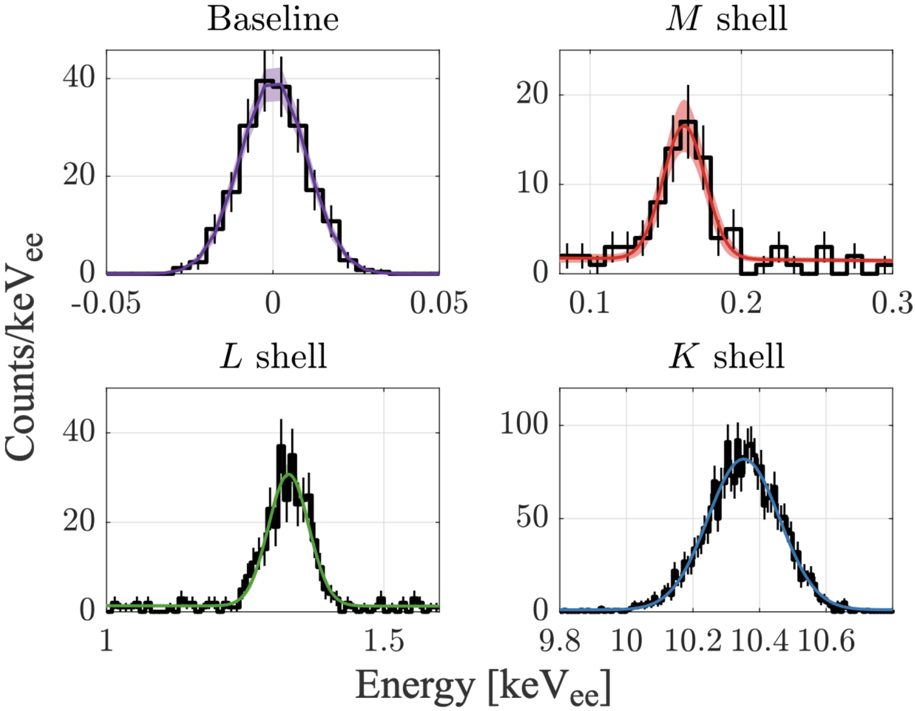

Figure 5.2: Fits of a Gaussian and linear background to the energy spectra of baseline events with zero energy and events from each ^{71}Ge activation peak. The widths of the Gaussians are the energy resolution σ. Image taken from [131].

The uncertainties associated with these Gaussian widths are used as weights in the fitting process to extract the model parameters and their corresponding uncertainties are listed in the following table:

Table 5.3: Parameters for the resolution model with uncertainties for CDMSlite Run 3-1 and Run 3-2. Table taken from [46].

	σ_E (eV)	B (eV)	A ($\times 10^{-3}$)
Run 3-1	9.87 ± 0.04	0.87 ± 0.12	4.94 ± 1.27
Run 3-2	12.7 ± 0.04	0.80 ± 0.12	5.49 ± 1.13

The resolution model for the iZIP detectors is also determined by fitting Eq. 5.2 to the observed widths of several pre-defined peaks in the energy spectrum. These peaks include the K-shell electron capture peak of ^{71}Ge at 10.37 keV, the inelastic scattering on ^{73}Ge during ^{252}Cf calibration at 66.7 keV, the peak of ^{133}Ba calibrations at 356 keV, and the peak from electron-positron annihilation at 511 keV. The exposure and fitted energy resolution parameters of the four iZIP detectors employed in Run 2 and Run 3 are presented in Table 5.4, which presents the resulting model parameters along with their statistical uncertainties derived from the fit, while systematic uncertainties are found to be relatively insignificant.

Table 5.4: Exposure and fitted parameters for the energy resolution of the four iZIP detectors. Table taken from [46].

	σ_E (eV)	B (eV)	A ($\times 10^{-3}$)	Exposure (kg·days)
T1Z1	100.5 ± 3.4	2.7 ± 0.5	19.5 ± 0.1	80.2
T2Z1	69.9 ± 4.6	2.4 ± 1.1	15.4 ± 0.3	82.9
T2Z2	79.0 ± 2.9	1.2 ± 0.3	13.6 ± 0.1	80.9
T4Z3	80.2 ± 5.4	0.6 ± 1.2	19.0 ± 0.4	83.8

Figure 5.3 presents the resolution model derived from the fitting process, showing separate plots for CDMSlite Run 2, Run 3 Period 1, and Run 3 Period 2. Although the Ge K-shell capture line at 10.37 keV represents the highest energy point used in the fits, the model was presumed to maintain its accuracy throughout the entire analysis range. The uncertainty bands were constructed by assessing the resolution model using the best-fit parameters in conjunction with their respective uncertainties, with the upper band corresponding to the addition of the uncertainties and the lower band to their subtraction. This approach yields a conservative 1σ uncertainty band.

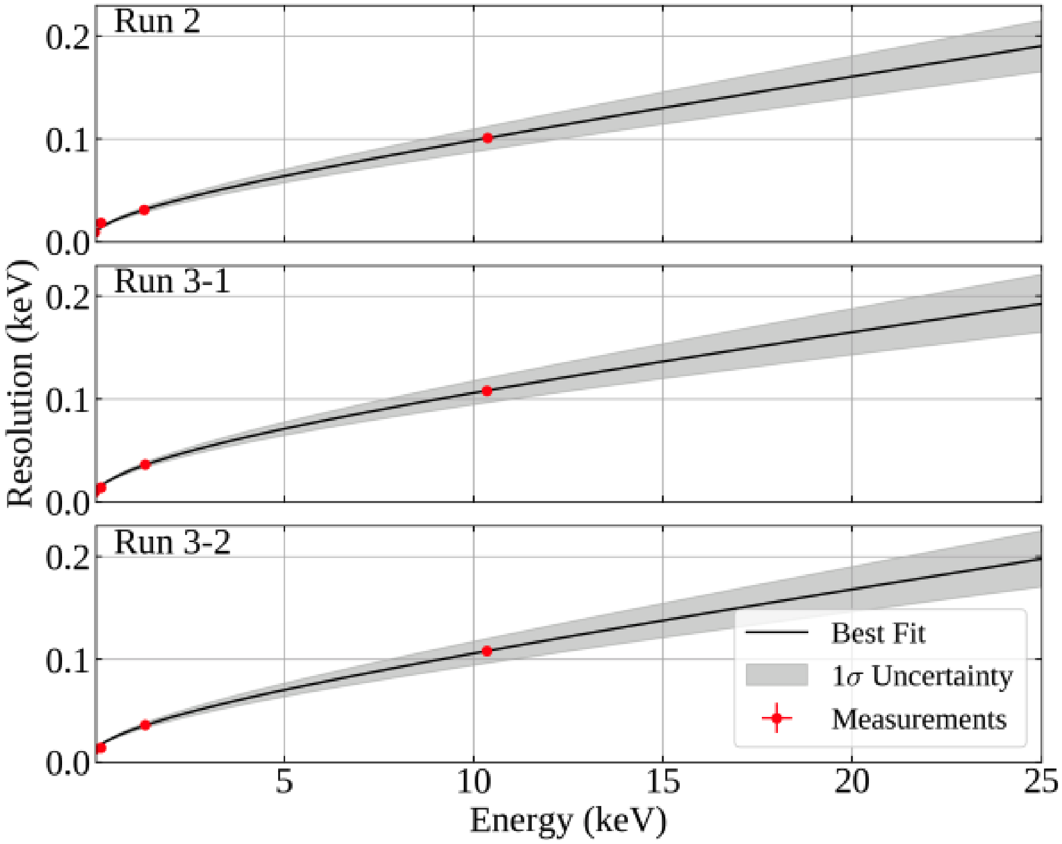

Figure 5.3: The energy resolution models for CDMSlite Run 2, Run 3-1 and Run 3-2. The best-fit curves (solid lines) and 1σ uncertainty bands (shaded regions) are shown with the measured widths of the three Ge electron capture peaks and the baseline noise resolution. The top, middle, and bottom panels show the models for Run 2, Run 3 Period 1, and Run 3 Period 2, respectively. Image taken from [46].

Similarly, the iZIP detectors employ a resolution model that shares the same functional form as the one used in the CDMSlite analysis, as described in Eq. 5.1. The model was fitted to the resolution of five distinct peaks, taking into account their associated uncertainties. These peaks include the four peaks used for energy scale calibration and the baseline noise peak. The model parameters and the corresponding 1σ uncertainty band on the resolution were independently determined for each detector. The upper and lower edges of the uncertainty band were obtained by considering the upper and lower values of the 1σ confidence interval for each parameter, as determined by the fitting procedure. Figure 5.4 illustrates the model for the T2Z2 detector as an example, showing the measured peak energies and widths to which the model is fitted. It is representative of the highly similar energy resolution models exhibited by all four iZIP detectors.

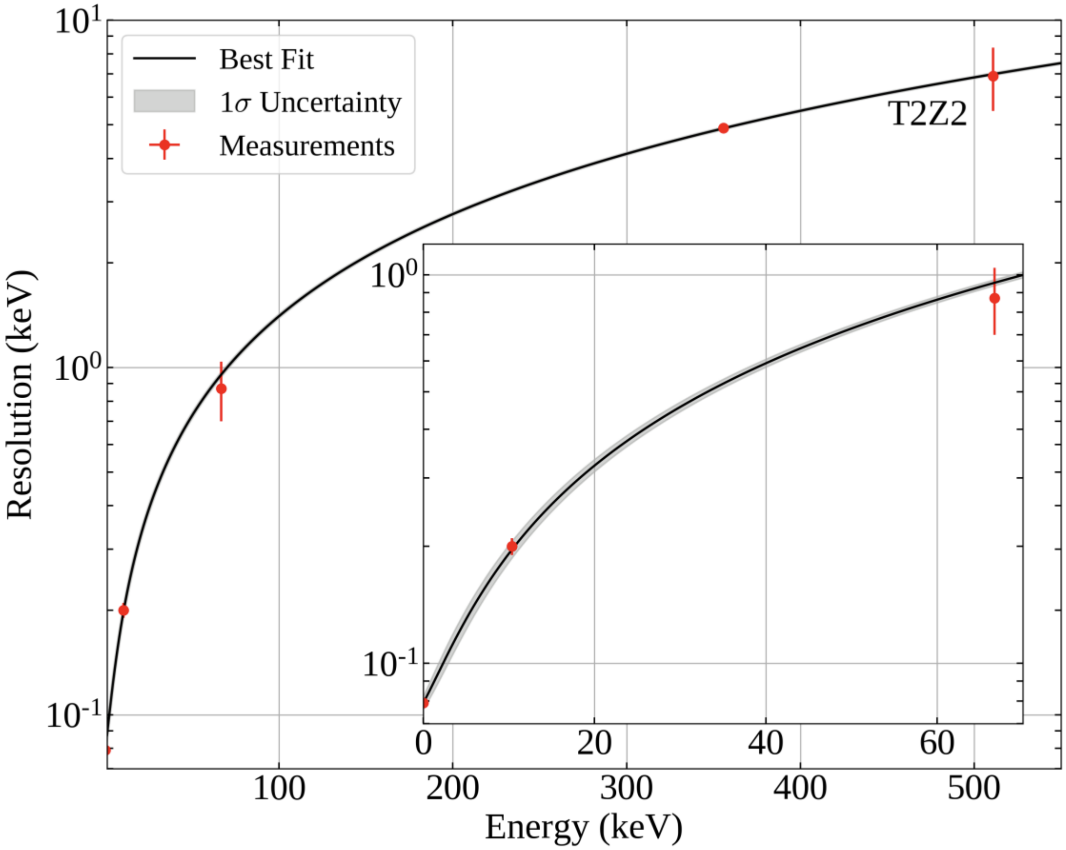

Figure 5.4: The fitted resolution model used in the iZIP analysis, using detector T2Z2 as an example. The measured peak widths (points) are used to determine the best-fit curve (solid line) and 1σ uncertainty band (shaded region). The inset plot shows a zoomed-in plot of the region between 0 and 70 keV. Image taken from [46].

5.4. Blinding Strategy for CDMSlite Run3

Analysis of CDMSlite R3 data was the first CDMSlite search performed on blinded data, where a novel blinding scheme was implemented to prevent bias. Different from previous SuperCDMS analyses with iZIPs that employed a “black box” approach, where events within a specific range of recoil energy and yield were removed, the CDMSlite R3 analysis adopted a data "salting" method. This approach allowed analyzers to view all events throughout the analysis while still blinding the true amount of potential dark matter signal, which was particularly important given the significant and time-varying nature of instrumental noise.

The salting process involved replacing a randomly selected portion of events (between 280 and 840) with artificial signal-like events, effectively masking the true amount of dark matter signal present in the data. The exact number and energy distribution of these salt events were kept hidden until the final stage of the analysis. Upon unblinding, it was revealed that 393 events had been replaced, and after applying selection cuts, 105 salt events remained in the signal region, constituting 26% of the total events in that region.

Salt events were chosen randomly from the data set with a uniform time distribution. The waveform data of selected events was replaced with artificial pulses, while preserving metadata such as trigger masks and timestamps. A pre-selection cut requiring reconstructed energy greater than 3.5 keV removed most cryocooler-induced noise events. The energies of the salt events were chosen from an exponential distribution with a constant offset, designed to roughly approximate a WIMP spectrum:

$$P(E) \propto C + \frac{1}{D}\exp\left(-\frac{E}{D}\right), \quad E \in [0.05, 5]\mathrm{keV}_{ee} \tag{5.3}$$

where C and D are randomized hidden parameters, sampled logarithmically from 1/3 to 3 $\mathrm{keV}_{ee}{}^{-1}$ for C, and from 0.5 to 2 keV_{ee} for D. The chosen energy was restricted to the range of 0.05 to 5 keV_{ee} to match the expected signal region of interest. The randomly selected parameters used for the CDMSlite R3 salting were C = 0.6967 $\mathrm{keV}_{ee}{}^{-1}$ and D = 1.299 keV_{ee}, resulting in a nearly uniform distribution of salt events over the CDMSlite region of interest. Table 5.5 summarized all the random parameters were used.

Table 5.5: Randomized parameters used to generate the unknown salt data set. The units of the second and third row are keV_{ee} and ${\text{keV}_{ee}}^{-1}$ respectively. The allowed range of parameters was known in advance, while the final value was hidden until unblinding after all cuts were finalized. For parameters that required logarithmic weighting, a uniform distribution was employed to randomly select values for the logarithm of those parameters, ensuring they fell within the predetermined upper and lower limits. Table taken from [131].

Parameter	Range	Weight	Actual Value
Number of slated events	280 - 840	linear	393
Spectrum constant weight (C in Eq. 5.3)	1/3 - 3	log	0.6967
Spectrum constant weight (D in Eq. 5.3)	0.5 - 2	log	1.299

Artificial pulses for each salt event were constructed by combining a baseline noise waveform with scaled fast and slow templates from calibration events near the target energy. The relative amplitudes of the fast and slow templates were maintained to simulate uniform bulk event distributions without explicitly modeling those variables.

Before starting the salting process, an inspector would inspect the salt to ensure it did not significantly deviate from the real data. After validation, the inspector was excluded from further analysis of the salted data set.

The decision to replace events with salt, rather than simply adding salt, was made to avoid the need to work around the sequential event IDs that are inherent to the data format. This approach also provided an additional benefit by preventing the potential tendency of excessively tuning cuts to the specific events in the salted data, as they were unknown number of events.

Chapter 6

Search for Solar Axions

This chapter presents a detailed analysis of the solar axion search, focusing on background noise and the mathematical framework of the study. It begins with an examination of various background models, including events from cosmic rays, neutrons from the calibration source, gamma rays, and surface events. Then the potential detection of axions through axio-electric effect with the SuperCDMS detectors will also be explored. Following this, the statistical method will be introduced with an explanation of the profile likelihood analysis used to distinguish the axion signal from background noise. This statistical approach offers a thorough insight into the complexities involved in the search for axions with various backgrounds and the precise processes required to identify these elusive particles.

6.1. Background Models

The SuperCDMS experiment utilizes advanced background models to estimate and exclude non-signal events for the dark matter and axion search. The background sources analyzed include neutron activation by the ^{252}Cf calibration source, cosmogenic activation of the crystal, radiogenic Compton scattering, and ^{210}Pb surface contamination [131]. Models such as Monte Carlo incorporate detailed simulations of various background sources. These simulations were validated against direct measurements of material radiopurity and on-site background data. Additionally, data-driven fits and machine learning techniques are currently being explored to further improve background discrimination [118].

6.1.1. Cosmogenic activation

Exposure to cosmic rays during fabrication, storage, and transportation above ground can lead to spallation reactions, resulting in the cosmogenic activation of the SuperCDMS crystals and apparatus materials. Specifically, this activation can produce radioisotopes within the crystal, such as tritium, ^{68}Ga, ^{65}Zn, and ^{55}Fe, which contribute to the overall background of the experiment. [131]

Tritium (^{3}H), a radioactive isotope of hydrogen, can be a significant source of background in dark matter detection experiments, particularly in low-energy searches. It is produced through cosmogenic activation of the detector materials during exposure to cosmic rays above ground, and it can also be present in the materials used for detector construction [118]. In the case of tritium, non-relativistic β-decay theory is adequate to model its decay spectrum due to the low energy of the emitted electrons. This is because tritium's endpoint energy, also known as the Q-value, is much smaller than the rest mass energy of the electron ($m_e c^2$). Consequently, the kinetic energy distribution of the electrons emitted during tritium decay can be described using the following equation:

$$f_{\text{tritium}}(E_{\text{KE}}) = C\sqrt{E_{\text{KE}}^2 + 2E_{\text{KE}}m_e c^2}(Q - E_{\text{KE}})^2 \times \left(E_{\text{KE}} + m_e c^2\right) F(Z, E_{\text{KE}}) \tag{6.1}$$

where C is a normalization constant, E_{KE} is the electron's kinetic energy, Q is the endpoint energy, and $F(Z, E_{\text{KE}})$ is the Fermi function that accounts for the Coulomb interaction between the emitted electron and the daughter nucleus, which can be described as following:

$$F(Z, E_{\text{KE}}) = \frac{2\pi\eta}{1 - e^{-2\pi\eta}}, \quad \text{with} \quad \eta = \frac{\alpha Z(E_{\text{KE}} + m_e c^2)}{pc} \tag{6.2}$$

where Z is the atomic number of the daughter nucleus formed after the beta decay of tritium, α is the fine structure constant that characterizes the strength of the electromagnetic interaction, and p is the momentum of the emitted electron. These parameters are essential for determining the shape of the tritium beta decay spectrum, which is described by the analytical expressions given in Equations 6.1 and 6.2. The tritium decay spectrum is employed as a component of the background model in the likelihood analysis of the data collected by the SuperCDMS experiments. [131]

The cosmogenically produced isotopes that undergo electron capture (EC) decay and contribute to the measured CDMSlite energy spectrum are summarized in Table 6.1. This table lists the shell energies for each isotope and the relative amplitudes of the different shells, which are all normalized to the K shell. In the CDMSlite detector, these EC decays manifest as Gaussian peaks in the energy distribution, centered at the corresponding shell energies. The width of these peaks is determined by the energy resolution of the detector at the specific shell energy. The specific descriptions of the energy resolution for different shell energies in the CDMSlite runs can be found in Section 5.3, which provides a detailed discussion of the detector's energy resolution and its dependence on the energy scale.

Table 6.1: Table of cosmogenic isotopes that undergo electron capture decay and are observed in the measured energy spectrum of the CDMSlite experiment. μ is the shell energies in keV and Λ is the amplitudes normalized with respect to the K shell. Table taken from [118].

Shell:	K		L_1		M_1	
	μ	Λ	μ	Λ	μ	Λ
^{68}Ge/^{71}Ge	10.37	1.0	1.30	0.1202	0.160	0.0203
^{68}Ga	9.66	1.0	1.20	0.1107	0.140	0.0183
^{65}Zn	8.98	1.0	1.10	0.1168	0.122	0.0192
^{55}Fe	6.54	1.0	0.77	0.1111	0.082	0.0178

In the background models used for the CDMSlite analysis, the relative amplitudes of the K-, L-, and M-shell peaks for each electron capture isotope are assumed to follow the ratios given in Table 6.1. The contribution of these EC isotopes to the measured energy spectrum is described by a sum of Gaussian functions, given by

$$f_{\mathrm{EC_{peaks}}}(E) = \sum_{i=K,L,M} \frac{\Lambda_i}{\sigma_i\sqrt{2\pi}} \exp\left(-\frac{1}{2}\left(\frac{E-\mu_i}{\sigma_i}\right)^2\right) \tag{6.3}$$

where Λ_i represents the amplitudes of the respective shells (K, L, and M), μ_i denotes the shell energies, σ_i corresponds to the energy resolutions at the respective energies, and E is the energy variable.

The number of events in the K shell (Λ_k) would be treated as a free parameter in a likelihood fit, which will be discussed in a later section, while the amplitudes of the L and M shells (Λ_L and Λ_M) are determined based on the branching ratios provided in Table 6.1. This approach reduces the number of free parameters in the fit and ensures that the relative contributions of the different shells for each EC isotope are consistent with the expected branching ratios.

6.1.2. Neutrons from ^{252}Cf

The CDMSlite detectors are calibrated using a ^{252}Cf source, which serves multiple purposes. First, it validates the energy scale calibration of the phonon channels obtained from a barium source, demonstrating that the calibration remains accurate even for nuclear recoils [118]. Second, the ^{252}Cf source activates the germanium detectors by producing ^{71}Ge through neutron capture on ^{70}Ge. The resulting ^{71}Ge isotope also decays via electron capture, emitting low-energy lines at 10.37 keV, 1.30 keV, and 0.16 keV, corresponding to the K-, L-, and M-shell energies of ^{71}Ga, respectively. These peaks are particularly useful for calibrating the CDMSlite detectors, which saturate at lower energies due to the high Neganov-Trofimov-Luke (NTL) gain and cannot rely on the cross-calibration of the ionization channels.

Although the ^{71}Ge EC peaks are used for calibration purposes, they also contribute to the background in the CDMSlite detectors, despite their relatively short half-life of 11.43 days. These peaks are modeled using the same functional form as the cosmogenic EC peaks, described by Equation 6.3. However, due to the large number of events associated with the ^{71}Ge EC decays, the L_2 peak, which has an energy of 1.14 keV and a relative amplitude of 0.0011, is not negligible and is included in the fit. [131]

6.1.3. Compton scattering of gamma rays

Material contamination is a significant concern in low-background experiments like CDMSlite, as even trace amounts of radioactive isotopes can introduce unwanted background events. One common contaminant is ^{238}U, which can be integrated into the detector materials during the manufacturing process. ^{238}U undergoes a series of alpha and beta decays, producing a chain of radioactive daughter isotopes that contribute to the background in the CDMSlite energy spectrum. To minimize this contamination, materials with low levels of radioactivity are carefully selected, and strict cleanliness protocols are followed during detector fabrication and assembly.

One of the key features in the CDMSlite background spectrum is the presence of "Compton steps", which are step-like structures created by the detector's collection of at least the binding energy of any freed electron during a Compton scattering event. The Monash University Compton Model [136] is used to calculate the properties of the scattered incident photon and the recoiling electron in the detector while accounting for the atomic binding energy.

As an example, when an electron from the K shell of germanium, which has a binding energy of 11.1 keV, is freed by an incident gamma, the detector collects at least this binding energy along with any additional energy transferred to the electron. Consequently, a K-shell electron in germanium can never deposit less than 11.1 keV in the detector. The relative size of the Compton steps is expected to be determined by the number of electrons in each atomic shell, but the details of the electron wave functions also play a role. While the K-shell step has been directly measured in germanium, other methods must be employed to estimate the lower energy steps [131].

The primary contributors to the Compton background in CDMSlite are radiogenic photons from trace contamination in the experimental materials, such as the shield materials (polyethylene and lead), cryostat, and towers (copper). To estimate the shape of this background component, a simulation of ^{238}U decays originating from the cryostat cans was performed with Geant4 [137]. The resulting spectrum of deposited energy in the CDMSlite detector was found to be representative of all bulk contamination. The simulated spectrum is then fit with a model consisting of a sum of error functions in Eq. 6.4 to describe the Compton background in the CDMSlite analysis.

$$f_c(E) = \Lambda_0 + \sum_{i=K,L,M,N} 0.5\Lambda_i \left(1 + \mathrm{erf}\left(\frac{E-\mu_i}{\sqrt{2}\sigma_i}\right)\right) \tag{6.4}$$

where μ_i gives the location of each step, σ_i is the energy resolution illustrated in Section 5.3, and Λ_i represents amplitudes of the error functions. Λ_0 is a constant term with a value of 0.005 keV^{-1}, accounting for a flat background required to fit the simulated spectrum. [131]

Due to the binned nature of the fit, only the amplitudes of the first four Compton steps could be reliably determined. The final parameters of the Compton background model, obtained by fitting Equation 6.4 to the Geant4 simulation, are presented in Table 6.2 and shown in Figure 6.1.

	Λ_K	Λ_L	Λ_M	Λ_N
Isotope	5.7 ± 0.3	15.2 ± 0.5	9.43 ± 1.40	18.7 ± 1.3

Table 6.2: Amplitudes of the error functions, normalized over the energy range of 0-20 keV. All values have been multiplied by a factor of 103 and are in units of keV^{-1}. Table taken from [131].

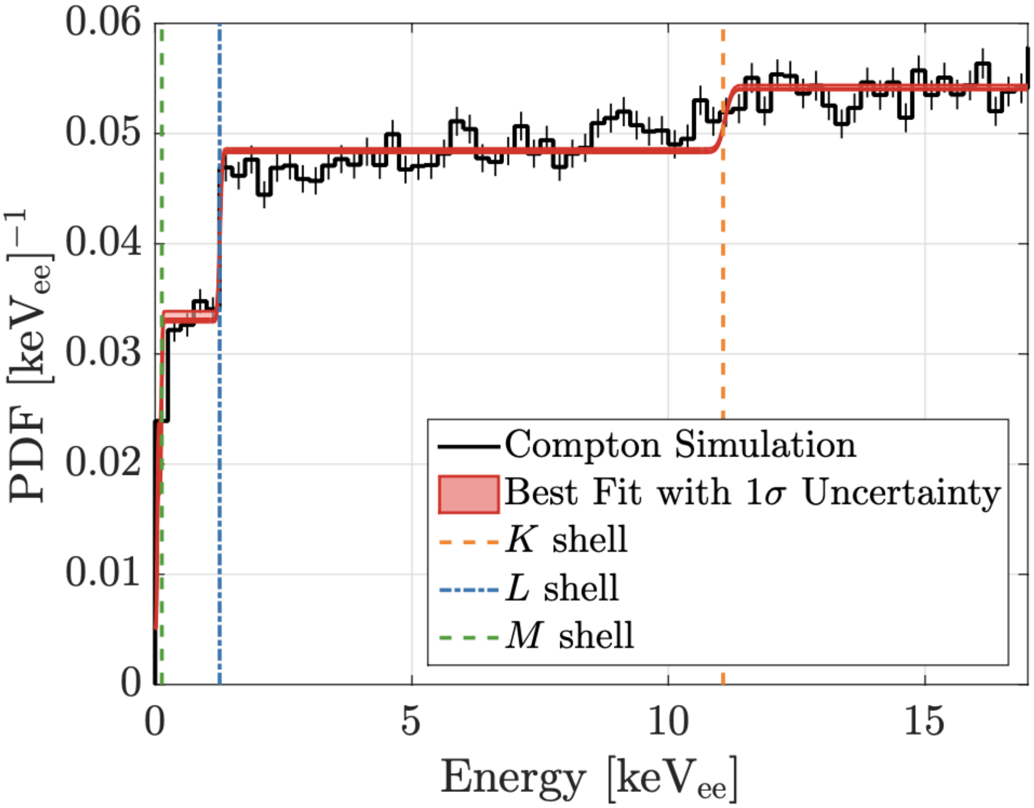

Figure 6.1: Best fit of the Compton scattering spectral model using Geant4 simulation of Compton scatters. Image taken from [131].

6.1.4. Surface background

Surface backgrounds in the CDMSlite detector arise from radioactive contamination on the detector's surface or nearby materials, with the primary contributors being ^{210}Pb, ^{40}K, and ^{14}C [118]. Among these, the decay of ^{210}Pb and its daughter isotopes, originating from radon exposure during detector production and testing, constitutes a significant background source. When ^{222}Rn decays, its long-lived daughter ^{210}Pb can plate out onto the surfaces of the detectors and their surrounding copper housings. As ^{210}Pb undergoes a multi-step decay to stable ^{206}Pb, it emits a variety of particles, including alphas, betas, Auger electrons, x-rays, a 46.5 keV gamma-ray, and the 103 keV ^{206}Pb daughter nucleus. These particles have a short mean free path in germanium and deposit most of their energy within a few millimeters of the detector's surface, resulting in near-surface recoil events that can mimic dark matter signals [131].

To model and understand the surface background components, simulations using Geant4 [137] were employed combined with a detector response function. The simulation tracks the energy deposition of the various particles emitted in the radioactive decays, particularly focusing on the ^{210}Pb decay chain, and predicts their expected energy distribution in the detector. The simulated surface background rate is then normalized using data from a study of alpha events, which provide an independent measure of the contamination levels.

To accurately model surface events in the CDMSlite detector, it is important to consider the limited penetration depth of the particles and the impact of the asymmetric electric field on their NTL gain. Due to the asymmetric electric field, surface events occurring at large radii may experience reduced NTL gain, leading to their removal by the fiducial volume cut. To properly account for this effect in the CDMSlite background model, an approximation of the detector response is necessary to ensure that reduced NTL events are appropriately removed.

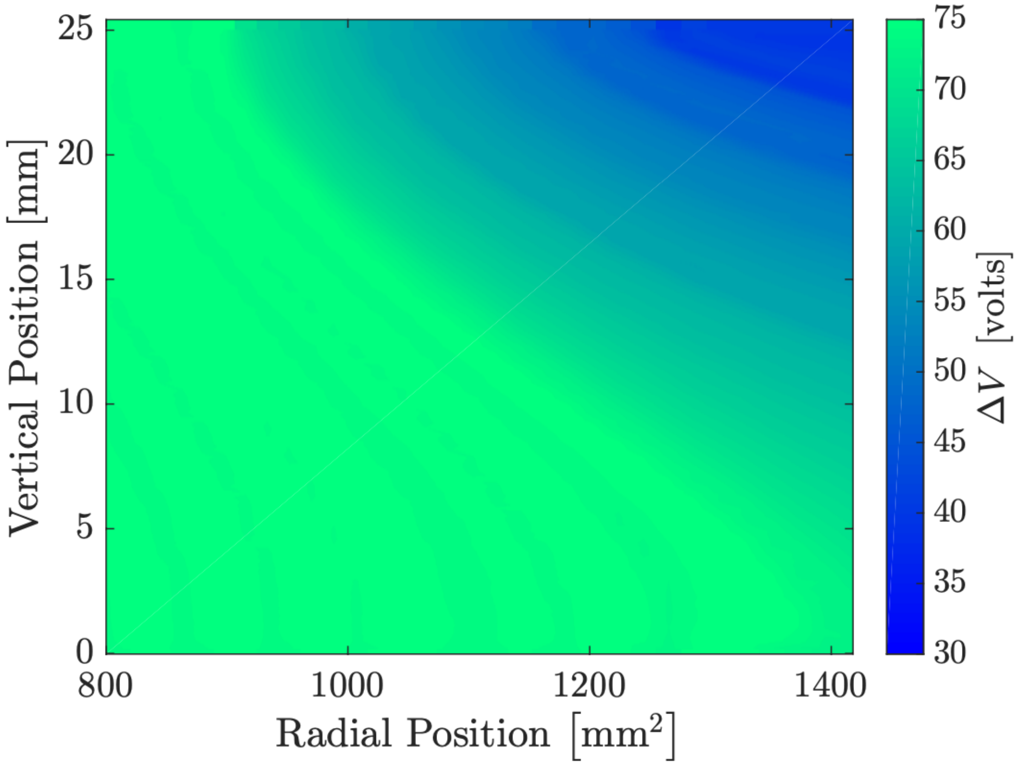

Figure 6.2: Calculated voltage map for high radius events, showing the difference in electric potential between the final collection points of the positive and negative charge carriers, as a function of initial position of the pair (plotted as radius squared vs. vertical position). The top of the crystal is biased at +75V and the bottom is grounded. Charge carriers in the outermost (radius $>$ 800 mm^2) detector annulus can experience less than the full detector bias voltage. Image Taken from [131].

.

The detector response model incorporates the voltage map shown in Figure 6.2 and the resolution model described in Section 5.3 to estimate the total phonon energy measured in the detector. Each component of the energy resolution model is implemented independently. For instance, the energy deposited in a Geant4 simulation is used to determine the average number of electron-hole pairs produced. Then, an integer number of actual pairs is randomly drawn from a distribution with a width of σ_F. The location of the Geant4 event within the detector is used to determine the voltage difference (ΔV) experienced by the event, and the total phonon energy is calculated based on the energy deposited in the simulation.

To approximate the fiducial volume cut, a cut on the experienced ΔV of the events is employed. This cut is set at $\Delta \mathrm{V} > \mathrm{V}_{\mathrm{cut}} \approx 74$ volts, where the simulation itself used a detector voltage ($\mathrm{V}_{\mathrm{det}}$) of 75 volts. By applying this cut, events with reduced NTL gain due to their proximity to the detector surface can be effectively removed from the analysis.

6.2. Photoelectric Absorption Cross Section

As mentioned in Chapter 1, the expected cross section σ_{ae} is proportional to the photoelectric absorption cross section σ_{pe}, which depends on the detector's target material. Precise measurement of the photoelectric absorption cross section is necessary for the search of solar axions and other low-mass dark matter candidates, as some of the relevant energy range of interest for these particles lies in the low-energy regime. Photoelectric absorption cross section σ_{pe} is a measurement of the probability that a photon will be absorbed when light travels through a medium, resulting in the ejection of a photoelectron. The cross section depends on multiple factors, including the temperature, the photon energy, the target material's atomic number, and the electronic configuration of the involved atoms or molecules [138]. The cross section generally increases with the atomic number Z of the target material. This is because atoms with higher Z have more electrons and a greater probability of absorbing photons [139].

The total cross section for the interaction of photons with matter is the sum of the cross sections of three main processes: photoelectric absorption, coherent scattering (Rayleigh scattering), and incoherent scattering (Compton scattering). Each process contributes to the overall likelihood of a photon interacting with the atoms or molecules within a material. The total cross section σ_{total} of a photon traveling through a medium is the sum of these three individual cross sections

$$\sigma_{\mathrm{total}} = \sigma_{pe} + \sigma_R + \sigma_C \tag{6.5}$$

where σ_R and σ_C are the cross sections for Rayleigh and Compton scattering, respectively. The relative contributions of all the cross sections to the total cross section for Ge and Si were analyzed in [110], using data from the X-Ray Form Factor, Attenuation, and Scattering Tables (FFAST) database by the National Institute of Standards and Technology (NIST). The target materials employed in SuperCDMS detectors, are illustrated in Figure 6.3.

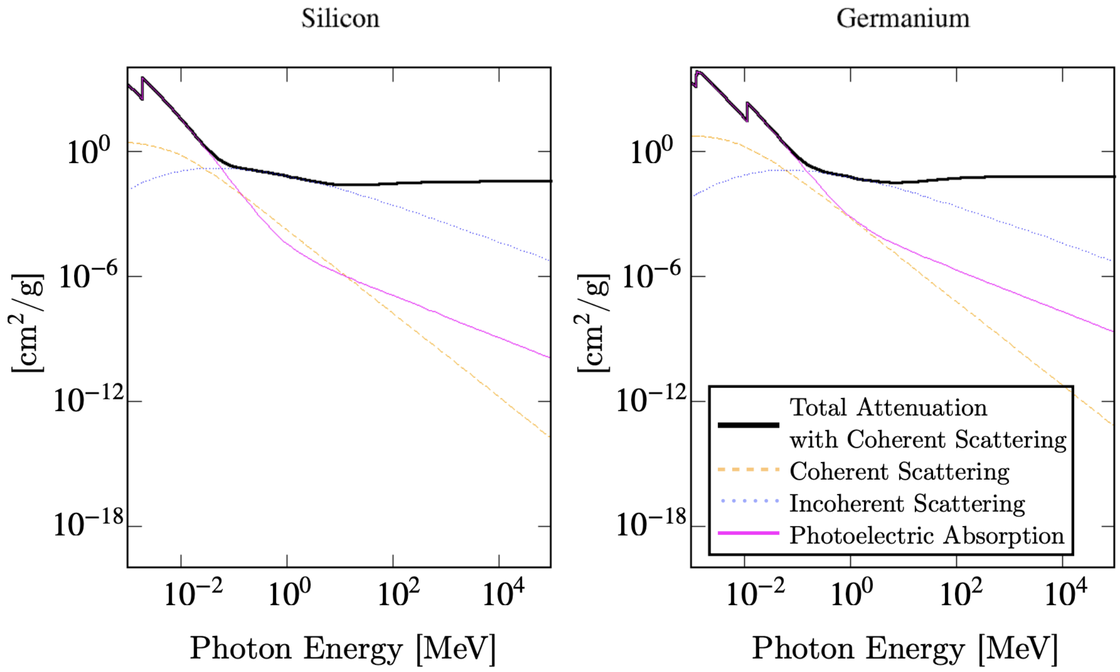

Figure 6.3: Breakdown of the total cross section for Silicon and Germanium. Data source from NIST XCOM [140]. Image taken from [110].

A comprehensive literature review was conducted in [110] to gather data on the photoelectric absorption cross section σ_{pe}. The various sources from which the σ_{pe} data were collected are summarized in Table 6.3. However, this list is not exhaustive, as the primary focus was on collecting data at low photon energies below 100 eV, where data points are scarce and discrepancies among available data are more prevalent. At higher energies, numerous additional sources of σ_{pe} data exist, but their data are consistent with other available datasets and are therefore considered redundant. Figure 6.4 presents a compilation of the σ_{pe} data collected from the sources listed in Table 6.3 for photon energies below 20 keV.

Table 6.3: List of references for the photoelectric absorption cross section σ_{pe} data obtained for Si and Ge. For each reference, the material, methodology, photon energy range, and temperature of which the data was measured/calculated are also listed. Noted that the 296 K is not explicitly specified in the cited reference, and it has been assumed that the measurements were performed at room temperature. Table taken from Ref. [110].

Source No.	Reference	Material	Method	Energy Range	Temperature
1	Ref. [141]	Si	Experimental	1–1.3 eV	4.2–415 K
2	Ref. [142]	Si	Experimental	1–3.3 eV	296 K
3	Ref. [143]	Si	Experimental	1 eV–1 keV	296 K
4	Ref. [144]	Si	Experimental	1.5–5 eV	77 K
5	Ref. [145]	Si	Experimental	$<$ 10 eV	300 K
6	Ref. [146]	Si	Experimental	$<$ 10 eV	300 K
7	Ref. [147]	Si	Experimental	25–97 eV	296 K
8	Ref. [148]	Si	Experimental	69–220 eV	296 K
9	Ref. [149]	Si	Experimental	90–210 eV	296 K
10	Ref. [150]	Si	Experimental	98–105 eV	296 K
11	Ref. [151]	Si	Experimental	99–105 eV	296 K
12	Ref. [152]	Si	Experimental	1.4–30 keV	296 K
13	Ref. [153]	Si, Ge	Experimental	1.5–6 eV	296 K
14	Ref. [154]	Si, Ge	Experimental	$<$ 10 eV	77–300 K
15	Ref. [155]	Si Ge	Theory Calculation	5 eV–433 keV 30 eV–443 keV	296 K
16	Ref. [156]	Si Ge	Theory Calculation	10–926 eV 10–487 eV	296 K
17	Ref. [157]	Ge	Semi-Empirical	10 eV–30 keV	296 K
18	Ref. [158]	Si, Ge	Experimental	20–120 eV	296 K
19	Ref. [140]	Si, Ge	Experimental	1 keV–100 GeV	296 K
20	Ref. [159]	Si, Ge	Theory/Experimental	5–25 keV	296 K
21	Ref. [160]	Si, Ge	Experimental	$<$ 1 eV	4–291 K
22	Ref. [143]	Ge	Experimental	1 eV– 1 keV	296 K
23	Ref. [161]	Ge	Experimental	1–10 eV	296 K
24	Ref. [162]	Ge	Experimental	10–25 eV	296 K
25	Ref. [163]	Ge	Experimental	15–170 eV	296 K
26	Ref. [164]	Ge	Experimental	400 eV–1.7 keV	296 K

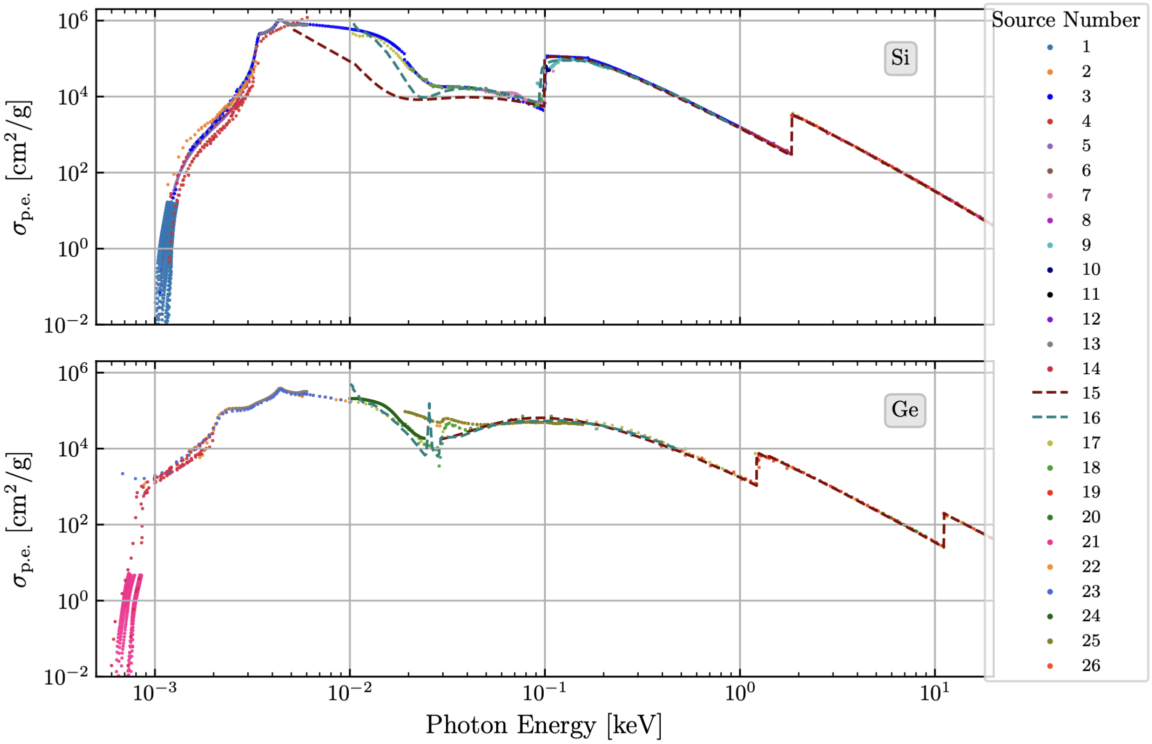

Figure 6.4: A collection of the photoelectric absorption cross section data from sources listed in Table 6.3 for Si (top) and Ge (bottom). The solid points represent experimental or semi-empirical measurements of the photoelectric absorption cross section σ_{pe}, while the dashed lines represents theoretically calculated values of σ_{pe}. Image taken from [110].

For the common axion models, the event rate is monotonously increasing with the photoelectric absorption cross section according to Equation 1.30 in Section 1.5.2. Consequently, a lower absorption curve leads to a more conservative limit on the axion parameters, as it implies a smaller expected event rate for a given set of axion properties. Conversely, a higher absorption curve results in a more aggressive limit, as it suggests a larger expected event rate, allowing for more stringent constraints on the axion parameters.

6.3. Profile Likelihood Analysis

The CDMSlite experiment's strength resides in its ability to operate at a low energy threshold, enabling the exploration of previously uncharted regions of dark matter and axions' parameter space. However, the presence of backgrounds constrains the range of cross-sections that can be investigated using the data obtained from the operations.

To effectively integrate background information when searching for a dark matter or solar axion signal, the profile likelihood ratio (PLR) method is utilized, incorporating both the signal and background components to improve the sensitivity of the experiment. By accounting for known backgrounds, the PLR approach provides enhanced sensitivity compared to the optimum interval limit-setting method employed in the Run 2 analysis [165,166]. Additionally, the PLR method can potentially be used in a discovery framework, enabling the identification of a signal. This approach also incorporates systematic uncertainties associated with signal and background models, reflecting their impact on the overall sensitivity.

6.3.1. Mathematical framework

The Poisson method is a straightforward approach to set an upper limit on a parameter of interest, such as the WIMP-nucleon spin-independent cross section σ_{WIMP} in a dark matter search, or the axio-electric cross section σ_{ae} in solar axion search. Assuming a one-dimensional theoretical energy spectrum dN/dE, the signal hypothesis can be excluded to a desired confidence level (CL.) by adjusting σ to yield the expected number of events ν satisfying

$$\alpha = e^{-\nu} \sum_{m=0}^{N} \frac{\nu^m}{m!} \tag{6.6}$$

where N is the total number of observed events. However, this method assumes all observed events are signal, leading to overly conservative upper limits when background events are present.

To address this limitation, an extended likelihood function $\mathcal{L}$ can be employed. For a set of n observed events with an expected number of events ν, the extended likelihood function is constructed by considering a generic probability density function (PDF) f. This function is obtained by taking the product of the individual probabilities for each observed event while also incorporating the Poisson probability of observing n events given the expected number ν, as shown in Equation 6.7.

$$\mathcal{L}(\theta) = \frac{e^{-\nu}\nu^n}{n!}\prod_{i=1}^{n} f(x_i;\theta)\delta x \tag{6.7}$$

In this equation, $f(x;\theta)$ is the parametric probability density with the model parameters θ. The probability of an observation $x \in x_k \pm \delta x/2$ is $f(x_k;\theta)\delta x$. Note that factoring in Poisson probabilities is important when low event rates lead to results impacted by $\sim \sqrt{n}$ fluctuations.

The likelihood function provides a more robust approach to setting upper limits on parameters of interest in dark matter searches by properly accounting for background events and statistical fluctuations, thus avoiding the overly conservative limits that can result from the simpler Poisson method.

To determine the best-fit parameters, we take the logarithmic form of the extended likelihood function given in Eq. 6.7 and drop all non-parametric constants. The resulting log-likelihood function is given by:

$$\ln \mathcal{L}(\theta) = -\nu(\theta) + \sum_{i=1}^{n} \ln(\nu(\theta) f(x_i;\theta)). \tag{6.8}$$

By maximizing this log-likelihood function $\mathcal{L}(\theta)$, the best-fit values describing the observed data can be obtained. The core principle of this Maximum Likelihood Estimation

(MLE) is to choose the parameters θ that maximize the likelihood of observing the given data. In other words, MLE aims to find the parameter values that make the observed data the most probable.

To estimate the parameters using MLE, we rely on a set of n independent and identically distributed (IID) samples $\{X_1,\, X_2,\, ...,\, X_n\}$. These samples are assumed to be drawn from the same underlying probability distribution, and the observations are assumed to be independent of each other. Finding the argmax of the log-likelihood function yields the same result as finding the argmax of the likelihood function itself. In other words, the parameter values that maximize the log-likelihood function are identical to those that maximize the original likelihood function given by

$$\hat{\theta} = \arg\max_{\theta}\ \mathcal{L}(\theta) \tag{6.9}$$

This property holds because the logarithm is a monotonically increasing function. As a result, the logarithm preserves the relative order of the likelihood values, and the location of the maximum remains unchanged when the logarithm is applied. This maximum likelihood estimation provides a systematic approach to determine the optimal parameters based on the available observations.

6.3.2. Profile likelihood ratio

The Profile Likelihood Ratio (PLR) approach is a preferred technique for experiments with well-known background distributions, as a direct result of Neyman-Pearson's lemma [167]. The lemma states that the most powerful test statistic for testing between two hypotheses, H_0 (null) and H_1 (alternate) on observed data x, comes from the likelihood ratio λ of the alternate hypothesis to the null hypothesis given by

$$\lambda = \frac{\mathcal{L}(H_1|x)}{\mathcal{L}(H_0|x)} \tag{6.10}$$

The PLR approach is affected by the presence of background events in the search region, provided that the prediction from the background model is consistent with the number of observed events. This allows experiments to loosen their cuts and enlarge their search region, increasing signal acceptance and improving detection sensitivity. Additionally, the PLR approach can easily incorporate correlations of nuisance parameters.

To further advance Eq. 6.10, consider data dependent on a parameter of interest σ and a set of nuisance parameters $\{\theta\}$, which would introduce systematic uncertainties. The PLR is used to test the compatibility of the data with a hypothesized value of σ. Reducing the number of systematic uncertainties, and thus nuisance parameters, is crucial for experiments to place stronger upper limits on the cross section. This approach involves defining a likelihood function given by

$$\mathcal{L}(\sigma, \{\theta\}|x) = f(x|\sigma, \{\theta\}) \tag{6.11}$$

where x denotes an independent, observed dataset. The likelihood function can be defined as a function of 1,2,... N dimensions, giving the PLR approach an advantage when there are N measurements of > 2 variables. This $\mathcal{L}(\sigma, \{\theta\})$ can be maximized either conditionally, by fixing σ; or unconditionally, by allowing σ to vary freely. The PLR λ is defined as the ratio of the conditional maximum likelihood estimators to the unconditional MLE, gvien by

$$\lambda = \frac{\mathcal{L}(\sigma, \{\hat{\hat{\theta}}\})}{\mathcal{L}(\hat{\sigma}, \{\hat{\theta}\})} \tag{6.12}$$

where the double hat notation $\hat{\hat{\theta}}$ denotes the MLEs when σ is fixed using the test value, and the single hat notation $\hat{\theta}$ denotes the MLEs when σ is free and able to converge at the MLE of $\hat{\sigma}$. To present a result that only depends only σ, the nuisance parameters must be "profiled-out" with the systematic uncertainties, which is accounted for in the definition of λ.

A test statistic q based on the profile likelihood is defined differently for exclusion curves (upper limits) and discovery calculations:

$$q = \begin{cases} -2\ln(\lambda), & \hat{\sigma} \leq \sigma \\ 0, & \hat{\sigma} > \sigma \end{cases} \tag{6.13}$$

where only cases with the MLE of $\hat{\sigma} \leq \sigma$ are considered for exclusion curves. The compatibility between the observed data and the signal hypothesis can be tested using this q-value. A value of q = 0 indicates when the MLE of the parameter $\hat{\sigma}$ is equal to the hypothesized value σ, suggesting the data is most consistent with the signal hypothesis. As the q-value increases, the discrepancy between $\hat{\sigma}$ and σ grows, indicating a decreasing compatibility between the data and the signal hypothesis. By evaluating the observed data under the signal hypothesis H_σ, the observed q-value q_{obs} leads to the signal p-value p_s, which is given by

$$p_s = \int_{q_{\text{obs}}}^{\infty} f(q|H_\sigma)dq \tag{6.14}$$

where $f(q|H_\sigma)$ is the probability density function of the test statistic q under the signal hypothesis H_σ. To determine whether a signal hypothesis should be excluded, it is common to set a threshold for the p-value at 0.05, which corresponds to a confidence level of 95%. This threshold is associated with a Z-score (or standard score) of 1.64, meaning that the observed result is 1.64 standard deviations away from the mean of the distribution expected under the null hypothesis.

For the discovery of a positive signal, the test statistic q_0 is defined as

$$q_0 = \begin{cases} -2\ln(\lambda_0), & \hat{\sigma} \geq 0 \\ 0, & \hat{\sigma} < 0 \end{cases} \tag{6.15}$$

where $ln(\lambda_0)$ is defined as twice the logarithm of the ratio of these maximum likelihoods with respect to H_1 and H_0 hypotheses given by

$$q_0 = -2\ln\frac{\mathcal{L}(H_0)}{\mathcal{L}(H_1)} \tag{6.16}$$

where the parameter of interest σ is assumed to be non-negative, and an important case of the test statistic q_0 is used to test the hypothesis at $\sigma = 0$. This specific case is of great significance because rejecting the null hypothesis, effectively leads to the discovery of a new signal. A higher value of q_0 indicates a greater discrepancy between the two hypotheses, favoring the signal-plus-background hypothesis (H_1) and suggesting the potential for a discovery. According to Wilk's theorem, the test statistic q_0 follows a chi-squared distribution with two degrees of freedom (χ^2_2) in the asymptotic limit.

6.3.3. PLR on solar axion

The solar axion analysis relies on an extended likelihood function that comprises three distinct categories of terms. Notations of these terms are demonstrated in Table 6.8. The first category $\mathcal{L}_{\text{Poiss}}$ serves as an overall normalization term, allowing the total number of fitted events to vary around the observed number of events N in the dataset. This Poisson constraint is given by

$$\mathcal{L}_{poiss} = \Big[\nu_\chi + \sum_b \nu_b\Big]^N \times \frac{\exp\Big[-\Big(\nu_\chi + \sum_b \nu_b\Big)\Big]}{N!} \tag{6.17}$$

The second category forms the core of the likelihood function and includes signal and background probability density functions to estimate the most probable signal and background rates. Note that for the PLR analysis of CDMSlite Run 3, separate PDFs are used for Period 1 and Period 2, denoted as $\mathcal{L}^{R3a}_{\chi,b,sb}$ and $\mathcal{L}^{R3b}_{\chi,b,sb}$, where bb and sb denotes the bulk background and the surface background respectively. The general form of this likelihood function is given by

$$\mathcal{L}_{\chi,b} = \prod_{i=1}^{N}\Big[f_\chi(E_i) + \sum_b f_b(E_i)\Big] \tag{6.18}$$

The third category constrains the nuisance parameters by incorporating auxiliary measurements. This analysis incorporates three major terms: the morphed surface backgrounds, the morphed efficiency, the resolution model. The constraint terms are modeled using either a univariate Gaussian PDF for efficiency and yield or multivariate Gaussian distribution for surface backgrounds and resolution. To implement a multivariate constraint, a covariance matrix is derived from the normalization uncertainty of the individual components and the correlations between them. This constraint term of the likelihood function is given by

$$\begin{aligned}\mathcal{L}_{constr.} &= \frac{1}{\sqrt{2\pi\sigma_k^2}} \times \exp\left(-\frac{(x_k-\mu_k)^2}{2\sigma_k^2}\right)\\ &= \frac{1}{(2\pi)^{d/2}|\boldsymbol{V}|^{1/2}} \times \exp\left(-\frac{1}{2}(x_k-\mu_k)^T\boldsymbol{V}^{-1}(x_k-\mu_k)\right)\end{aligned} \tag{6.19}$$

Taking the logarithm of the likelihood function is a common practice, as it simplifies the computations. Additionally, any constant terms can be omitted, as they will cancel out when taking the ratio of likelihoods, and only the changes in likelihood are relevant. The first two likelihood terms that can be combined after taking the logarithm and are given by:

$$\begin{aligned}\left[\ln(\mathcal{L}^{R3}_{poiss}) + \ln(\mathcal{L}^{R3a}_{\chi,b,sb}) + \ln(\mathcal{L}^{R3b}_{\chi,b,sb})\right] &= -(\nu^{R3}_{\chi} + \sum_{b}\nu^{R3}_{b} + \sum_{sb}\nu^{R3}_{sb}) \\ &+ \sum_{i=1}^{N^{R3a}} \ln\left[\nu^{R3}_{\chi} f^{R3a}_{\chi}(E_i) + \sum_{b}\nu^{R3}_{b} f^{R3a}_{b}(E_i) + \sum_{sb}\rho^{R3a}_{sb}(E_i)\right] \\ &+ \sum_{i=1}^{N^{R3b}} \ln\left[\nu^{R3}_{\chi} f^{R3b}_{\chi}(E_i) + \sum_{b}\nu^{R3}_{b} f^{R3b}_{b}(E_i) + \sum_{sb}\rho^{R3b}_{sb}(E_i)\right]\end{aligned} \tag{6.20}$$

The full likelihood function with the constraint term used for the limit setting is given by

$$\begin{aligned}&\left[\ln(\mathcal{L}^{R3}_{poiss}) + \ln(\mathcal{L}^{R3a}_{\chi,b,sb}) + \ln(\mathcal{L}^{R3b}_{\chi,b,sb})\right] + \ln(\mathcal{L}^{R3}_{surf}) + \ln(\mathcal{L}^{R3a}_{res}) + \ln(\mathcal{L}^{R3b}_{res}) + \ln(\mathcal{L}^{R3a}_{eff}) + \ln(\mathcal{L}^{R3b}_{eff}) \\ &= -(\nu^{R3}_{\chi} + \sum_{b}\nu^{R3}_{b} + \sum_{sb}\nu^{R3}_{sb}) + \sum_{i=1}^{N^{R3a}} \ln\left[\nu^{R3}_{\chi} f^{R3a}_{\chi}(E_i) + \sum_{b}\nu^{R3}_{b} f^{R3a}_{b}(E_i) + \sum_{sb}\rho^{R3a}_{sb}(E_i)\right] \\ &\qquad + \sum_{i=1}^{N^{R3b}} \ln\left[\nu^{R3}_{\chi} f^{R3b}_{\chi}(E_i) + \sum_{b}\nu^{R3}_{b} f^{R3b}_{b}(E_i) + \sum_{sb}\rho^{R3b}_{sb}(E_i)\right] \\ &\qquad -\frac{1}{2}\sum_{k=1}^{3}\left[(s^{R3}_{k} - \mu^{R3}_{k})^{T}\boldsymbol{S}^{-1}_{R3}(s^{R3}_{k} - \mu^{R3}_{k})\right] - \frac{1}{2}\sum_{k=1}^{3}\left[(r^{R3a}_{k} - \mu^{R3a}_{k})^{T}\boldsymbol{R}^{-1}_{R3a}(r^{R3a}_{k} - \mu^{R3a}_{k})\right] \\ &\qquad -\frac{1}{2}\sum_{k=1}^{3}\left[(r^{R3b}_{k} - \mu^{R3b}_{k})^{T}\boldsymbol{R}^{-1}_{R3b}(r^{R3b}_{k} - \mu^{R3b}_{k})\right] - \frac{(\Xi^{R3a} - \mu^{R3a})^{2}}{2(\sigma^{R3a}_{\Xi})^{2}} - \frac{(\Xi^{R3b} - \mu^{R3b})^{2}}{2(\sigma^{R3b}_{\Xi})^{2}}\end{aligned} \tag{6.21}$$

Variable	Definition	State
$R3a$	data period 1	Identifier
$R3b$	data period 2	Identifier
n	iterator over N events	Iterator
bb	bulk background iterator	Iterator
sb	surface background iterator	Iterator
i, j	general nuisance iterators	Iterator
ν_x	number of signal events	Free
ν_{bb}	number of events in bb	Free
ν_{sb}	number of events in sb	Constrained
s	surface bg morphing parameter	Constrained
Σ	efficiency morphing parameter	Constrained
r	resolution nuisance parameter	Constrained
N	number of events in data	Constant
E_n	energy of event n	Constant
μ_s	expected value of s	Constant
μ_Σ	expected value of Σ	Constant
μ_r	expected value of r	Constant
σ_Σ	uncertainty of Σ	Constant
$\mathbf{S}$	surface bg covariance matrix	Constant
$\mathbf{R}$	resolution covariance matrix	Constant
f_x	signal PDF	Function
f_{bb}	PDF of bb	Function
ρ_{sb}	event density function of sb	Function

Table 6.4: Variable definitions and states used in the profile likelihood analysis. Table taken from [168].

To assess the significance of a potential WIMP or axion signal, two hypotheses are considered: the H_1 hypothesis and the H_0 hypothesis. The H_1 hypothesis assumes the presence of a signal and the null or H_0 hypothesis assumes no signal is present. In the H_1 hypothesis, we maximize the extended likelihood function given in Eq. 6.7 to obtain the best-fit parameters for the WIMP or solar axion signal component. Conversely, in the H_0 hypothesis, we maximize Eq. 6.7 under the assumption that no signal component exists.

To calculate an upper limit on the number of signal events, a modified approach is employed. When the number of signal events being tested is smaller than the best-fit value obtained from the likelihood maximization, the test statistic q is set to zero, which ensures that statistical fluctuations do not artificially lower the upper limit below the true number of signal events. The maximization of the log-likelihood function was performed using the MINUIT algorithm [169] through the Python interface provided by the iminuit package [170]. Figure 6.5 gives an example of the PLR scan on solar axion mass $m_a \approx 0.16\,\mathrm{keV/c^2}$ and $\sigma_{ae} = 1 \times 10^{-11}\mathrm{cm}^2$.

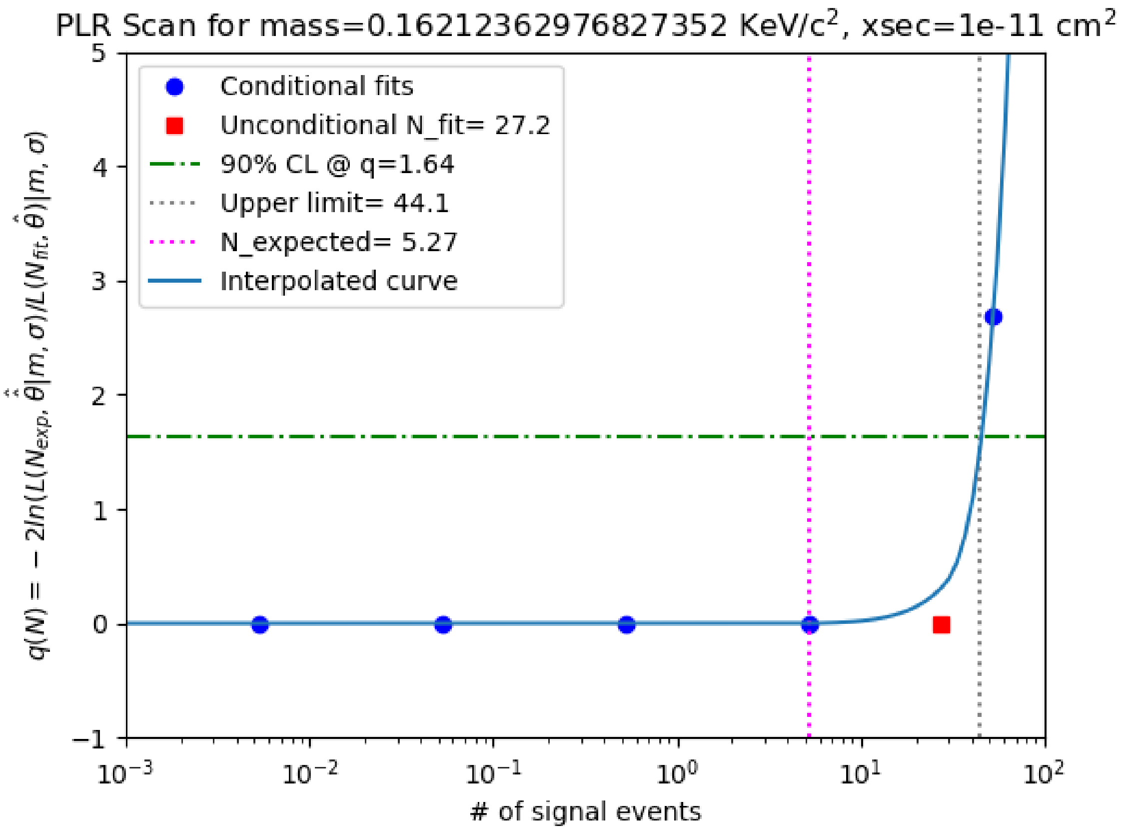

Figure 6.5: Example plot of a profile likelihood ratio scan for mass $m_a \approx 0.16\,\mathrm{keV/c^2}$ and $\sigma_{ae} = 1 \times 10^{-11}\mathrm{cm}^2$ with both conditional and unconditional fits. The green horizontal line indicates the 90% confidence level at q = 1.64, and the interpolated curve intersects and created the upper limit at 44.1 signal events. The purple vertical line shows the expected number of signal events N˙expected = 5.27 under q = 0.

.

6.4. Analysis Result

The solar axion flux results from Redondo [71] were employed as the total flux arriving at Earth from the Sun, primarily originating from the ABC reactions occurring in the solar core. Since the released data from Redondo only included energy levels above ∼ 10 eV, zero flux was assumed conservatively below this energy range shown in Figure 6.6.

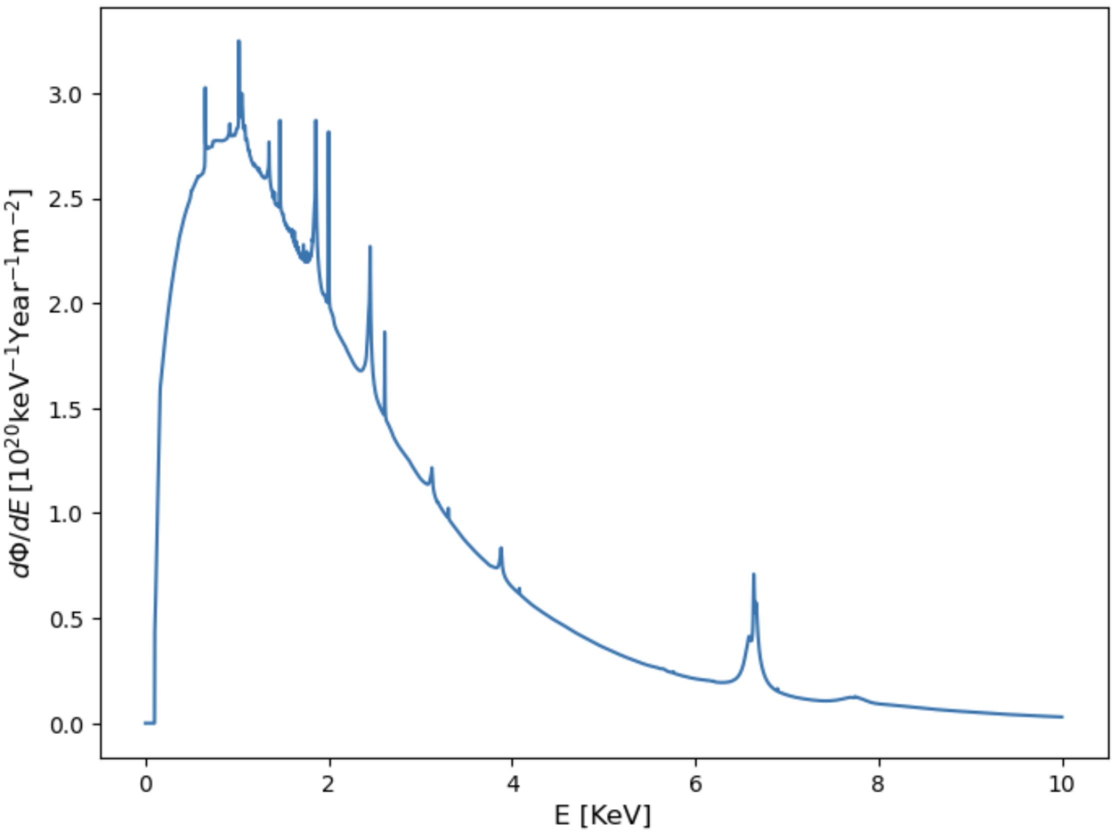

Figure 6.6: Solar axion flux results from Redondo [71] with linear interpolation. Note that flux was assumed to be zero for energy lower than ∼ 10 eV.

Upon reaching the Earth-based detector, the axio-electric effect was employed for axion detection through electron recoil. The photo-electric absorption cross-section in Figure 6.7 was utilized to estimate the anticipated axion event rates from the ABC process production in the germanium detector, which allows for a direct comparison between the predicted axion interactions and the observed experimental data. The uncertainty is a statistical combination of the analysis results from [110] and the dataset from NIST [140] for germanium material.

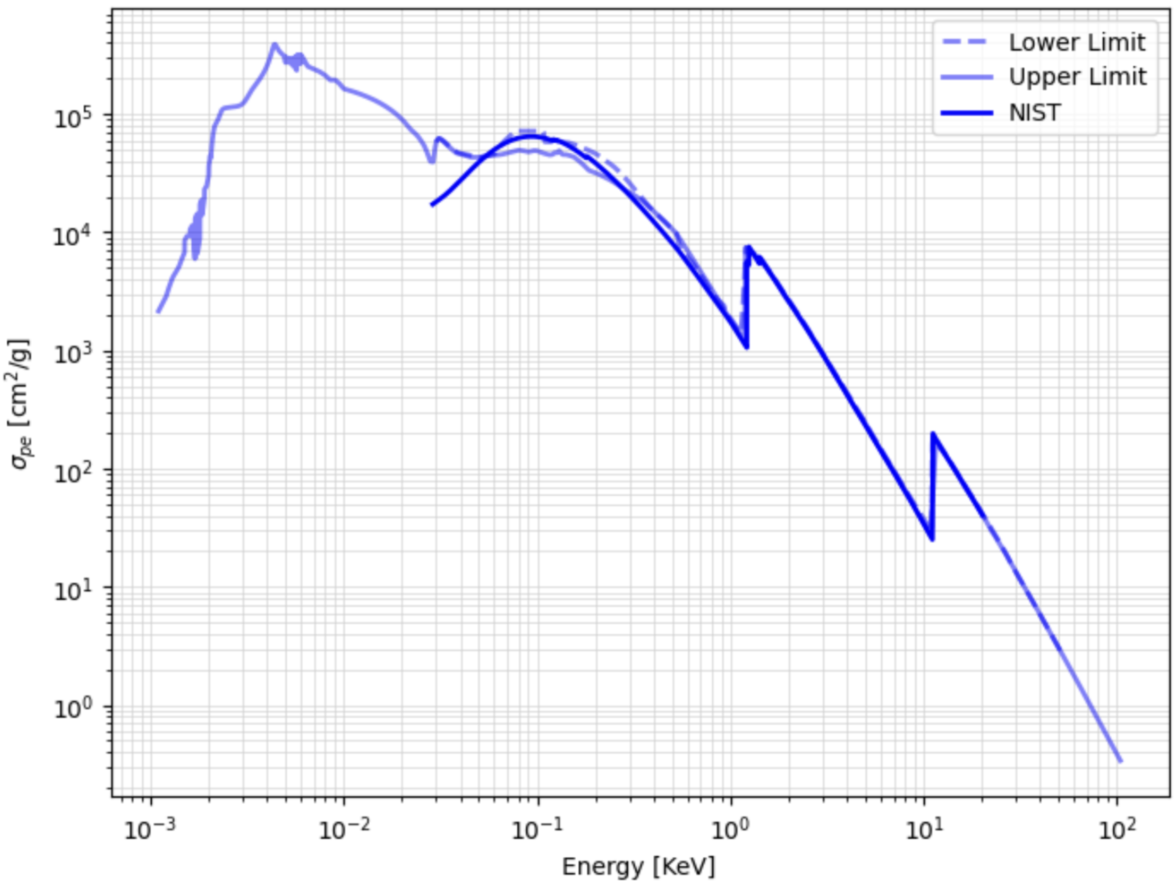

Figure 6.7: Photoelectric absorption cross section from a calculation by Wilson [110] and data from NIST [140] website for germanium.

An axion with energy E_a interacting with a SuperCDMS germanium detector via the axio-electric effect will cause an electron to recoil with approximately the same energy, creating a detectable signal. The axio-electric cross-section depending the axion energy has been calculated for various example axion masses, as depicted in Figure 6.8. This result aligns with calculation in EDELWEISS-II experiment [76] in barn per atom with $g_{ae} = 1$ for normalization.

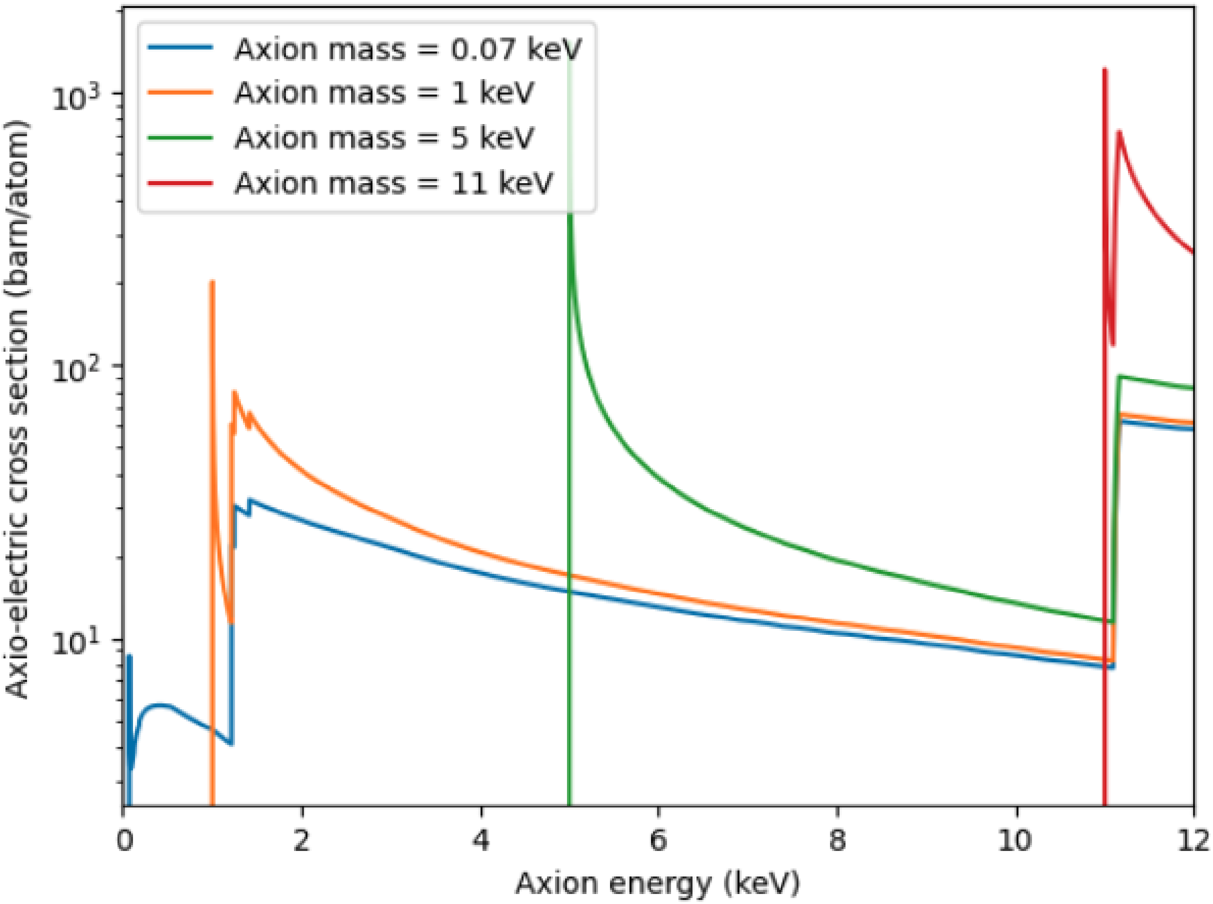

Figure 6.8: Axio-electric cross section for germanium at various axion masses, normalized with the axion-electron coupling constant σ_{ae} set to 1. Discontinuities in the cross section are evident around 1.4 keV and 11.1 keV, corresponding to electron shell transition energies.

Applying the limit setting method mentioned in the previous sections, Figure 6.9 presents the constraints on solar axion particles calculated from the profile likelihood ratio method with CDMSlite Run 3 data. A series of calculations were performed for more than 50 different axion masses, logarithmically distributed between 0.001 keV and 12 keV, using a fixed cross-section σ_{ae} of $1 \times 10^{-11}\text{cm}^2$.

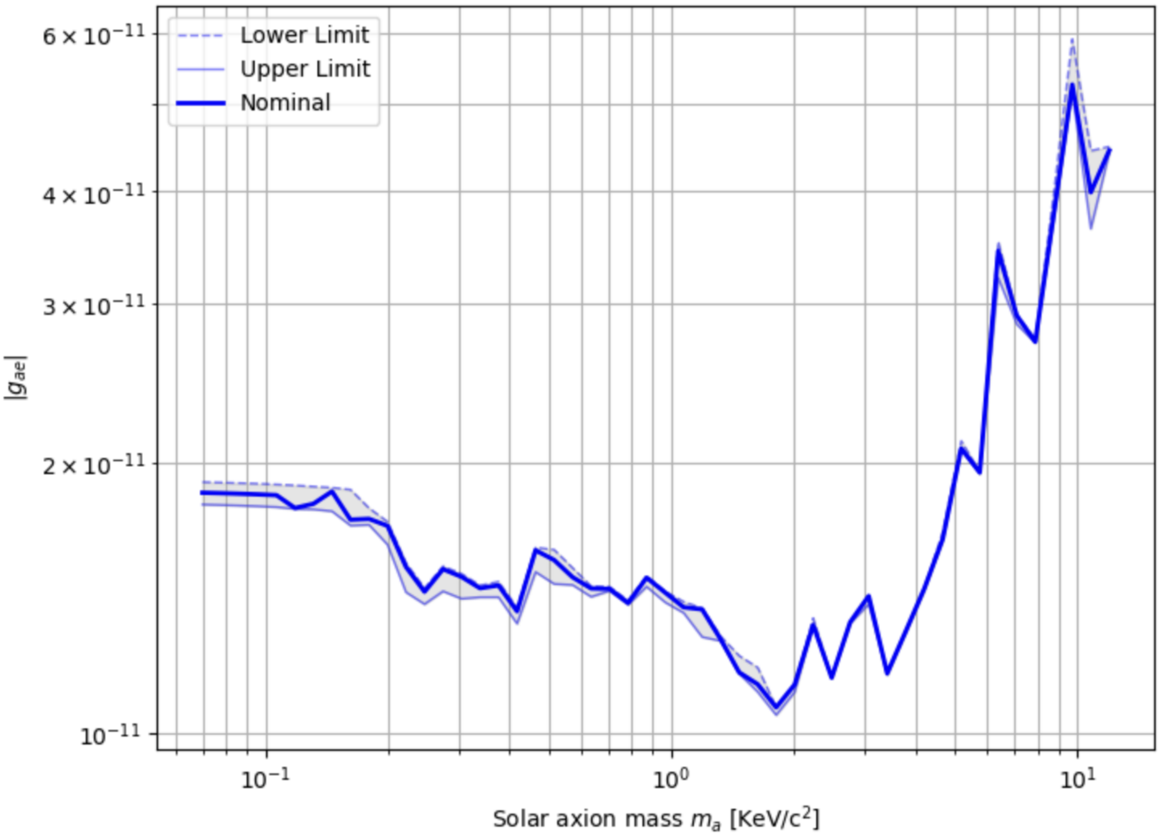

Figure 6.9: The CDMSLite-Run3 90% C.L. limit on axio-electric coupling as a function of axion mass. The shaded area represents the uncertainties originated from the photoelectric absorption in germanium detectors.

In Figure 6.9, the limit on the axio-electric coupling is displayed as a function of the axion mass of interest. Each coupling constant σ_{ae} at an individual mass was calculated using the profile likelihood ratio method with a 90% confidence level. The shaded area indicates the uncertainties from photoelectric absorption mentioned in Section 6.2. This uncertainty is a statistical combination of the analysis results from [110] and the dataset from NIST [140] for germanium material.

The constraints on axion-electron coupling constant from this work are compared with those from other underground search experiments, including both solar axions and axion-like particles. The latest astrophysical bounds from the Particle Data Group (PDG) [69] are also included. The combined results are presented in Figure 6.10.

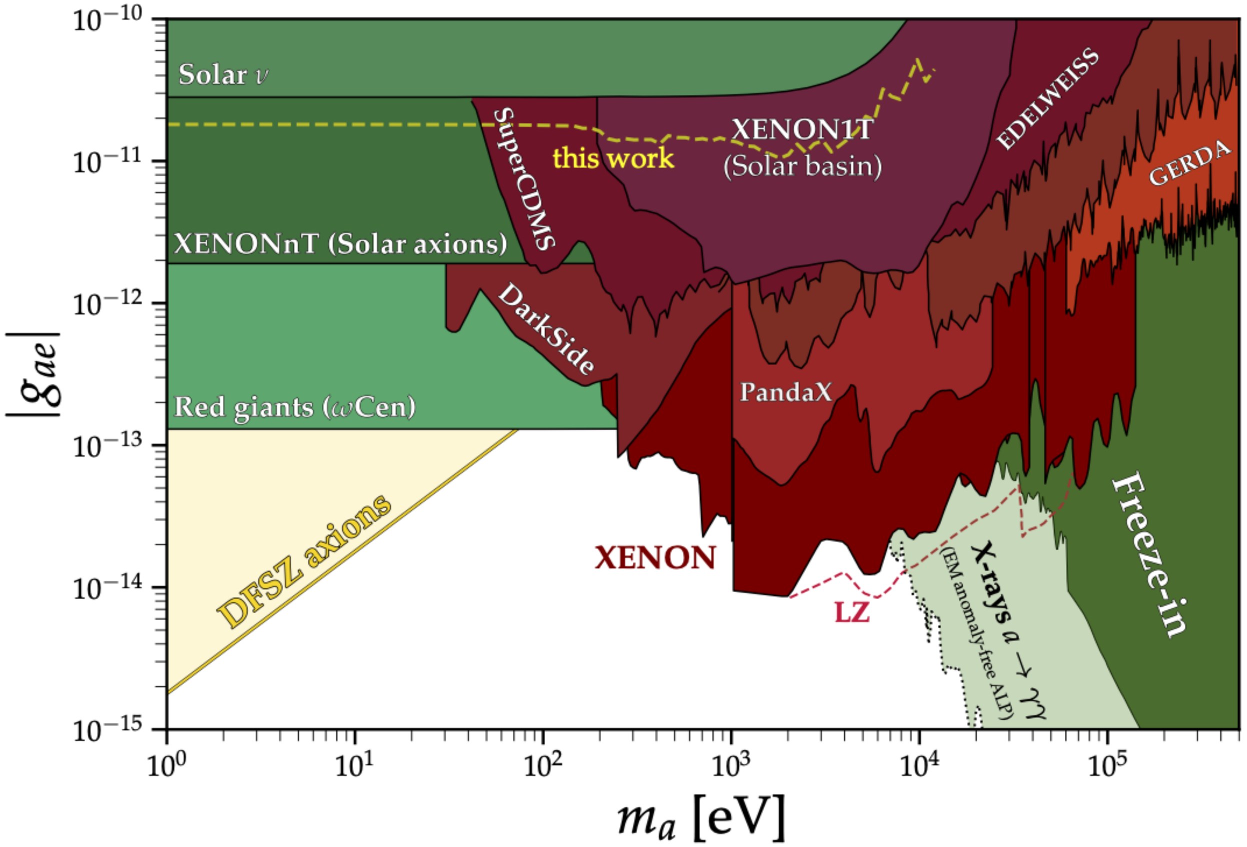

Figure 6.10: Comparison of constraints on axion-electron coupling between this work, other experiments, and astrophysical bounds. Results other than this work is taken from [69].

Chapter 7

Conclusion

Numerous observational pieces of evidence have indicated the existence of non-baryonic dark matter. Despite extensive efforts from various experiments and different detection strategies, the nature of dark matter remains a mystery, and no identification of dark matter has yet been achieved. Since the search for some dark matter candidates, such as weakly interacting massive particles and axions, has yet to yield a discovery, attention is shifting toward exploring alternative candidates and their possible interaction mechanisms, including the couplings of axions to electrons. The detection of solar axions within the parameters set by experimental data would offer compelling evidence for the existence of particles beyond the Standard Model.

The main focus of this thesis is to investigate the constraints of solar axions and particularly their interactions with electrons in the non-hadronic models. While the constraints derived for the axio-electric coupling constant in this work may not surpass those established by other underground experiments or astrophysical bounds, the calculation of these constraints for solar axions holds significant importance. By focusing on solar axions, this work fills a necessary gap in our understanding of these elusive particles and their interactions with electrons with data collected from the SuperCDMS experiments.

The solar axion search conducted in this study differs largely from previous SuperCDMS searches [46] for ALP dark matter. While ALP dark matter searches have focused on detecting ALPs that constitute dark matter in the galactic halo, the solar axion search makes no assumptions about axions being the dominant component of dark matter or about the local dark matter density. Instead, solar axions produced in the core of the Sun through the ABC reactions were studied, and they are independent of their contribution to dark matter. This work extends the constraints to axion masses below 70 eV, surpassing previous investigations [46] by the SuperCDMS collaboration regarding ALP-electron coupling. This expansion of the explored parameter space probes a region that has been less extensively studied in the context of solar axions. By exploring this lower mass range, this thesis work opens up new possibilities for discovering axion signals that may have been overlooked in prior analyses. This approach allows us to probe a wider range of axion parameter space and to set constraints on axion couplings to electron without relying on assumptions about the nature of dark matter, which provides a complementary probe of axion physics that is less dependent on the specific properties of dark matter.

The upcoming generation of SuperCDMS experiments is being developed at SNOLAB in Canada. Enhanced HV detectors will extend the sensitivity for WIMPs search to lower masses and significantly broaden the range in cross-section and coupling parameters for various channels. In anticipation of the SNOLAB commissioning, operational and analytical preparations are underway. Furthermore, using the solar axion model mentioned previously, we have projected the sensitivity of the axio-electric coupling using simulation developed for SNOLAB experiments. The projection in Figure 7.1 indicates improved sensitivity compared to the outcomes derived from CDMSlite Run3 data in certain mass region.

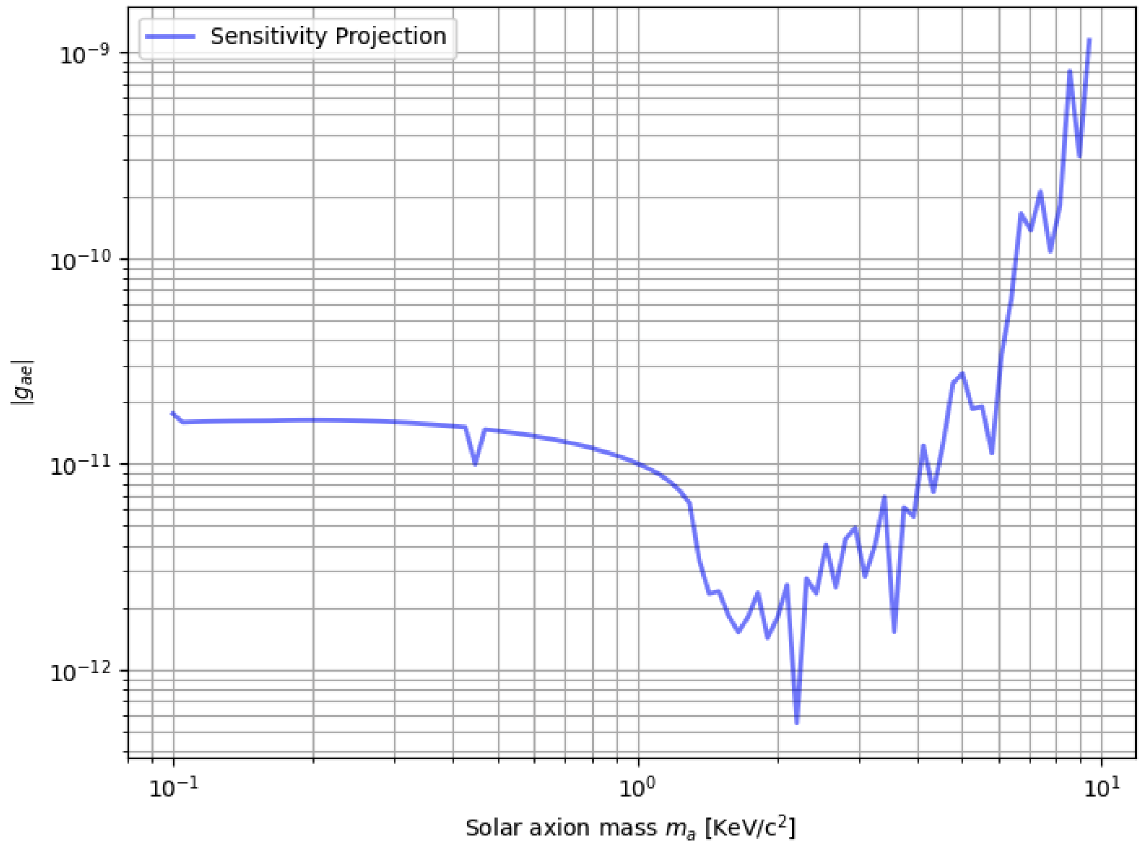

Figure 7.1: Sensitivity projection of axio-electric coupling on SNOLAB Experiments.

In conclusion, the study of solar axions is necessary in advancing the fields of particle physics, astrophysics, and cosmology. The work of this thesis established constraints on axion-electron coupling parameters that have not been previously probed by the SuperCDMS collaboration. Building on this work, the next generation of SuperCDMS experiments at SNOLAB could push the boundaries of sensitivity even further, enabling the exploration the parameter space of solar axions with higher precision. The potential discovery of solar axions would have relevance in addressing the mysteries of dark matter and the strong CP problem. The detection of solar axions could serve as compelling evidence for the existence of particles beyond the Standard Model, with significant implications for solar physics and stellar evolution.

BIBLIOGRAPHY

[1] N. Aghanim, Y. Akrami, M. Ashdown, J. Aumont, C. Baccigalupi, M. Ballardini et al., *Planck2018 results: Vi. cosmological parameters*, *Astronomy &; Astrophysics* **641** (Sept., 2020) A6. xiii, 1, 14, 15, 16, 18, 21

[2] H. Andernach and F. Zwicky, *English and spanish translation of zwicky's (1933) the redshift of extragalactic nebulae*, 2017. 3, 4

[3] R. Massey, T. Kitching and J. Richard, *The dark matter of gravitational lensing*, *Reports on Progress in Physics* **73** (July, 2010) 086901. 4

[4] V. C. Rubin and J. Ford, W. Kent, *Rotation of the Andromeda Nebula from a Spectroscopic Survey of Emission Regions*, ApJ **159** (Feb., 1970) 379. 5

[5] V. C. Rubin, W. K. Ford, Jr. and N. Thonnard, *Extended rotation curves of high-luminosity spiral galaxies. IV. Systematic dynamical properties, Sa through Sc*, *Astrophys. J. Lett.* **225** (1978) L107–L111. 5

[6] V. C. Rubin, J. Ford, W. K. and N. Thonnard, *Rotational properties of 21 SC galaxies with a large range of luminosities and radii, from NGC 4605 (R=4kpc) to UGC 2885 (R=122kpc)*, ApJ **238** (June, 1980) 471–487. 5, 6

[7] K. G. Begeman, A. H. Broeils and R. H. Sanders, *Extended rotation curves of spiral galaxies: Dark haloes and modified dynamics*, *Mon. Not. Roy. Astron. Soc.* **249** (1991) 523. 7

[8] D. Clowe, M. Bradač, A. H. Gonzalez, M. Markevitch, S. W. Randall, C. Jones et al., *A direct empirical proof of the existence of dark matter*, *The Astrophysical Journal* **648** (Aug., 2006) L109–L113. 8, 10, 11

[9] M. Bartelmann and P. Schneider, *Weak gravitational lensing*, *Physics Reports* **340** (Jan., 2001) 291–472. 8

[10] M. Markevitch, A. H. Gonzalez, D. Clowe, A. Vikhlinin, W. Forman, C. Jones et al., *Direct constraints on the dark matter self-interaction cross section from the merging galaxy cluster 1e 0657–56*, *The Astrophysical Journal* **606** (May, 2004) 819–824. 9

[11] NASA, *Astronomy Picture of the Day: The Matter of the Bullet Cluster*, 2017. 10

[12] S. W. Randall, M. Markevitch, D. Clowe, A. H. Gonzalez and M. Bradač, *Constraints on the self-interaction cross section of dark matter from numerical simulations of the merging galaxy cluster 1e 0657–56*, *The Astrophysical Journal* **679** (June, 2008) 1173–1180. 11, 12

[13] P. A. R. Ade, N. Aghanim, M. Arnaud, M. Ashdown, J. Aumont, C. Baccigalupi et al., *Planck2015 results: Xiii. cosmological parameters*, *Astronomy &; Astrophysics* **594** (Sept., 2016) A13. 12

[14] E. W. Kolb and M. S. Turner, *The Early Universe*, vol. 69. Westview Press, 1990, 10.1201/9780429492860. 12

[15] S. Dodelson, *Modern Cosmology*. Academic Press, Amsterdam, 2003. 13, 15

[16] O. Lahav and A. R. Liddle, *The cosmological parameters (2023)*, 2024. 14

[17] D. J. Fixsen, *The temperature of the cosmic microwave background*, *The Astrophysical Journal* **707** (Nov., 2009) 916–920. 14

[18] G. F. Smoot, C. L. Bennett, A. Kogut, E. L. Wright, J. Aymon, N. W. Boggess et al., *Structure in the cobe differential microwave radiometer first-year maps*, *Astrophysical Journal* **396** (9, 1992) . 14

[19] W. Hu and S. Dodelson, *Cosmic microwave background anisotropies*, *Annual Review of Astronomy and Astrophysics* **40** (2002) 171–216. 14, 15

[20] N. W. Halverson, E. M. Leitch, C. Pryke, J. Kovac, J. E. Carlstrom, W. L. Holzapfel et al., *Degree angular scale interferometer first results: A measurement of the cosmic microwave background angular power spectrum*, *The Astrophysical Journal* **568** (Mar., 2002) 38–45. 16

[21] W. Hu and N. Sugiyama, *Toward understanding cmb anisotropies and their implications*, *Physical Review D* **51** (Mar., 1995) 2599–2630. 16

[22] PARTICLE DATA GROUP collaboration, R. L. Workman et al., *Review of Particle Physics*, *PTEP* **2022** (2022) 083C01. 17, 36

[23] B. D. Fields, K. A. Olive, T.-H. Yeh and C. Young, *Big-bang nucleosynthesis after planck*, *Journal of Cosmology and Astroparticle Physics* **2020** (mar, 2020) 010. 17

[24] S. Alam, M. Aubert, S. Avila, C. Balland, J. E. Bautista, M. A. Bershady et al., *Completed sdss-iv extended baryon oscillation spectroscopic survey: Cosmological implications from two decades of spectroscopic surveys at the apache point observatory*, *Physical Review D* **103** (Apr., 2021) . 18

[25] A. G. Riess, A. V. Filippenko, P. Challis, A. Clocchiatti, A. Diercks, P. M. Garnavich et al., *Observational evidence from supernovae for an accelerating universe and a cosmological constant*, *The Astronomical Journal* **116** (Sept., 1998) 1009–1038. 19

[26] S. Perlmutter, G. Aldering, G. Goldhaber, R. A. Knop, P. Nugent, P. G. Castro et al., *Measurements of* Ω *and* Λ *from 42 high-redshift supernovae*, *The Astrophysical Journal* **517** (June, 1999) 565–586. 19

[27] M. Milgrom, *A modification of the Newtonian dynamics as a possible alternative to the hidden mass hypothesis.*, ApJ **270** (July, 1983) 365–370. 19

[28] J. Bekenstein and M. Milgrom, *Does the missing mass problem signal the breakdown of Newtonian gravity?*, ApJ **286** (Nov., 1984) 7–14. 20

[29] S. DODELSON, *The real problem with mond*, International Journal of Modern Physics D **20** (Dec., 2011) 2749–2753. 20

[30] P. Tisserand, L. Le Guillou, C. Afonso, J. N. Albert, J. Andersen, R. Ansari et al., *Limits on the macho content of the galactic halo from the eros-2 survey of the magellanic clouds*, Astronomy &; Astrophysics **469** (Apr., 2007) 387–404. 22

[31] T. D. Brandt, *Constraints on macho dark matter from compact stellar systems in ultra-faint dwarf galaxies*, The Astrophysical Journal Letters **824** (June, 2016) L31. 22

[32] S. Bird, A. Albert, W. Dawson, Y. Ali-Haïmoud, A. Coogan, A. Drlica-Wagner et al., *Snowmass2021 cosmic frontier white paper: Primordial black hole dark matter*, Physics of the Dark Universe **41** (Aug., 2023) 101231. 23

[33] M. Kamionkowski, *Wimp and axion dark matter*, 1997. 23, 25

[34] K. GRIEST, *The search for the dark matter: Wimps and machos*, Annals of the New York Academy of Sciences **688** (June, 1993) 390–407. 23

[35] D. Alp and S. Modée, *Dark matter: Particle evolution through freeze-out*, 2014. 24

[36] L. Roszkowski, E. M. Sessolo and S. Trojanowski, *Wimp dark matter candidates and searches—current status and future prospects*, Reports on Progress in Physics **81** (may, 2018) 066201. 25, 45

[37] ATLAS collaboration, G. Aad et al., *Search for new phenomena with top quark pairs in final states with one lepton, jets, and missing transverse momentum in pp collisions at $\sqrt{s}$ = 13 TeV with the ATLAS detector*, JHEP **04** (2021) 174, [`2012.03799`]. 25

[38] R. D. Peccei and H. R. Quinn, *CP Conservation in the Presence of Instantons*, Phys. Rev. Lett. **38** (1977) 1440–1443. 26

[39] S. Weinberg, *A New Light Boson?*, Phys. Rev. Lett. **40** (1978) 223–226. 26, 27

[40] F. Wilczek, *Problem of Strong P and T Invariance in the Presence of Instantons*, Phys. Rev. Lett. **40** (1978) 279–282. 26

[41] C. Vafa and E. Witten, *Parity conservation in quantum chromodynamics*, Phys. Rev. Lett. **53** (Aug, 1984) 535–536. 26

[42] G. G. Raffelt, *The nature of dark matter*, 1995. 27

[43] G. G. Raffelt, *Astrophysical methods to constrain axions and other novel particle phenomena*, Physics Reports **198** (1990) 1–113. 27

[44] P. Sikivie, *Invisible axion search methods*, Reviews of Modern Physics **93** (Feb., 2021) . 27, 28

[45] A. Derevianko, V. Dzuba, V. Flambaum and M. Pospelov, *Axio-electric effect*, Physical Review D **82** (2010) 065006. 28, 40, 50, 54

[46] T. Aralis, T. Aramaki, I. Arnquist, E. Azadbakht, W. Baker, S. Banik et al., *Constraints on dark photons and axionlike particles from the supercdms soudan experiment*, Physical Review D **101** (Mar., 2020) . 29, 30, 92, 95, 96, 97, 98, 99, 100, 101, 134, 135

[47] CDMS collaboration, Z. Ahmed et al., *Search for Axions with the CDMS Experiment*, Phys. Rev. Lett. **103** (2009) 141802, [`0902.4693`]. 30

[48] CoGeNT collaboration, C. E. Aalseth et al., *Experimental constraints on a dark matter origin for the DAMA annual modulation effect*, Phys. Rev. Lett. **101** (2008) 251301, [`0807.0879`]. 30

[49] EDELWEISS collaboration, E. Armengaud et al., *Searches for electron interactions induced by new physics in the EDELWEISS-III Germanium bolometers*, Phys. Rev. D **98** (2018) 082004, [`1808.02340`]. 30

[50] LUX collaboration, D. S. Akerib et al., *First Searches for Axions and Axionlike Particles with the LUX Experiment*, Phys. Rev. Lett. **118** (2017) 261301, [`1704.02297`]. 30

[51] PandaX collaboration, C. Fu et al., *Limits on Axion Couplings from the First 80 Days of Data of the PandaX-II Experiment*, Phys. Rev. Lett. **119** (2017) 181806, [`1707.07921`]. 30

[52] XENON100 collaboration, E. Aprile et al., *First Axion Results from the XENON100 Experiment*, Phys. Rev. D **90** (2014) 062009, [`1404.1455`]. 30

[53] XENON collaboration, E. Aprile et al., *Light Dark Matter Search with Ionization Signals in XENON1T*, Phys. Rev. Lett. **123** (2019) 251801, [`1907.11485`]. 30

[54] XMASS collaboration, K. Abe et al., *Search for dark matter in the form of hidden photons and axion-like particles in the XMASS detector*, Phys. Lett. B **787** (2018) 153–158, [`1807.08516`]. 30

[55] N. V. et al., *Phys. rev. lett.*, *Physical Review Letters* **111** (2013) 231301, [`1311.1669`]. 30

[56] M. T. P. D. Group), *Phys. rev. d*, *Physical Review D* **98** (2018) 030001. 30

[57] I. M. B. et al., *Jhep*, *Journal of High Energy Physics* **6** (2017) 87, [`1608.02123`]. 30

[58] I. G. Irastorza, *An introduction to axions and their detection*, SciPost Phys. Lect. Notes (2022) 45. 31, 34

[59] M. M. Bertolami, B. Melendez, L. Althaus and J. Isern, *Revisiting the axion bounds from the galactic white dwarf luminosity function*, Journal of Cosmology and Astroparticle Physics **2014** (Oct., 2014) 069–069. 32

[60] J. Isern, E. García-Berro, S. Torres, R. Cojocaru and S. Catalán, *Axions and the luminosity function of white dwarfs: the thin and thick discs, and the halo*, Monthly Notices of the Royal Astronomical Society **478** (May, 2018) 2569–2575. 32

[61] N. Viaux, M. Catelan, P. B. Stetson, G. G. Raffelt, J. Redondo, A. A. R. Valcarce et al., *Neutrino and axion bounds from the globular cluster m5 (ngc 5904)*, Physical Review Letters **111** (Dec., 2013) . 32

[62] O. Straniero, I. Dominguez, M. Giannotti and A. Mirizzi, *Axion-electron coupling from the rgb tip of globular clusters*, 2018. 32

[63] F. Capozzi and G. Raffelt, *Axion and neutrino bounds improved with new calibrations of the tip of the red-giant branch using geometric distance determinations*, Physical Review D **102** (Oct., 2020) . 32

[64] O. Straniero, C. Pallanca, E. Dalessandro, I. Domínguez, F. R. Ferraro, M. Giannotti et al., *The rgb tip of galactic globular clusters and the revision of the axion-electron coupling bound*, *Astronomy &; Astrophysics* **644** (Dec., 2020) A166. 32

[65] M. Giannotti, I. G. Irastorza, J. Redondo, A. Ringwald and K. Saikawa, *Stellar recipes for axion hunters*, *Journal of Cosmology and Astroparticle Physics* **2017** (Oct., 2017) 010–010. 33

[66] J. E. Kim, *Weak-interaction singlet and strong* CP *invariance*, *Phys. Rev. Lett.* **43** (Jul, 1979) 103–107. 33

[67] M. Dine, W. Fischler and M. Srednicki, *A simple solution to the strong cp problem with a harmless axion*, *Physics Letters B* **104** (1981) 199–202. 33

[68] P. Sikivie, *Experimental Tests of the Invisible Axion*, *Phys. Rev. Lett.* **51** (1983) 1415–1417. 34

[69] Particle Data Group collaboration, R. L. Workman et al., *Review of Particle Physics*, *PTEP* **2022** (2022) 083C01. 35, 48, 133

[70] G. G. di Cortona, E. Hardy, J. P. Vega and G. Villadoro, *The qcd axion, precisely*, *Journal of High Energy Physics* **2016** (Jan., 2016) . 36

[71] J. Redondo, *Solar axion flux from the axion-electron coupling*, *Journal of Cosmology and Astroparticle Physics* **2013** (2013) 008–008. xii, 37, 38, 39, 51, 128, 129

[72] N. Badnell, C. Ballance, M. Bautista, P. Burke, K. Butler, G. Chen et al., *The iron project - the opacity project*, 2024. 38

[73] L. A. N. Laboratory, *Los alamos light element detailed configuration opacity code*, 2024. 38

[74] C. Blancard, P. Cossé and G. Faussurier, *Solar Mixture Opacity Calculations Using Detailed Configuration and Level Accounting Treatments*, ApJ **745** (Jan., 2012) 10. 38

[75] I. Irastorza, F. Avignone, S. Caspi, J. Carmona, T. Dafni, M. Davenport et al., *Towards a new generation axion helioscope*, *Journal of Cosmology and Astroparticle Physics* **2011** (June, 2011) 013–013. 38

[76] E. Armengaud, Q. Arnaud, C. Augier, A. Benoit, A. Benoit, L. Bergé et al., *Axion searches with the edelweiss-ii experiment*, *Journal of Cosmology and Astroparticle Physics* **2013** (Nov., 2013) 067–067. x, 41, 55, 130

[77] R. Germond, *Techniques and challenges in low-mass dark matter searches using CDMS style detectors*. PhD thesis, Queen's U., Kingston, Queen's U., Kingston, 2023. 44, 86

[78] CMS collaboration, A. M. Sirunyan et al., *Search for dark matter particles produced in association with a Higgs boson in proton-proton collisions at* $\sqrt{s} = 13$ *TeV*, *JHEP* **03** (2020) 025, [`1908.01713`]. 45

[79] ATLAS collaboration, G. Aad et al., *Search for dark matter produced in association with a single top quark in* $\sqrt{s} = 13$ *TeV pp collisions with the ATLAS detector*, *Eur. Phys. J. C* **81** (2021) 860, [`2011.09308`]. 45

[80] E. Izaguirre, G. Krnjaic, P. Schuster and N. Toro, *New electron beam-dump experiments to search for mev to few-gev dark matter*, *Physical Review D* **88** (Dec., 2013) . 46

[81] H. Abdalla, F. Aharonian, F. A. Benkhali, E. Angüner, C. Armand, H. Ashkar et al., *Search for dark matter annihilation signals in the h.e.s.s. inner galaxy survey*, *Physical Review Letters* **129** (Sept., 2022) . 47

[82] A. Acharyya, A. Archer, P. Bangale, J. T. Bartkoske, P. Batista, M. Baumgart et al., *Search for ultraheavy dark matter from observations of dwarf spheroidal galaxies with veritas*, *The Astrophysical Journal* **945** (Mar., 2023) 101. 47

[83] V. Acciari, S. Ansoldi, L. Antonelli, A. Arbet Engels, M. Artero, K. Asano et al., *Combined searches for dark matter in dwarf spheroidal galaxies observed with the magic telescopes, including new data from coma berenices and draco*, *Physics of the Dark Universe* **35** (Mar., 2022) 100912. 47

[84] E. Charles, M. Sánchez-Conde, B. Anderson, R. Caputo, A. Cuoco, M. Di Mauro et al., *Sensitivity projections for dark matter searches with the fermi large area telescope*, *Physics Reports* **636** (June, 2016) 1–46. 47

[85] T. Yapici and A. J. Smith, *Dark matter searches with hawc*, 2017. 47

[86] A. Albert, M. André, M. Anghinolfi, G. Anton, M. Ardid, J.-J. Aubert et al., *Search for dark matter towards the galactic centre with 11 years of antares data*, *Physics Letters B* **805** (June, 2020) 135439. 47

[87] M. Chianese, D. F. Fiorillo, G. Miele, S. Morisi and O. Pisanti, *Decaying dark matter at icecube and its signature on high energy gamma experiments*, *Journal of Cosmology and Astroparticle Physics* **2019** (Nov., 2019) 046–046. 47

[88] SUPER-KAMIOKANDE collaboration, K. Abe et al., *Indirect search for dark matter from the Galactic Center and halo with the Super-Kamiokande detector*, *Phys. Rev. D* **102** (2020) 072002, [2005.05109]. 47

[89] M. de Naurois and D. Mazin, *Ground-based detectors in very-high-energy gamma-ray astronomy*, *Comptes Rendus. Physique* **16** (Aug., 2015) 610–627. 47

[90] M. C. Smith, G. R. Ruchti, A. Helmi, R. F. G. Wyse, J. P. Fulbright, K. C. Freeman et al., *The rave survey: constraining the local galactic escape speed*, *Monthly Notices of the Royal Astronomical Society* **379** (Aug., 2007) 755–772. 49

[91] J. Billard, M. Boulay, S. Cebrián, L. Covi, G. Fiorillo, A. Green et al., *Direct detection of dark matter—appec committee report**, *Reports on Progress in Physics* **85** (Apr., 2022) 056201. 51

[92] M. Schumann, *Direct detection of wimp dark matter: concepts and status*, *Journal of Physics G: Nuclear and Particle Physics* **46** (Aug., 2019) 103003. 51

[93] E. Armengaud, D. Attié, S. Basso, P. Brun, N. Bykovskiy, J. Carmona et al., *Physics potential of the international axion observatory (iaxo)*, *Journal of Cosmology and Astroparticle Physics* **2019** (June, 2019) 047–047. 51

[94] M. Bauer, M. Neubert, S. Renner, M. Schnubel and A. Thamm, *The low-energy effective theory of axions and alps*, *Journal of High Energy Physics* **2021** (Apr., 2021) . 51

[95] J. Redondo and A. Ringwald, *Light shining through walls*, *Contemporary Physics* **52** (May, 2011) 211–236. 51, 52

[96] J. Cooley, *Dark matter direct detection of classical wimps*, SciPost Phys. Lect. Notes (2022) 55. 52

[97] T. Nitta, T. Braine, N. Du, M. Guzzetti, C. Hanretty, G. Leum et al., *Search for a dark-matter-induced cosmic axion background with admx*, Physical Review Letters **131** (Sept., 2023) . 52

[98] ADMX collaboration, C. Bartram et al., *Search for Invisible Axion Dark Matter in the 3.3–4.2 μeV Mass Range*, Phys. Rev. Lett. **127** (2021) 261803, [`2110.06096`]. 52

[99] CAST collaboration, V. Anastassopoulos et al., *New CAST Limit on the Axion-Photon Interaction*, Nature Phys. **13** (2017) 584–590, [`1705.02290`]. 53

[100] D. d'Enterria, *Collider constraints on axion-like particles*, 2021. 53

[101] V. Brdar, B. Dutta, W. Jang, D. Kim, I. M. Shoemaker, Z. Tabrizi et al., *Axionlike particles at future neutrino experiments: Closing the cosmological triangle*, Physical Review Letters **126** (May, 2021) . 53

[102] K. Arisaka, P. Beltrame, C. Ghag, J. Kaidi, K. Lung, A. Lyashenko et al., *Expected sensitivity to galactic/solar axions and bosonic super-wimps based on the axio-electric effect in liquid xenon dark matter detectors*, Astroparticle Physics **44** (Apr., 2013) 59–67. 54

[103] E. Aprile, F. Agostini, M. Alfonsi, K. Arisaka, F. Arneodo, M. Auger et al., *First axion results from the xenon100 experiment*, Physical Review D **90** (Sept., 2014) . 54

[104] C. Fu, X. Zhou, X. Chen, Y. Chen, X. Cui, D. Fang et al., *Limits on axion couplings from the first 80 days of data of the pandax-ii experiment*, Physical Review Letters **119** (Nov., 2017) . 54

[105] D. Akerib, S. Alsum, C. Aquino, H. Araújo, X. Bai, A. Bailey et al., *First searches for axions and axionlike particles with the lux experiment*, Physical Review Letters **118** (June, 2017) . 54

[106] E. Aprile, J. Aalbers, F. Agostini, M. Alfonsi, L. Althueser, F. Amaro et al., *Light dark matter search with ionization signals in xenon1t*, Physical Review Letters **123** (Dec., 2019) . 54

[107] Y. Wang, Q. Yue, S. Liu, K. Kang, Y. Li, H. An et al., *Improved limits on solar axions and bosonic dark matter from the cdex-1b experiment using the profile likelihood ratio method*, Physical Review D **101** (Mar., 2020) . 54

[108] R. Bernabei, P. Belli, R. Cerulli, F. Montecchia, F. Nozzoli, A. Incicchitti et al., *Search for solar axions by primakoff effect in nai crystals*, Physics Letters B **515** (2001) 6–12. 55

[109] Z. Ahmed, D. S. Akerib, S. Arrenberg, C. N. Bailey, D. Balakishiyeva, L. Baudis et al., *Search for axions with the cdms experiment*, Physical Review Letters **103** (Oct., 2009) . 55, 64

[110] M. J. Wilson, *A New Search for Low-mass Dark Matter and an Examination and Reduction of the Uncertainty due to the Photoelectric Absorption Cross Section using a Cryogenic Silicon Detector with Single-charge Sensitivity*. PhD thesis, Toronto U., Toronto U., 2022. xii, xiii, 58, 61, 63, 114, 116, 117, 129, 130, 132

[111] R. Pehl, F. Goulding, D. Landis and M. Lenzlinger, *Accurate determination of the ionization energy in semiconductor detectors*, *Nuclear Instruments and Methods* **59** (1968) 45–55. 59

[112] R. Ren, C. Bathurst, Y. Y. Chang, R. Chen, C. W. Fink, Z. Hong et al., *Design and characterization of a phonon-mediated cryogenic particle detector with an ev-scale threshold and 100 kev-scale dynamic range*, *Phys. Rev. D* **104** (Aug, 2021) 032010. 60

[113] G. Wang, *Phonon emission in germanium and silicon by electrons and holes in applied electric field at low temperature*, *Journal of Applied Physics* **107** (06, 2010) 094504 – 094504. 60

[114] W. Shockley, *Currents to Conductors Induced by a Moving Point Charge*, *Journal of Applied Physics* **9** (10, 1938) 635–636. 61

[115] S. Ramo, *Currents induced by electron motion*, *Proceedings of the IRE* **27** (1939) 584–585. 61

[116] D. Akerib, P. Barnes, Jr, P. Brink, B. Cabrera, R. Clarke, R. Gaitskell et al., *Design and performance of a modular low-radioactivity readout system for cryogenic detectors in the cdms experiment*, *Nuclear Instruments and Methods in Physics Research A* **5916020** (07, 2008) . 62

[117] *Dark matter search results from the cdms ii experiment*, *Science* **327** (Mar., 2010) 1619–1621. 64, 66

[118] R. Agnese, T. Aramaki, I. Arnquist, W. Baker, D. Balakishiyeva, S. Banik et al., *Results from the super cryogenic dark matter search experiment at soudan*, *Physical Review Letters* **120** (Feb., 2018) . 64, 65, 70, 104, 105, 106, 107, 111

[119] M. Albakry, I. Alkhatib, D. Amaral, T. Aralis, T. Aramaki, I. Arnquist et al., *Ionization yield measurement in a germanium cdmslite detector using photo-neutron sources*, *Physical Review D* **105** (June, 2022) . 65

[120] SuperCDMS collaboration, R. Agnese et al., *Demonstration of Surface Electron Rejection with Interleaved Germanium Detectors for Dark Matter Searches*, *Appl. Phys. Lett.* **103** (2013) 164105, [`1305.2405`]. 66, 67, 68

[121] S. Zatschler, *Status and prospects of the supercdms dark matter experiment at snolab*, p. 076, 01, 2024. DOI. 67, 72

[122] D. S. Akerib, M. S. Armel-Funkhouser, M. J. Attisha, C. N. Bailey, L. Baudis, D. A. Bauer et al., *Exclusion limits on the wimp-nucleon cross section from the first run of the cryogenic dark matter search in the soudan underground laboratory*, *Physical Review D* **72** (Sept., 2005) . 69

[123] D. Speller and (for the SuperCDMS Collaboration), *Dark matter direct detection with supercdms soudan*, *Journal of Physics: Conference Series* **606** (apr, 2015) 012003. 70

[124] F. Duncan, A. J. Noble and D. Sinclair, *The construction and anticipated science of SNOLAB*, *Ann. Rev. Nucl. Part. Sci.* **60** (2010) 163–180. 70

[125] JNE collaboration, Z. Guo et al., *Muon flux measurement at China Jinping Underground Laboratory*, *Chin. Phys. C* **45** (2021) 025001, [`2007.15925`]. 73

[126] M. Hollister, D. Bauer, R. Dhuley, P. Lukens, L. Martin, M. Ruschman et al., *The cryogenics design of the supercdms snolab experiment*, *IOP Conference Series: Materials Science and Engineering* **278** (12, 2017) 012118. 74

[127] P. Camus, J. Corbett, S. Crawford, K. Dering, E. Fascione, G. Gerbier et al., *Cute: A cryogenic underground test facility at snolab*, *Frontiers in Physics* **11** (Jan., 2024) . 75, 77

[128] U. Schötzig, K. Debertin and K. Walz, *Standardization and decay data of 133ba*, *The International Journal of Applied Radiation and Isotopes* **28** (1977) 503–507. 87

[129] J. MacQueen, *Some methods for classification and analysis of multivariate observations*, in *Proceedings of the fifth Berkeley symposium on mathematical statistics and probability*, vol. 1, pp. 281–297, 1967. 89

[130] P. J. Rousseeuw, *Silhouettes: A graphical aid to the interpretation and validation of cluster analysis*, *Journal of Computational and Applied Mathematics* **20** (1987) 53–65. 89

[131] R. Agnese, T. Aralis, T. Aramaki, I. Arnquist, E. Azadbakht, W. Baker et al., *Search for low-mass dark matter with cdmslite using a profile likelihood fit*, *Physical Review D* **99** (Mar., 2019) . xiii, 92, 93, 94, 96, 97, 98, 103, 104, 105, 106, 108, 109, 110, 111, 112

[132] D. Michael, P. Adamson, T. Alexopoulos, W. Allison, G. Alner, K. Anderson et al., *The magnetized steel and scintillator calorimeters of the minos experiment*, *Nuclear Instruments and Methods in Physics Research Section A: Accelerators, Spectrometers, Detectors and Associated Equipment* **596** (Nov., 2008) 190–228. 93

[133] R. Agnese, A. Anderson, T. Aramaki, M. Asai, W. Baker, D. Balakishiyeva et al., *New results from the search for low-mass weakly interacting massive particles with the cdms low ionization threshold experiment*, *Physical Review Letters* **116** (Feb., 2016) . 94

[134] D. Bauer, S. Burke, J. Cooley, M. Crisler, P. Cushman, F. DeJongh et al., *The cdms ii data acquisition system*, *Nuclear Instruments and Methods in Physics Research Section A: Accelerators, Spectrometers, Detectors and Associated Equipment* **638** (2011) 127–133. 95

[135] SuperCDMS Collaboration collaboration, R. Agnese, A. J. Anderson, T. Aralis, T. Aramaki, I. J. Arnquist, W. Baker et al., *Low-mass dark matter search with cdmslite*, *Phys. Rev. D* **97** (Jan, 2018) 022002. 96

[136] J. Brown, M. Dimmock, J. Gillam and D. Paganin, *A low energy bound atomic electron compton scattering model for geant4*, *Nuclear Instruments and Methods in Physics Research Section B: Beam Interactions with Materials and Atoms* **338** (2014) 77–88. 108

[137] S. Agostinelli, J. Allison, K. Amako, J. Apostolakis, H. Araujo, P. Arce et al., *Geant4—a simulation toolkit*, *Nuclear Instruments and Methods in Physics Research Section A: Accelerators, Spectrometers, Detectors and Associated Equipment* **506** (2003) 250–303. 109, 111

[138] J. Yeh and I. Lindau, *Atomic subshell photoionization cross sections and asymmetry parameters: 1 $\leq z \leq$ 103*, *Atomic Data and Nuclear Data Tables* **32** (1985) 1–155. 113

[139] J. H. Scofield, *Theoretical photoionization cross sections from 1 to 1500 kev*, . 113

[140] M. J. Berger et al., "XCOM: Photon Cross Section Database (version 1.5)." http://physics.nist.gov/xcom, 2010. xii, 114, 116, 129, 130, 132

[141] G. Macfarlane, T. McLean, J. Quarrington and V. Roberts, *Fine structure in the absorption-edge spectrum of si*, *Physical Review* **111** (Sep, 1958) 1245–1254. 116

[142] R. Hulthén, *Optical constants of epitaxial silicon in the region 1 – 3.3 ev*, *Physica Scripta* **12** (1975) . 116

[143] D. F. Edwards, *Silicon (si)*, in *Handbook of Optical Constants of Solids*, p. 547–569. Academic Press, Burlington, 1997. 116

[144] S. E. Holland, D. E. Groom, N. P. Palaio, R. J. Stover and M. Wei, *Fully depleted, back-illuminated charge-coupled devices fabricated on high-resistivity silicon*, *IEEE Transactions on Electron Devices* **50** (2003) 225–238. 116

[145] M. A. Green, *Self-consistent optical parameters of intrinsic silicon at 300k including temperature coefficients*, *Solar Energy Materials and Solar Cells* **92** (2008) 1305–1310. 116

[146] M. A. Green and M. J. Keevers, *Optical properties of intrinsic silicon at 300 k*, *Progress in Photovoltaics: Research and Applications* **3** (1995) 189–192. 116

[147] E. M. Gullikson, P. Denham, S. Mrowka and J. H. Underwood, *Absolute photoabsorption measurements of mg, al, and si in the soft-x-ray region below the l2,3 edges*, *Physical Review B* **49** (Jun, 1994) 16283–16288. 116

[148] C. Gähwiller and F. C. Brown, *Photoabsorption near the lii,iii edge of silicon and aluminum*, *Physical Review B* **2** (1970) 1918–1925. 116

[149] C. Gähwiller and F. Brown, *Photoabsorption near the lii,iii edge of silicon*, in *Proc. 10th International Conference on the Physics of Semiconductors*, pp. 213–216, U.S. Atomic Energy Commission, Division of Technical Information, 1970. 116

[150] F. C. Brown, R. Z. Bachrach and M. Skibowski, $l_{2,3}$ *threshold spectra of doped silicon and silicon compounds*, *Physical Review B* **15** (May, 1977) 4781–4788. 116

[151] F. C. Brown and O. P. Rustgi, *Extreme ultraviolet transmission of crystalline and amorphous silicon*, *Physical Review Letters* **28** (Feb, 1972) 497–500. 116

[152] L. Da-Chun, L. Ping-An and Y. Hua, *Measurement of the mass attenuation coefficients for sih4 and si*, *Nuclear Instruments and Methods in Physics Research Section B: Beam Interactions with Materials and Atoms* **95** (1995) 161–165. 116

[153] D. E. Aspnes and A. A. Studna, *Dielectric functions and optical parameters of si, ge, gap, gaas, gasb, inp, inas, and insb from 1.5 to 6.0 ev*, *Physical Review B* **27** (Jan, 1983) 985–1009. 116

[154] W. C. Dash and R. Newman, *Intrinsic optical absorption in single-crystal germanium and silicon at 77°k and 300°k*, *Physical Review* **99** (1955) 1151. 116

[155] C. Chantler, K. Olsen, R. A. Dragoset, J. Chang, A. R. Kishore, S. Kotochigova et al., *X-Ray Form Factor, Attenuation and Scattering Tables (version 2.1)*. No. 66. NIST Standard Reference Database, 2005. 116

[156] G. D. Doolen and D. A. Liberman, *Calculations of photoabsorption by atoms using a linear response method*, *Physica Scripta* **36** (1987) 77–79. 116

[157] B. L. Henke, E. M. Gullikson and J. C. Davis, *X-ray interactions: Photoabsorption, scattering, transmission, and reflection at e = 50-30,000 ev, z = 1-92*, *Atomic Data and Nuclear Data Tables* **54** (1993) 181 – 342. 116

[158] W. R. Hunter, *Observation of absorption edges in the extreme ultraviolet by transmittance measurements through thin unbacked metal films*, in *Optical Properties and Electron Structure of Metals and Alloys* (F. Abelès, ed.), p. 136–146. North-Holland Publishing Company, 1966. 116

[159] G. Hildebrandt, J. D. Stephenson and H. Wagenfeld, *Normale und anomale absorption von röntgen-strahlen in germanium und silicium*, *Zeitschrift für Naturforschung A* **28** (1973) 588. 116

[160] G. G. Macfarlane, T. P. McLean, J. E. Quarrington and V. Roberts, *Fine structure in the absorption-edge spectrum of ge*, *Physical Review* **108** (Dec, 1957) 1377–1383. 116

[161] H. R. Philipp and E. A. Taft, *Optical constants of germanium in the region 1 to 10 ev*, *Physical Review* **113** (Feb, 1959) 1002–1005. 116

[162] L. Marton and J. Toots, *Optical properties of germanium in the far ultraviolet*, *Physical Review* **160** (Aug, 1967) 602–606. 116

[163] M. Cardona, W. Gudat, B. Sonntag and P. Yu, *Optical absorption of semiconductors from 12 ev to 200 ev*, in *Proc. 10th International Conference on the Physics of Semiconductors*, pp. 209–212, U.S. Atomic Energy Commission, Division of Technical Information, 1970. 116

[164] O. A. Ersov, I. A. Brytov and A. P. Lukirskii, *Reflection of x rays from certain substances in the region 7 to 44 Å*, *Optics and Spectroscopy* **22** (1967) 66–69. 116

[165] S. Yellin, *Extending the optimum interval method*, 2007. 118

[166] J. Lewin and P. Smith, *Review of mathematics, numerical factors, and corrections for dark matter experiments based on elastic nuclear recoil*, *Astroparticle Physics* **6** (1996) 87–112. 118

[167] J. Neyman, E. S. Pearson and K. Pearson, *Ix. on the problem of the most efficient tests of statistical hypotheses*, *Philosophical Transactions of the Royal Society of London. Series A, Containing Papers of a Mathematical or Physical Character* **231** (1933) 289–337. 120

[168] M. Albakry, I. Alkhatib, D. Alonso-González, D. Amaral, T. Aralis, T. Aramaki et al., *Search for low-mass dark matter via bremsstrahlung radiation and the migdal effect in supercdms*, *Physical Review D* **107** (June, 2023) . xiii, 126

[169] F. James and M. Roos, *Minuit: A System for Function Minimization and Analysis of the Parameter Errors and Correlations*, *Comput. Phys. Commun.* **10** (1975) 343–367. 127

[170] iminuit team, “iminuit – a python interface to minuit.” https://github.com/scikit-hep/iminuit. 127